TU Delft

Delft University of Technology

Document Version
Final published version

Licence
CC BY-NC-SA

Citation (APA)
Li, Y. (2025). *Beyond the Surface: Non-Invasively Revealing Hidden Composition in Bronze Heritage Artefacts through Neutron Tomography and Gamma Spectroscopy*. [Dissertation (TU Delft), Delft University of Technology]. https://doi.org/10.4233/uuid:cf2c1444-9642-42c6-963c-c70a76d9cd70

Important note
To cite this publication, please use the final published version (if applicable).
Please check the document version above.

Copyright
In case the licence states “Dutch Copyright Act (Article 25fa)”, this publication was made available Green Open Access via the TU Delft Institutional Repository pursuant to Dutch Copyright Act (Article 25fa, the Taverne amendment). This provision does not affect copyright ownership.
Unless copyright is transferred by contract or statute, it remains with the copyright holder.

Sharing and reuse
Other than for strictly personal use, it is not permitted to download, forward or distribute the text or part of it, without the consent of the author(s) and/or copyright holder(s), unless the work is under an open content license such as Creative Commons.

Takedown policy
Please contact us and provide details if you believe this document breaches copyrights.
We will remove access to the work immediately and investigate your claim.

This work is downloaded from Delft University of Technology.

BEYOND THE SURFACE

Non-Invasively Revealing Hidden Composition in Bronze Heritage Artefacts through Neutron Tomography and Gamma Spectroscopy



Yueer Li 李玥儿

Beyond the Surface

Non-Invasively Revealing Hidden Composition in Bronze Heritage Artefacts through Neutron Tomography and Gamma Spectroscopy

Beyond the Surface

Non-Invasively Revealing Hidden Composition in Bronze Heritage Artefacts through Neutron Tomography and Gamma Spectroscopy

Dissertation

for the purpose of obtaining the degree of doctor
at Technische Universiteit Delft,
by the authority of the Rector Magnificus, prof. dr. ir. T.H.J.J. van der Hagen,
chair of the Board of Doctorates,
to be defended publicly
on Wednesday 17 December 2025 at 10:00

by

Yueer LI

Master of Science in Biomedical Engineering,
Beijing Institute of Technology, China,
born in Dazu, Chongqing, China.

This dissertation has been approved by the

promotor: Prof. dr. C. Pappas
copromotor: Dr. L. van Eijck

Composition of the doctoral committee:

Rector Magnificus,	Chairperson
Prof. dr. C. Pappas,	Technische Universiteit Delft
Dr. L. van Eijck,	Technische Universiteit Delft
Onafhankelijke leden:	
Prof. dr. J. Dik,	Technische Universiteit Delft, the Netherlands
Dr.ir. M.C. Goorden,	Technische Universiteit Delft, the Netherlands
Dr. I. Joosten,	Cultural Heritage Agency (RCE), the Netherlands
Prof. dr. K. Keune,	UvA / Rijksmuseum, the Netherlands
Prof. dr. M. Strobl,	Paul Scherrer Institute (PSI), Switzerland
Prof.dr. E.H. Brück,	Technische Universiteit Delft, reserve member

This research work is part of the NICAS-Beeldvorming project funded by NWO (grant no. 628-007-032), carried out in close collaboration with the Rijksmuseum in Amsterdam and Cultural Heritage Agency of the Netherlands.







Keywords: data fusion; conservation; simulation; GPUs; Geant4; Vulkan; bronze; heritage science; imaging; neutron activation; self-attenuation correction; simulation acceleration, gamma radiation, neutron

ISBN: 978-94-6384-886-2
Printed by ProefschriftMaken, the Netherlands
Cover page designed by Yueer Li
Copyright © 2025 by Yueer Li

to my parents

Contents

Preface **xi**

1 Introduction **1**
1.1 Modern vs. Ancient Craftsmanship: New Insights into the Ommerschans Sword from Neutron Tomography . . . 2
1.2 Neutron Tomography: Advantages and One Disadvantage . . . 4
1.3 Gamma Spectroscopy: Turning the Disadvantage into an Advantage . . . 6
1.4 Data Fusion: Rendering a 3D Model with Quantitative Elemental Information . . . 7
1.5 Thesis Objectives and Structure . . . 7

2 Theoretical foundations and experimental details **9**
2.1 Introduction . . . 10
2.2 Neutron Tomography . . . 10
2.2.1 Scattering and Capture of Thermal Neutrons by Bronzes . . . 10
2.2.2 Neutron Beam . . . 12
2.3 Gamma Spectroscopy . . . 13
2.3.1 Gamma Production . . . 13
2.3.2 Interactions Between Gamma Emissions and Matter . . . 14
2.3.3 Key Experimental Parameters . . . 15

3 Validation of 1D Self-attenuation Corrections in Mass Quantification **17**
3.1 Introduction . . . 18
3.2 Mass Quantification from Gamma Spectroscopy . . . 19
3.2.1 Theoretical Calculation . . . 19
3.2.2 Measurement Strategy in Practical Bronze Research . . . 20
3.2.3 1D Self-Attenuation Corrections Using a Matchbox Model . . . 21
3.3 Method Validation . . . 23
3.3.1 Experiment and Materials . . . 23
3.3.2 Results and Discussion . . . 24
3.4 Applications . . . 25
3.4.1 Dagger Fragment . . . 25
3.4.2 Shiva's Pendant . . . 27
3.4.3 Kuvera Statuette . . . 29
3.5 Conclusion . . . 29

4 Geant4-based Iterative Simulation Method for Element-to-Source Material Assignment and Compositional Quantification **31**
4.1 Introduction . . . 32

4.2 Methods . . . 34
4.2.1 Object Geometry from Neutron Tomography. . . . 34
4.2.2 The First Composition from Gamma Spectroscopy . . . 35
4.2.3 Simulation of Experiments Using Monte Carlo Method. . . . 35
4.2.4 Comparing Simulations with Experiments . . . 35
4.3 Materials and experiments . . . 36
4.3.1 CYL . . . 37
4.3.2 CUBE . . . 37
4.3.3 Kuvera Statuette . . . 37
4.4 Results and discussion . . . 38
4.4.1 Method validation . . . 38
4.4.2 Analysis of the Kuvera Statuette . . . 41
4.5 Conclusion . . . 42

5 New GPU-based Simulation Framework to Accelerate Data Fusion 45
5.1 Introduction . . . 46
5.2 Implementing NT-GS Simulations via Vulkan Ray Tracing . . . 48
5.2.1 Ray-tracing Pipeline and Shader-Based GPU Execution . . . 48
5.2.2 Integrating Stochastic Physical Processes into Ray-Tracing Shaders 50
5.2.3 GPU Output and Data Processing . . . 55
5.3 Simulation Validation . . . 56
5.3.1 Neutron Beam . . . 56
5.3.2 Neutron Radiography . . . 56
5.3.3 Gamma Spectroscopy . . . 58
5.4 Application to the Ommerschans Sword . . . 59
5.5 Comparison of the Three Mass Quantification Methods Applied to the Ommerschans Sword. . . . 61
5.6 Conclusion . . . 62

6 Conclusion and Outlook 65
6.1 Summary of Contributions . . . 65
6.2 General Discussion and Comparative Analysis . . . 66
6.3 Outlook and Future Work . . . 67

A Supplementary Information 69

Bibliography 81

Acknowledgments 89

Curriculum Vitæ 91

List of Publications 93

Preface

Understanding the internal features of cultural heritage artefacts—without damaging them—remains one of the most important and challenging goals in conservation science. These artefacts often carry centuries of history, yet their true stories are hidden beneath layers of corrosion or folded within inaccessible interiors. Traditional non-invasive techniques tend to focus on surface features, while bulk information remains elusive—particularly for dense materials like bronze.

Neutron tomography (NT) offers a way forward, looking deeply. It is capable of probing internal structures with high metal penetration and sensitivity to light elements. However, during NT scans, the artefact is inevitably rendered radioactive temporarily, emitting gamma rays. This radioactivity is typically seen as a drawback and is often treated as waste. But what if it could be turned into an asset?

This thesis begins with that question. Rather than treating the gamma radiation as an unfortunate by-product, it proposes an insightful strategy: to perform gamma spectroscopy (GS) after NT, using the induced radioactivity to gain elemental composition "for free". At first glance, NT and GS seem to measure different things—geometry and composition—but when performed on the same object, they carry inherently consistent information. Together, they offer two sides of the same physical reality. Fusing these data holds the potential for spatially resolved, quantitative elemental analysis deep within heritage artefacts.

The idea is elegant in principle, but challenging in practice. Neutrons and gamma rays are both heavily attenuated in dense materials, and interpreting the resulting signals requires careful correction for these effects. Highly accurate solutions rely on Monte Carlo simulations that, while accurate, are too slow and resource-intensive. Achieving both high data fusion accuracy and computational efficiency became the central challenge of this work.

This thesis is, to the best of the author's knowledge, the first systematic study dedicated to developing and comparing multiple data-fusion methods that combine NT and GS for quantitative, non-destructive elemental analysis. Instead of proposing a one-size-fits-all solution, it develops a suite of three complementary approaches, each designed to balance accessibility, analytical accuracy, and computational performance. These range from a fast, analytical model for rapid estimation, to a simulation-driven method capable of handling complex geometries, and finally, to a GPU-accelerated framework that dramatically reduces analysis time from weeks to hours without compromising physical fidelity and analytical accuracy.

Collectively, they form a practical and adaptable "toolkit" for cultural heritage research—methods that can be chosen according to the object, the research question, and the available resources. This work hopes to broaden the application of neutron-based techniques in conservation science, not only by pushing technical boundaries, but also by making these methods more accessible and more aligned with real-world needs.

While this work is performed with a focus on ancient bronzes and archaeological artefacts, the methods are general. They may find application wherever rapid, non-invasive compositional insight is needed—from archaeology and museum studies to plant research and material science. It is the author's hope that this work opens new possibilities for both heritage science and neutron techniques, encouraging researchers to see not just what lies beneath the surface—but how we might understand it more fully and more respectfully, beyond the surface, than ever before.

Yueer Li
Delft, September 2025

1

Introduction

1

1.1 Modern vs. Ancient Craftsmanship: New Insights into the Ommerschans Sword from Neutron Tomography

At first glance, it is tempting to assume that modern craftsmanship must be better than that of the ancient world: today's artists benefit from a deeper understanding of materials and access to vastly more advanced manufacturing tools. Bronze casting, however, provides an interesting counter-example to this intuition.

When ancient people discovered that adding an appropriate amount of tin to molten copper can make copper stronger, harder, and easier to cast, they sparked the Bronze Age (2000-800 BC). Since then, bronze (copper alloyed with tin and other trace elements) has been widely used for casting objects of diverse sizes and functions [1–5]. Thanks to the chemical stability of bronze, many such objects have been well preserved and have become cultural legacies of ancient civilizations, with significance beyond their original functions.

The Ommerschans sword [6] (Figure 1.1), a masterpiece of solid-casting bronze, is one of the icons of Dutch archaeology. It dates back over 3000 years, being considered particularly important as it demonstrates that the Netherlands experienced a true Bronze Age. It is notable that this is a giant artefact, approximately 70 cm long and weighing 3 kg. Those features, along with its abstract decorative patterns, strongly suggest it was an object for a special or ceremonial purpose rather than a weapon or an object for daily use. Archaeologists hypothesize that this sword was deliberately deposited in a bog as a ritual offering, transiting one world to another, in exchange with a supernatural world of ancestors and gods [7]. A key question thus arises: how was such a large, solid bronze object cast thousands of years ago, potentially in the prehistoric Netherlands?

To investigate this, a skilled contemporary bronzesmith was commissioned in 2019 to cast a replica (Figure 1.2). Subsequently, in 2022, both the ancient sword and its modern replica underwent neutron tomography (NT) experiments (Figure 1.3) on the FISH imaging beamline of the TU Delft | Reactor Institute [8]. This



Figure 1.1: The Ommerschans sword (RMO *inv.* no. d 2017/7.1), discovered in 1896 near Ommerschans in the northern Netherlands and now held by the *Rijksmuseum van Oudheden*. Among the six almost identical swords that have been found across England, France and the Netherlands, the Ommerschans sword is the most impressive, intact one and is thought to have played a powerful ceremonial role during the Bronze Age.

NT technique enabled non-invasive "internal examination" of the two bulk bronze swords and direct comparison of their interior structures (Figure 1.4). The results are striking: The prehistoric sword exhibits remarkable homogeneity in both structure and composition aspects. It is almost perfect with a near-complete absence of internal porosity, compared to the significant internal defects displayed in the tip region of the modern replica. These defects are caused by trapped air during casting, characterized by numerous "black holes" in the NT slices. This significant difference underscores the sword's extraordinary casting quality and highlights the persistent difficulty in casting such large, high quality bronze objects in modern times, not to mention in prehistoric times.

This prehistoric sword directly challenges the common assumption of inherent modern craftsmanship superiority. Furthermore, its study demonstrates the powerful capability of NT to non-destructively reveal previously inaccessible internal structures of artefacts. While NT has gained significant popularity in ancient bronze research for gaining insights on interior structures, this thesis argues that its utility extends beyond mere structure probing. I propose that NT, when combined with careful consideration of characteristic activation radiation from it, can also be employed to quantify the interior elemental composition of bulk bronzes to a certain extent. This thesis details the methodology for achieving such composition quantification through NT and subsequent gamma spectroscopy (GS). The aim of this research is to derive quantitative structural and elemental information of the bulk bronze objects by fusing experimental NT and GS datasets.



Figure 1.2: The ancient Ommerschans sword and its modern replica (RMO *inv.* no. z 2019/11.1) made by *Jeroen Zuiderwijk* in 2019 [7].

1.2 Neutron Tomography: Advantages and One Disadvantage

Compared to X-rays, neutrons offer distinct advantages in their ability to penetrate thick and dense materials while also providing sensitivity to both light and heavy elements. This makes NT well-suited to non-invasively studying the interior structure of bronzes, even when they are obscured by thick corrosion layers [9–12]. The resulting 3D dataset consists of voxels, whose grey values reflect the atomic density as well as the neutron interaction cross sections of local compositions [13]. This enables the segmentation of different compositional components within the artefact.

By comparing the brightness of the segmented components with that of the main bronze, possibly along with a known background of the object, initial hypotheses about what the segmented materials could be can reasonably be formulated. For instance, a region significantly brighter than the surrounding bronze and shaped like a jewel is likely to contain precious metals such as silver or gold. Conversely, a darker region at a mechanical joint may represent a soldering material rich in tin or lead (according to the neutron attenuation coefficients (cm^{-1}) of Au (6.23) > Ag (4.04) > Cu (1.07) > Pb (0.38) > Sn (0.21)). Such composition information is valuable because it sheds light on ancient manufacturing techniques and cultural practices.

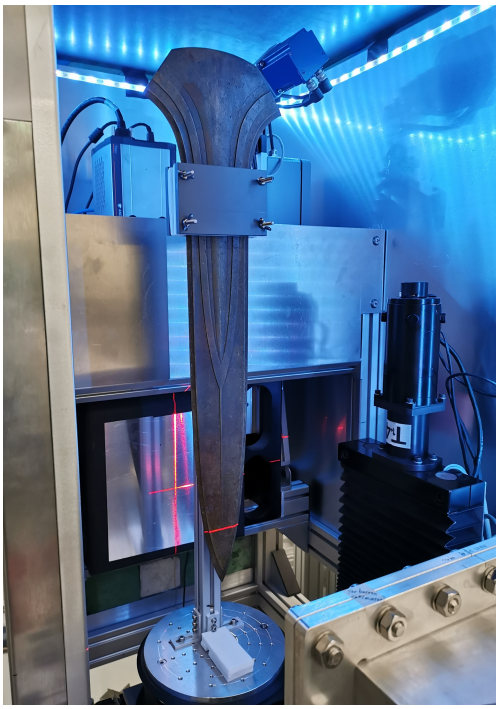

Figure 1.3: The Ommerschans sword during the NT experiment. The photo was taken from a perspective facing upstream of the imaging beamline. The sword was fixed on a rotating platform by an aluminium holder and a clamp of two plastic plates and foam in between. Neutrons, coming from a neutron guide, arrived at the position where the sword was. Part of them transmitted through the sword and hit a scintillator, where photons were generated and then detected by a camera behind, forming a neutron projection image. During the experiment, the sword was rotated for a full circle, and projections from different angles were taken accordingly, which were then used to reconstruct the 3D NT model of the sword.

However, confirming these hypotheses non-destructively remains a key challenge in heritage science. X-ray Fluorescence (XRF), though widely used, probes only the outer micrometres of metal objects and has limited ability to quantify compositions. By contrast, the isotope-specific delayed gamma emissions induced during NT experiments are energetic enough to escape from deep within the object, providing a more promising way for non-destructive, quantitative compositional analysis of bulk materials.

In practice, the delayed radioactivity induced by neutron irradiation from NT is always a

concern: an artefact cannot be returned until its activity has fallen below the radiation safety limit, and it must therefore be stored under controlled conditions during this "cooling down" period. Although this temporary activation radiation was often seen as a disadvantage of NT, it also creates a unique opportunity to obtain elemental information of bulk objects "for free". Because the object rotates during the NT experiment, every surface experiences effectively the same neutron irradiation, resulting in a nearly uniform activation across all angles. Furthermore, thanks to the deep penetration of neutrons, the induced gamma rays originate from throughout the object volume, meaning the emitted photons carry information not only from the outer surface but also from the interior (pristine) core, which is typically inaccessible to most other non-destructive techniques. Since activation is already an unavoidable consequence of NT, it is both efficient and scientifically valuable to make good use of it. What was commonly seen as a limitation can instead serve as a powerful source of interior compositional insight through GS performed after NT.

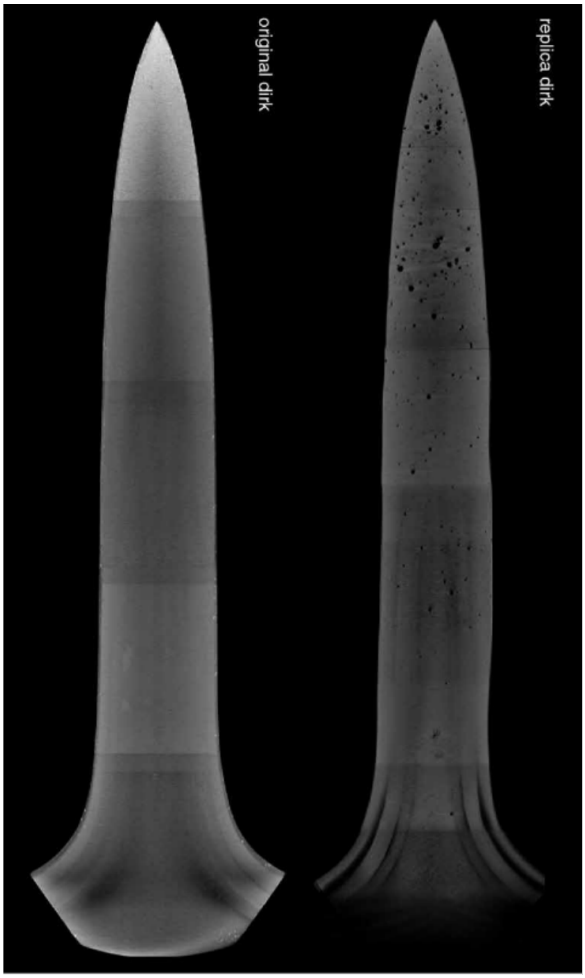

Figure 1.4: Cross-section slices of the reconstructed NT model of the prehistoric Ommerschans sword (left) and its modern replica (right), showing their interior difference that the replica contains considerable porosity (black holes) in the tip region of the dirk, whereas the original Ommerschans is virtually free of porosity. Both images show computer artefact (the "horizontal stripes) caused by the CT reconstruction and data stitching.

1

1.3 Gamma Spectroscopy: Turning the Disadvantage into an Advantage

Exploiting neutron activation to investigate the composition of bulk artefacts is not new in heritage science. Instrumental Neutron Activation Analysis (INAA) [14, 15], Prompt Gamma-ray Activation Analysis (PGAA) [16, 17], and Neutron Resonance Capture Analysis (NRCA) [18, 19] have pursued this goal by applying the same fundamental principle that neutron irradiation induces characteristic gamma emissions that can escape from within bulk artefacts, enabling non-invasive elemental quantification for interior compositions. Among these, PGAA is increasingly considered a routine analytical method at neutron research facilities and is being actively developed further, such as PGAI-NT [20], ibNAA [21], and T-PGAA [22]. Nevertheless, PGAA facilities are not as common as INAA, as PGAA has higher requirements for detector efficiency and shielding for both neutrons and gamma rays. This thesis demonstrates that even without the infrastructure of PGAA on-site, one can still use delayed-emitted gamma rays from the induced radioactivity to obtain quantitative information on the bulk composition in a non-invasive manner.

The strategy used in this work, similar to INAA, measures delayed radioactive decay through GS, but the neutron activation is performed in an NT experiment. By combining GS with NT, it becomes possible to make productive use of the otherwise wasted activation radiation, gaining quantitative compositional insight in addition to the structural information provided by NT, without requiring additional neutron beam time. The only infrastructure needed to measure such gamma radiation is a HPGe detector in a low-gamma-background environment, typically away from the beam line. INAA is well-known for its highly accurate and precise elemental analysis of homogeneous powders in milligram quantities [23]. However, when applied to large artefacts such as bronze statuettes (on the centimetre scale), quantification faces two key challenges [24]. First, self-attenuation effects of both penetrating neutrons and gamma rays become too significant [25], and correcting for this is essential [26]. In the case of ancient bronzes, however, such corrections are particularly tedious due to their irregular shapes and internal inhomogeneities. Second, gamma spectra inherently lack spatial resolution, making it difficult to link detected elements to specific materials within the object. This could be problematic in heritage artefacts, which often incorporate a variety of materials, such as decorative gilding, ritual inclusions, or restoration materials.

To address these challenges, three typical scenarios that often encountered in bronze research are summarised:

- **Situation 1:** Simple artefacts with effectively regular geometry and homogeneous composition. For example, the small dagger fragment shown in Figure 3.5.
- **Situation 2:** Complex artefacts with irregular geometry and/or inhomogeneous composition, such as the Kuvera statuette with a mysterious consecration deposit embedded in its pedestal shown in Figure 4.1.
- **Situation 3:** Artefacts involved in a complex experiment, which could lead to significantly high computational demands when applying the simulation-based method (used in Situation 2). For example, the neutron investigation of the Ommerschans sword (Figure 5.1), which experienced eight neutron scans at different heights for

a complete dataset, represents a particularly time-consuming case for traditional CPU-based simulations and requires a more advanced simulation tool.

Each scenario calls for a tailored data-fusion method, which is detailed in the following section.

1.4 Data Fusion: Rendering a 3D Model with Quantitative Elemental Information

Combining NT with GS enables us to extract interior elemental information in addition to structure information of bulk artefacts. However, data-fusing these two datasets remains challenging. This thesis presents three complementary solutions (detailed in Chapter 3, 4, and 5) corresponding to the three scenarios, all sharing the goal of identifying which elements originate from which parts of the 3D NT model and quantifying the compositions of different regions discernible in the NT data.

- **Method 1: Mass Quantification with 1D Self-attenuation Corrections**
  For a simple object, elemental masses can be directly and effectively calculated from GS spectra by applying a simplified "matchbox" model for self-attenuation corrections.
- **Method 2: Iterative Method using Geant4 Ray-tracing Simulations**
  For a more complex object, Method 1 does not work due to the object's inhomogeneity and shape complexity, while elemental compositions can be indirectly derived by using an iterative method with Geant4-based Monte Carlo simulations [27], regardless of those complexities.
- **Method 3: Iterative Method with an GPU-accelerated Simulation Core**
  For cases involving complex experiments, a new GPU-accelerated ray-tracing simulation framework is developed to replace the traditional Geant4-based simulation toolkit used in Method 2, providing a more efficient simulation tool for data fusion.

1.5 Thesis Objectives and Structure

The overarching objective of this thesis is to develop and validate a new analytical strategy in heritage science that elegantly combines NT and GS for fully non-destructive, quantitative analysis of interior elemental composition in large (bulk) bronze artefacts.

With this strategy, it becomes possible to access deep, pristine materials that were previously inaccessible, all without causing any damage. This is particularly valuable in heritage science, where preservation is critical and interior information, especially from pristine materials, plays an important role in understanding the manufacturing techniques of past cultures. Additionally, this strategy makes full use of the activation radiation from NT, which was often otherwise wasted. As a result, it adds a composition analysis dimension to NT without requiring extra neutron beam time, which is limited and precious.

This work focuses on heritage objects for which the non-invasive analysis is crucial, with a specific emphasis on bronzes. In this thesis, three different methods are introduced for three typical scenarios in bronze research: a single neutron scan on a simple object, a

single neutron scan on a complex object, and a complex experiment with multiple neutron scans on a large object. These methods are validated using reference samples and then applied to different archaeological bronzes. The structure of the thesis is outlined in Figure 1.5 and detailed below:

- **Chapter 2:** Theoretical background and experimental setup.
- **Chapter 3:** Method 1—implementation and validation; applications to ancient bronzes with varying sizes and shapes.
- **Chapter 4:** Method 2—implementation and validation; application to an intricate Indonesian statuette.
- **Chapter 5:** Method 3—implementation and validation of the GPU-based simulation framework; application to the Ommerschans sword; a comparison against Method 1 and 2 on that case.
- **Chapter 6:** General conclusions and outlook.

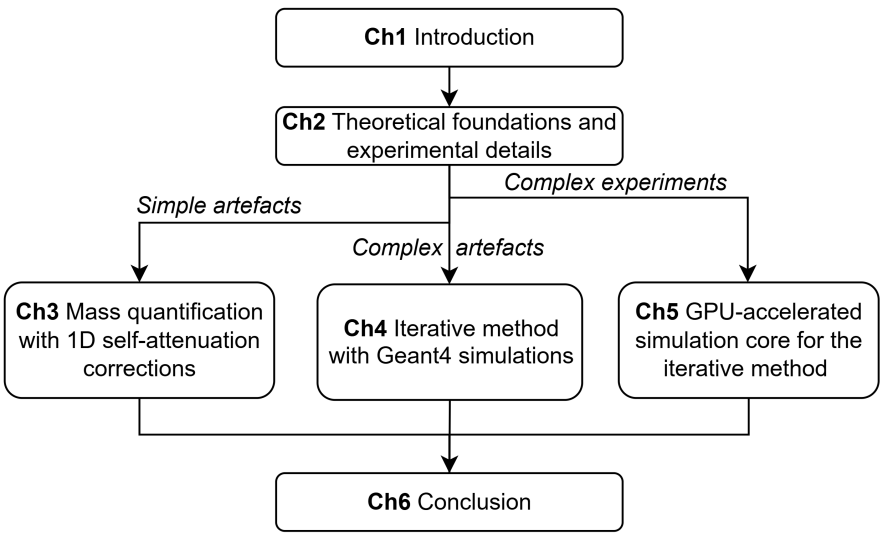

Figure 1.5: The structure of this thesis.

2

Theoretical foundations and experimental details

2.1 Introduction

This chapter introduces the two primary techniques employed in this study, namely neutron tomography (NT) [28] and gamma spectroscopy (GS) [29]. It provides an overview of the physical principles behind these techniques, including primary particle interactions and the production of gamma rays. Key experimental parameters are also discussed, particularly those relevant to the mass calculation directly derived from GS (Method 1) and to the simulations performed for NT and GS experiments (Method 2 and Method 3).

All experiments presented in this thesis were conducted on the FISH imaging beamline of the TU Delft | Reactor Institute [8]; this information will not be repeated in subsequent chapters.

2.2 Neutron Tomography

Similar to X-ray computed tomography (CT) commonly used in hospitals, NT is also an imaging technique; however, it is more commonly applied to non-human-or-animal objects, especially cultural heritage artefacts such as bronzes. Figure 2.1 shows the principle of NT, via which a 3D model of the object's interior structure is reconstructed from 2D neutron projections acquired from various angles in 2π radians, using specialised reconstruction software such as Octopus [30], MuhRec [31], and NeuTomPy [32].

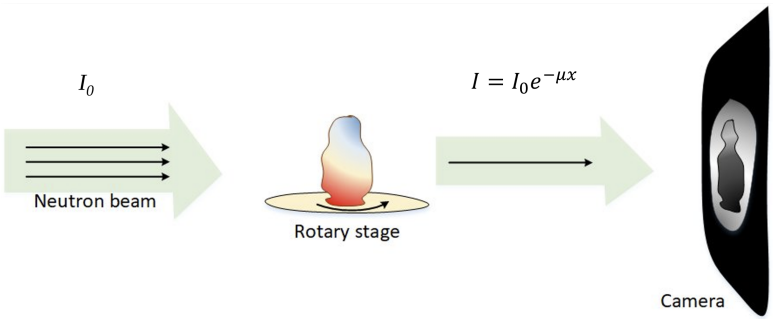

Figure 2.1: Schematic of a typical NT experiment. Neutrons are emitted in parallel from a source with initial intensity I_0. During the experiment, the object rotates while some of the neutrons interact with it and the rest pass through, resulting in a reduced intensity I. The transmission decreases exponentially with both the neutron path length through the object x and the material's neutron attenuation coefficient μ. The downstream "neutron camera" consists of a scintillator, a mirror, and a camera. The scintillator converts the transmitted neutrons into visible light photons, which are then reflected by the mirror and detected by the camera to form projection images.

2.2.1 Scattering and Capture of Thermal Neutrons by Bronzes

Interactions

As shown in Figure 2.1, the interactions between neutrons and the object result in a reduction of the neutron flux reduced. The interactions include neutron scattering and capture.

Table 2.1: Cross sections of neutrons (at 2200 m/s) for Cu and Sn.

Element	Coh. xs [barn]	Inc. xs [barn]	Abs. xs [barn]
Cu	7.485	0.550	3.780
Sn	4.871	0.022	0.626

Note: Coh. xs = Coherent scattering cross section; Inc. xs = Incoherent scattering cross section; Abs. xs = Absorption cross section.

For bronze, most neutrons will be scattered coherently, see Table 2.1. Given the mass difference between a neutron and a copper or tin atom, elastic scattering dominate the process, resulting in a scattering angle satisfying Bragg's law [33] and no change in energy after scattering.

Given that the crystallite orientations in cast bronzes are equally likely, the neutrons are scattered into space forming what are known as Debye-Scherrer cones [34]. Within large 3D artefacts, neutron scattering occurs at diverse penetration depths within the object, from randomly oriented grains. As a result, multiple cones overlap in space, causing an effectively uniform distribution of scattered neutrons.

Neutron capture is a process in which an isotope captures a neutron and forms a heavier isotope:

$$ {}^{A}_{Z}\mathrm{X} + \mathrm{n} \xrightarrow{\text{neutron capture}} {}^{A+1}_{Z}\mathrm{X}^{*} $$

This reaction may activate stable isotopes into unstable isotopes, leading to gamma emission during the de-excitation of the compound nucleus.

Attenuation Coefficient

The probabilities of neutron capture and scattering interactions are quantified by the effective interaction area of a single nucleus, commonly referred to as the "cross section", measured in barns (1 barn = 10^{-24} cm^2).

For a single isotope i:

$$ \sigma_{\text{total},i} = \sigma_{\text{scatt},i} + \sigma_{\text{abs},i} \tag{2.1} $$

Its attenuation coefficient μ_i, measured in cm^{-1}, can be derived via:

$$ \mu_{\text{total},i} = N_i \sigma_{\text{total},i} \tag{2.2} $$

where N_i is the isotope's atomic number density.

Material mixtures are common in bronze research. For a compound material such as bronze or brass, its total attenuation coefficient is:

$$ \mu = \sum \mu_{\text{total},i} \tag{2.3} $$

The probability that particles are transmitted through a material of thickness x is given by:

$$ T = e^{-\mu x} \tag{2.4} $$

Therefore, the intensity of the neutron beam transmitted through a material is calculated as:

$$ I = I_0 e^{-\mu x} \tag{2.5} $$

where I_0 is the initial flux (in unit of $n/cm^2/s$), and I is the transmitted intensity.

Projection and Reconstruction

In NT, the object is virtually divided into multiple unit voxels of thickness x along the neutron path, with each voxel representing a different material. The projection equation above is then rewritten as:

$$I = I_0 e^{-\sum_k \mu_k x} \tag{2.6}$$

where μ_k is the attenuation coefficient of voxel k.

Reconstruction refers to the process of solving for μ_k from measured projection data I:

$$\sum_k \mu_k = \frac{-\ln\left(\frac{I}{I_0}\right)}{x} \tag{2.7}$$

By acquiring projections from different angles, a system of linear equations (Equation 2.7) is formulated. The reconstruction process then is solving this system to obtain a 3D model, where the greyscale value of each voxel corresponds to its attenuation coefficient.

2.2.2 Neutron Beam

Figure 2.2 shows the beam profile of the FISH beamline, which reflects the spatial distribution of the neutron source. The neutron beam is Gaussian-distributed in both horizontal and vertical directions, on this basis, the beam profile can be simulated. The flux measured at the highest intensity position is 7.7×10^7 n/cm^2/s, which is almost two times higher than the previous flux [8] measured before a reactor upgrade. The energy distribution of the thermal neutron beam at output of the mirror system of FISH is obtained from the research performed in 1991 [35].

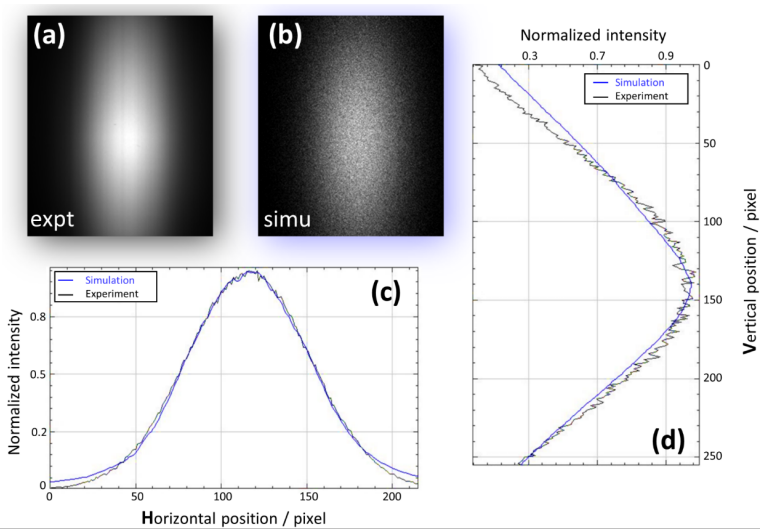

Figure 2.2: (a) and (b) Beam profile in the experiment and Geant4 simulation, where one binned pixel is 0.5 mm. (c) and (d) By assigning neutron positions with Gaussian distributions in both horizontal and vertical directions, the simulated neutron beam well represents the experimental beam.

2.3 Gamma Spectroscopy

GS is a technique that is capable to quantify elemental composition in a non-invasive manner. In this work, it measures the gamma emissions induced by the NT neutron irradiation, forming a series of gamma spectra. As shown in Figure 2.3, both the gamma peak energy and decay constant are characteristic of the isotope, enabling to identifying elements present in the object. In addition, the intensity of a gamma peak is proportional to the quantity of elemental atoms, allowing mass quantification. Since both neutrons and gamma rays are highly penetrating, the information carried by the gamma spectra comes from the entire bulk object. The elemental mass composition throughout the object can be determined by analysing each photonpeak. It is important to note that not all elements can be analysed by GS. For instance, lead (Pb) is commonly not detectable in GS.

2.3.1 Gamma Production

The gamma emissions are generated through neutron activation followed by radioactive decay. When a nucleus ${}^{A}_{Z}X$ captures a neutron, it forms an excited compound nucleus ${}^{A+1}_{Z}X^{*}$. This excitation energy comes mainly from the binding energy released as a result of the mass defect, with a smaller contribution from the neutron's kinetic energy. This excited nucleus typically de-excites promptly to its ground state ${}^{A+1}_{Z}X$, emitting gamma radiation which is the basis of prompt gamma neutron activation analysis (PGAA) [16, 17]. In some cases, the nucleus may transition to a long-lived metastable state, forming an isomer ${}^{A+1}_{Z}X^{m}$. The process is illustrated as:

$$ {}^{A}_{Z}\mathrm{X} + \mathrm{n} \xrightarrow{\text{neutron capture}} {}^{A+1}_{Z}\mathrm{X}^{*} \xrightarrow{\text{de-excitation}} {}^{A+1}_{Z}\mathrm{X}\,(\text{or } {}^{A+1}_{Z}\mathrm{X}^{m}) + \text{prompt } \gamma $$

If the de-excited product ${}^{A+1}_{Z}X$ is unstable, it then undergoes beta decay, producing a daughter nucleus Y^{*} in an excited state. The daughter nucleus then de-excites to its ground

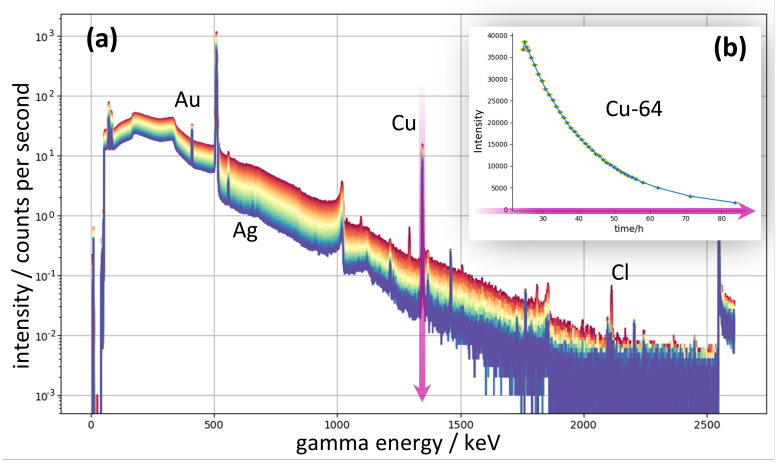

Figure 2.3: (a) A series of gamma spectra of the bronze statuette, the Kuvera (see Figure 4.1). (b) The radioactive decay of the gamma intensity of the peak at 1345 keV (emitted from Cu-64).

state, emitting delayed gamma rays randomly in all directions:

$$^{A+1}_{Z}X \xrightarrow{\beta \text{ decay}} Y^* \xrightarrow{\text{de-excitation}} Y + \text{delayed } \gamma$$

This delayed gamma emission can occur during or after neutron irradiation (NT), and it forms the basis of instrumental neutron activation analysis (INAA) [14, 15]. It also contributes to the GS measurements used in this work.

2.3.2 Interactions Between Gamma Emissions and Matter

Interactions

The gamma photons generated may interact with the bronze material itself, which is known as the self-attenuation effect. If the photons escape from the bronze, they may interact with objects in the surrounding environment, including the germanium crystal of the HPGe gamma detector. Figure 2.4 illustrates the attenuation coefficient of the three main types of photon interactions is strongly depend on the photon energy:

- **Pair Production and Annihilation**
  If the gamma energy exceeds 1022 keV, the photon may undergo pair production, creating an electron-positron pair with a total rest energy of 1022 keV. The excess energy is shared between the electron and positron as their kinetic energy. The positron eventually annihilates with an electron, emitting two 511 keV photons.

  If this occurs within the bronze, the kinetic energy is deposited locally, and only the annihilation photons may escape and be detected, contributing to the 511 keV peak in the gamma spectrum.

  If the original gamma photon escapes from the bronze and enters the detector, it may experience pair production inside the detector. In this case, the energy deposited may be: the full gamma energy (if all particles and photons are absorbed), the full energy minus 511 keV (if one annihilation photon escapes), or the full energy minus 1022 keV (if both annihilation photons escape).

- **Compton Scattering**
  A gamma photon may "scatter" off an atomic electron, when the photon energy greatly exceeds the electron's binding energy. The original photon vanishes, ejecting the electron and producing a scattered photon with lower energy. The energy lost is determined by the scattering angle, which follows the Klein-Nishina distribution.

  If Compton scattering occurs within the bronze, the photon is unlikely to be detected at its original energy. Given this, Compton-scattered gamma photons can be skipped in the GS simulation, as such photons are not taken into account in the analysis. However, if Compton scattering occurs inside the detector, the photon energy may be fully registered, unless the scattered photon escapes the detector, in which case it contributes to the Compton continuum.

- **Photoelectric Effect**
  When a gamma photon energy matches or slightly exceeds the electron's binding energy, the photon may be "absorbed" by an electron. The photon vanishes, transferring its entire energy to the electron, which is then ejected.

If this occurs within the bronze, the photon cannot be detected. If it occurs inside the detector, the energy is fully deposited.

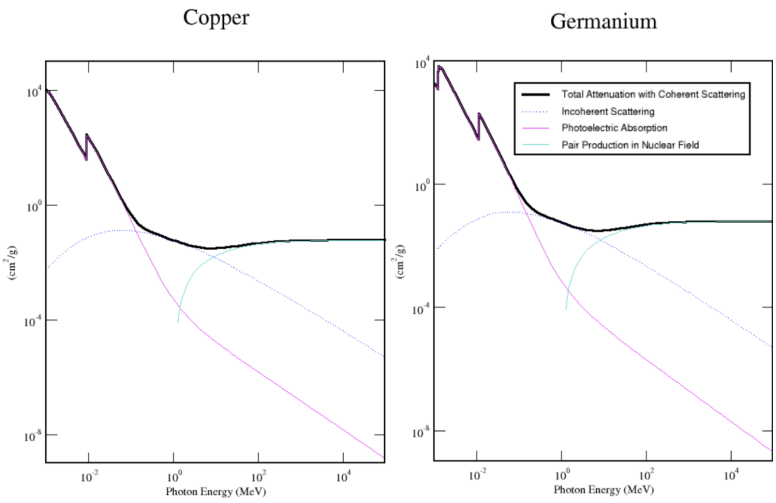

Figure 2.4: Photon mass attenuation coefficients for Cu (left) and Ge (right), obtained from the NIST database [36]. In both cases, the photoelectric effect, Compton scattering (incoherent scattering), and pair production dominate in the low-, medium-, and high-energy ranges, respectively.

Attenuation Coefficient

Similar to neutrons, the probability of gamma-ray interactions with matter is quantified using the attenuation coefficient μ (in units of cm^{-1}), whose value is typically derived from elemental cross section data using the Equations 2.2 and 2.3. As with neutrons, the transmission probability of gamma photons through a material is given by Equation 2.4.

2.3.3 Key Experimental Parameters

Detector Efficiency

For a point source, gamma photons are emitted uniformly in all directions, but only a portion of these photons reach the detector, as illustrated in Figure 2.5. This fraction defines the geometrical efficiency of the detector, which is given by:

$$\epsilon_{\text{geo}} = \frac{\text{photons hitting detector}}{\text{photons emitted}} = \frac{\Omega}{4\pi} \tag{2.8}$$

where Ω is the solid angle subtended by the detector at the location of the point source.

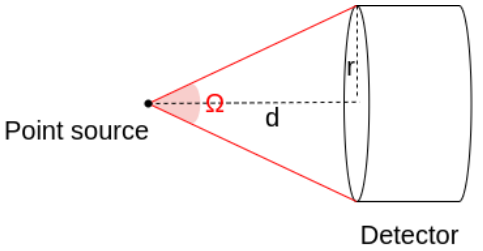

Figure 2.5: Geometry between a point source and a gamma detector. The source is positioned along the detector's central axis. The solid angle Ω is defined by the detector radius r and the source-to-detector distance d, and is calculated by: $\Omega = 2\pi\left(1 - d/\sqrt{d^2 + r^2}\right)$.

As discussed, those photons that reach the detector may interact with the germanium crystal, but only those that deposit all their energy within the crystal contribute to the full-energy peak in the spectrum. The fraction of emitted gamma photons that result in such full-energy events defines the full-energy peak efficiency, given by:

$$\epsilon = \frac{\text{Photons fully deposited}}{\text{Photons emitted}} = \epsilon_{\text{geo}} P_{\text{abs}} \tag{2.9}$$

where P_{abs} is the probability that a photon is fully absorbed within the detector. Since photon interaction depends on energy, the full-energy peak efficiency is energy-dependent.

Geometrical efficiency can be directly calculated using Equation 2.8, while full-energy peak efficiency is usually determined through calibration with reference sources of known radioactivity. For this purpose, experts from the INAA lab at TU Delft developed a computer program [37, 38], which is also used in this work. The obtained full-energy peak efficiency is then used in Method 1 to determine elemental masses from GS.

Detector Dead Time

When the incoming photon rate is high, the detector can become temporarily unresponsive, causing a dead time and fewer detected gamma counts. The true counts of detected gamma photons can be recovered by correcting for dead time using dead-time percentage, which is calculated as:

$$\%DT = 200 * \frac{T_D}{T_R} \tag{2.10}$$

where T_R is the real (measurement) time, and T_D is the total dead time during the measurement.

3

Validation of 1D Self-attenuation Corrections in Mass Quantification

Direct analysis of gamma spectroscopy data collected after neutron tomography enables the identification of elements and estimation of their masses. However, in heritage science, accurate mass quantification is often challenged by corrections for self-attenuation of both neutrons and gamma rays, as artefacts are typically large and complex in both shape and composition. Compared to traditional INAA-based approaches, the method presented in this chapter uses a "matchbox" model to simplify object geometry, reducing the complexity of self-attenuation corrections from 3D to 1D while retaining the key physical factors involved. It also accounts for object rotation during neutron irradiation, making it applicable to neutron tomography experiments. The chapter details the method with a focus on the 1D self-attenuation correction approach. It demonstrates the method using benchmark objects of known composition, showing significant improvements in mass accuracy after applying the corrections. The method is further applied to three archaeological bronze artefacts of increasing complexity, demonstrating both its effectiveness and limitations across different object types.

This chapter is based on the publication: Cantini, F., Creange, S., **Li, Y.**, van Eijck, L., Kardjilov, N., Kabra, S., & Grazzi, F. (2024). Morphological and microstructural characterization of an ancient Chola bronze statuette by neutron-based non-invasive techniques. *Archaeological and Anthropological Sciences*, 16(3), 45.

3.1 Introduction

Neutron tomography (NT) utilizes highly penetrating neutrons to probe objects' interior structures, inherently inducing the emission of (delayed) gamma rays that are specific to isotopes and are able to penetrate objects deeply. These gamma rays carry valuable composition information from the interior (pristine) materials. If we perform subsequent gamma spectroscopy (GS), this activation radiation can be efficiently exploited for the quantification of interior elemental composition based on the measured gamma spectra, as illustrated in Figure 3.1.

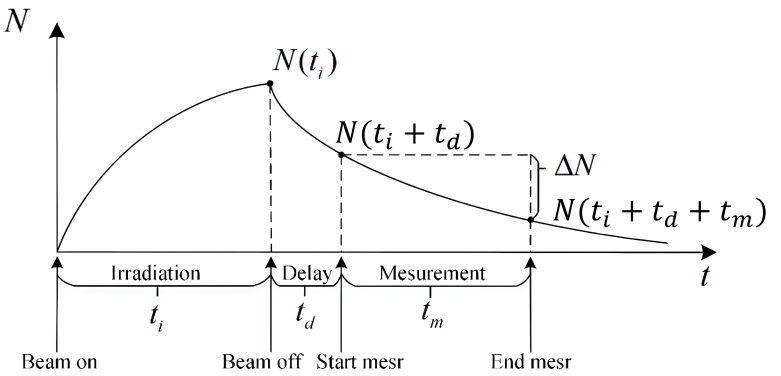

Figure 3.1: Schematic of the number of radioactive nuclei N as a function of time t in a NT and subsequent GS experiment. $N(t)$ increases during the irradiation time t_i, reaching a maximum $N(t_i)$ at the end of NT. It then decreases due to radioactive decay, which is accompanied by gamma emission. After a delay period t_d, the gamma activity is measured for a duration t_m. During this time, the number of radioactive nuclei decreases by $\Delta N = N(t_i + t_d) - N(t_i + t_d + t_m)$, which is proportional to the number of delayed gamma rays measured by GS, enabling elemental mass quantification.

In heritage research, objects are typically on the centimetre scale. For such bulk objects, both the incoming neutron beam and the outgoing gamma rays experience significant self-attenuation within the objects. This often results in a substantial underestimation of elemental mass unless proper corrections are applied. However, due to the complexity of object shapes and internal compositions, calculating these corrections can be extremely. Therefore, direct mass quantification from GS is more practical for simpler objects with regular geometry and homogeneous compositions.

The researchers, from the INAA lab at TU Delft, have been investigating how to apply INAA to large mineral samples since the 1990s. Their work has led to numerous advancements in the field, including the specific irradiation facility BISNIS [39] and measurement system [40] as well as great developments in analysis [15, 26, 41–48]. However, these methods are not suited to our case where objects could contains different discernible materials (e.g., bronze with a corroded surface) and irradiation is delivered through NT.

Inspired by their work, I developed a mass quantification method based on the absolute quantification from GS, but tailored for bronze objects with regular geometry and relatively homogeneous composition, with proper consideration of objects' rotation during neutron irradiation. This method simplifies the correction of self-attenuation effects by effectively

modelling the object as a "matchbox", thereby reducing the complexity of correction calculations from 3D to 1D.

This chapter outlines the approach for quantifying elemental masses from GS measurements and details the implementation of 1D self-attenuation corrections using the matchbox model. This method was validated using reference samples of known compositions. Its application is further demonstrated on three ancient bronze objects: a dagger fragment, a pendant from the Shiva statuette, and a solid cast the Kuvera statuette, showcasing the method's feasibility for objects of varying sizes, shapes and composition complexity.

3.2 Mass Quantification from Gamma Spectroscopy

3.2.1 Theoretical Calculation

Activation Accumulation

N_0 is the number of target isotopes that present in the object, given by:

$$N_0 = \frac{m\theta}{M_a} N_A \tag{3.1}$$

where m is the mass of the target element, θ and M_a are the isotopic abundance and atomic mass of the target isotope respectively, and N_A is Avogadro's number.

During neutron irradiation, the reaction rate R per isotope absorbing one neutron and becoming radioactive is defined by:

$$R = \phi_0 \sigma \tag{3.2}$$

where ϕ_0 is the incident neutron flux, and σ is the neutron absorption cross section of the target isotope.

The net production rate of the radioactive isotope is:

$$\frac{dN(t)}{dt} = RN_0 - \lambda N(t) \tag{3.3}$$

where $N(t)$ is the number of nuclei at irradiation time t, and λ is the decay constant. $\lambda N(t)$ is the decay rate of the radioactive isotope. Then, $N(t)$ is derived as:

$$N(t) = \frac{RN_0}{\lambda}(1 - e^{-\lambda t}) \tag{3.4}$$

Decay and Gamma Counts

After irradiation, the number of radioactive isotopes decays exponentially:

$$N(t) = \frac{RN_0}{\lambda}(1 - e^{-\lambda t_i})e^{-\lambda(t - t_i)} \tag{3.5}$$

where t_i is the irradiation time.

The number of decayed radioactive isotopes during measurement time t_m starting at delayed time t_d is:

$$\Delta N = N(t_i + t_d) - N(t_i + t_d + t_m) = \frac{RN_0}{\lambda}(1 - e^{-\lambda t_i})e^{-\lambda t_d}(1 - e^{-\lambda t_m}) \tag{3.6}$$

Of these decays, a fraction of them induce the target gamma ray. In addition, a fraction of the induced gamma rays are measured by the gamma detector. The number of detected gamma counts C is:

$$C = \Delta N \Gamma \epsilon \tag{3.7}$$

where ϵ is the full-energy peak efficiency (see Section 2.3.3), and Γ is the probability of the radioactive isotope emitting the target photon.

Quantifying Elemental Mass from Gamma Counts

According to Equations 3.1, 3.2, 3.6, and 3.7, the elemental mass m is related to the measured gamma counts C as:

$$m = \frac{C}{\frac{\theta}{M_a} N_{av} \phi_0 \sigma \frac{1}{\lambda}(1 - e^{-\lambda t_i}) e^{-\lambda t_d}(1 - e^{-\lambda t_m}) \Gamma \epsilon} \tag{3.8}$$

In the gamma spectra, C is the net area of the photopeak, determined through a fitting of the peak using a Gaussian model and commonly following a dead-time correction (see Section 2.3.3).

3.2.2 Measurement Strategy in Practical Bronze Research

Theoretically, the total gamma count C collected by the detector is given by the time integration of the gamma activity $A(t)$:

$$C = \int A(t)\, dt \tag{3.9}$$

$A(t)$ is proportional to the decay rate of the radioactive nuclei, which is itself proportional to the number of activated atoms $N(t)$:

$$A(t) \propto \lambda N(t) \tag{3.10}$$

Based on the expressions for $N(t)$ during and after irradiation (see Equations 3.4 and 3.5), the time-dependent gamma activity can be expressed as:

$$A(t) \propto R N_0 \left(1 - e^{-\lambda t}\right), \quad \text{during irradiation } (0 < t \leq t_i) \tag{3.11}$$

$$A(t) \propto R N_0 \left(1 - e^{-\lambda t_i}\right) e^{-\lambda (t - t_i)}, \quad \text{after irradiation } (t > t_i) \tag{3.12}$$

These relations imply that short-lived isotopes reach their maximum activity sooner and decay faster than long-lived isotopes. In practice, this strongly influences the peak-to-background ratio, especially for short-lived nuclides.

Bronze Example

After neutron irradiation of bronze, both Cu-64 (with a half-life of 12.7 h and characteristic gamma peak at 511 keV) and Sn-125m (with a half-life of 9.52 min and characteristic gamma peak at 332 keV) can be produced. A typical NT scan lasts several hours, activating large amounts of Cu-64. If counting begins only after the scan, Cu-64 dominates the spectrum and its high-energy gamma rays raise the Compton continuum, masking the 332 keV tin peak.

Optimising the timing

When isotopes with widely different half-lives are present, three time parameters must be chosen carefully:

- **Irradiation time** t_i: long enough for activation, but short enough to limit long-lived background.
- **Delay time** t_d: as short as practicable for detecting short-lived nuclides.
- **Measurement time** t_m: long enough for statistical precision, yet not so long that short-lived peaks disappear into background.

For Sn-125m we therefore use a short irradiation (minutes rather than hours) before the NT scan, start counting immediately, and stop after roughly five half-lives of Sn-125m. This maximises the Sn-125m signal while minimising the Cu-64 background, preserving an adequate peak-to-background ratio in the low-energy region.

3.2.3 1D Self-Attenuation Corrections Using a Matchbox Model

The mass calculation in Equation 3.8 is the ideal, assuming both neutrons and gamma rays traverse the sample without attenuation. Introducing correction factors N^* (neutron) and G^* (gamma), we write:

$$m = \frac{C}{\frac{\theta}{M_a} N_{av} \phi_0 N^* \sigma \frac{1}{\lambda}(1 - e^{-\lambda t_i}) e^{-\lambda t_d}(1 - e^{-\lambda t_m}) \Gamma G^* \epsilon} \tag{3.13}$$

The correction factors are the transmission probabilities given by Equation 2.4:

$$N^* = e^{-\mu_n l_n}, \quad G^* = e^{-\mu_g l_g} \tag{3.14}$$

where attenuation coefficients (μ_n and μ_g) and transmission paths (l_n and l_g) are determined by a consideration of objects' geometry and orientation.

A Matchbox Model for Geometry Approximation

As shown in Figure **??**, we use a matchbox, which is of the same volume as the object, to approximate the object's size and shape. Considering that ancient bronzes are commonly covered by a corrosion layer which is always associated with hydrogen, which has big impact of neutron attenuation, the model contains two different materials: an outer layer of bronze corrosion and the inner core that is the pristine bronze material. Given parallel-emitted neutrons and assuming the induced gamma rays propagate in the same direction, the attenuation variation in the height direction is negligible, reducing the calculation complexity from 3D to 2D. Therefore, the model is designed to consist of long rectangular voxels. In addition, choosing the given voxel as the origin of the reference rotation coordinate system further simplifies the calculation difficulty to 1D. We consider the total gamma counts C is a sum up of counts from each voxel k, Equations 3.7 is rewritten as:

$$C = \sum_{k=1}^{K} C_k = \sum_{k=1}^{K} \frac{m_k \theta}{M_a} N_{av} \phi_0 N_k^* \sigma \frac{1}{\lambda}(1 - e^{-\lambda t_i}) e^{-\lambda t_d}(1 - e^{-\lambda t_m}) \Gamma G_k^* \epsilon \tag{3.15}$$

where m_k is the elemental mass of the voxel and is assumed uniform in this model:

$$m_k = \frac{m}{K} \tag{3.16}$$

where K is the total number of voxels.

Then the total mass is:

$$m = Km_k = \frac{C}{\sum_{k=1}^{K} \frac{1}{K} \frac{\theta}{M_a} N_{av} \phi_0 N_k^* \sigma \frac{1}{\lambda} (1 - e^{-\lambda t_i}) e^{-\lambda t_d} (1 - e^{-\lambda t_m}) \Gamma G_k^* \epsilon} \tag{3.17}$$

where the self-attenuation correction factors are:

$$N_k^* = e^{-(\mu_{n_shell,k} l_{n_shell,k} + \mu_{n_core,k} l_{n_core,k})}, \quad G_k^* = e^{-(\mu_{g_shell,k} l_{g_shell,k} + \mu_{g_core,k} l_{g_core,k})} \tag{3.18}$$

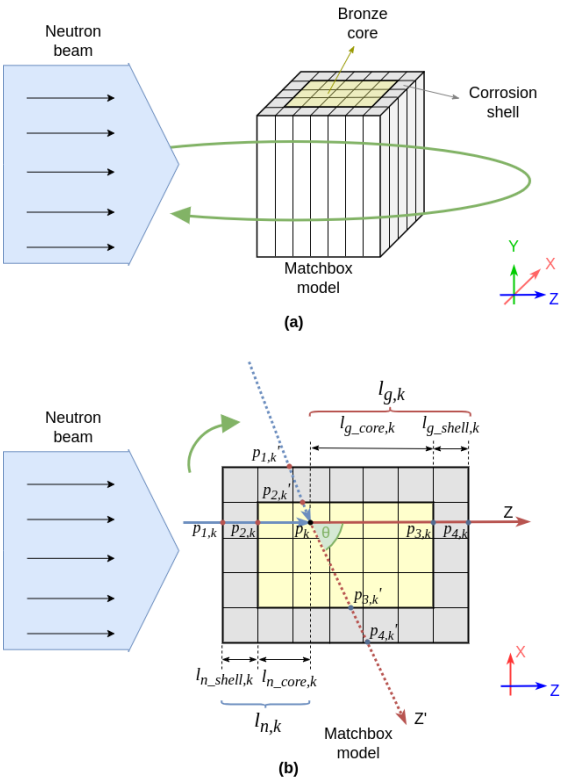

Figure 3.2: Schematic of approximating the bronze object by a matchbox model in the mass calculation. (a) A 3D view of the matchbox model in the experiment, where neutron beams rotate around the model. (b) The top view of the setup. For each voxel, the paths of neutron and gamma ray are assumed to cross its centre. The transmission paths can be calculated by determining the distances of the intersections between the particles' trajectories and the boundaries of the shell and the core.

Accounting for Orientation-dependent Irradiation during NT

Considering rotation during NT, each orientation j has its own correction factors, irradiation time, and delayed time (see Figure 3.3):

$$m = \frac{C}{\sum_{j=1}^{J}\sum_{k=1}^{K}\frac{1}{K}\frac{\theta}{M_a}N_{av}\phi_0 N^*_{k,j}\sigma\frac{1}{\lambda}(1-e^{-\lambda t_{i,j}})e^{-\lambda t_{d,j}}(1-e^{-\lambda t_m})\Gamma G^*_{k,j}\epsilon} \tag{3.19}$$

$$N^*_{k,j} = e^{-(\mu_{n_shell,k,j}l_{n_shell,k,j}+\mu_{n_core,k,j}l_{n_core,k,j})}, \quad G^*_{k,j} = e^{-(\mu_{g_shell,k,j}l_{g_shell,k,j}+\mu_{g_core,k,j}l_{g_core,k,j})} \tag{3.20}$$

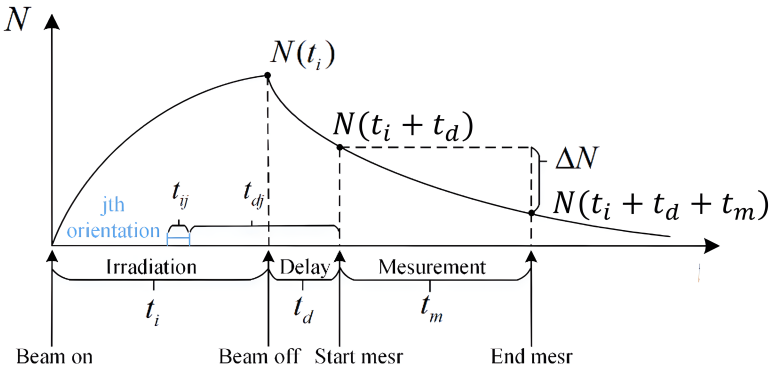

Figure 3.3: For each orientation, the irradiation starts at a different time, and the new delayed time is the global delayed time plus the rest of irradiation time.

3.3 Method Validation

This is a general method, with the goal of calculating elemental masses under a consideration of both self-attenuation effects of the object and its rotation during the irradiation. We use an experiment with benchmark objects of known composition to evaluate this method and demonstrate its accuracy.

3.3.1 Experiment and Materials

One object is a stack consisting of an iron alloy (steel 37-2) cube, a copper cube, and a titanium alloy cylinder (Ti6Al4V). This object was rotated during the NT experiment of projections (500 orientations). For comparison, a copper foil was placed against the scintillator and irradiated without rotation, as shown in Figure 3.3.1. After an irradiation of approximately 2 hours, each of the assemblies was measured by GS following the order of titanium alloy cylinder, copper foil, copper cube, and iron alloy cube.

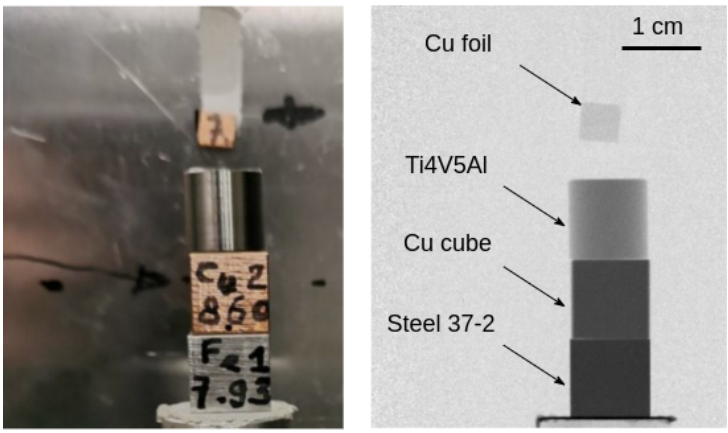

Figure 3.4: Benchmark samples used in the experiment: (a) a stacked assembly with a Cu foil in the FISH beamline; (b) a neutron projection image.

3.3.2 Results and Discussion

As shown in Table 3.1, for all investigated materials, the calculated mass from GS without corrections for neutron and gamma self-attenuation effects is consistently lower than the corresponding weighed mass. After applying the corrections, the calculated masses increase significantly, and the average relative error improves from 42% to 22%.

For the copper cube and copper foil, this method effectively compensates for self-shielding effects regardless of whether the object rotates during neutron irradiation or not. Notably, the improvement is more substantial for larger samples, where attenuation along the particle's transmission path is greater. In the copper cube (10 mm thick), the correction reduces the relative error by approximately 60%, while in the thinner copper foil (1 mm thick), the improvement is approximately 16%.

For alloy objects, a noticeable improvement is observed for Ti, which constitutes approximately 90 wt% of the Ti6Al4V cylinder. In contrast, the other two components V (approximately 4 wt%) and Al (approximately 6 wt%) show no improvement in their relative errors after correction, despite having reasonable signal-to-noise ratios in their gamma peaks. A similar situation is seen in the steel object, where Mn (0.04 wt%) exhibits no noticeable improvement. However, this does not necessarily imply that major alloying elements benefit more from attenuation correction than minor elements. The alloying elements are homogeneously distributed and should experience similar neutron and gamma attenuation. A more plausible explanation is the variation between the actual and nominal compositions of these industrial alloys. While the primary elements are present in relatively stable proportions, small-mass-fraction elements may deviate more significantly. This compositional deviation can contribute to the discrepancies in mass determination that are not related to the limitations of the attenuation correction itself, and this will not be a problem of analysing bronzes.

Furthermore, the accuracy of this GS method depends on the activation probability of the isotope. For example, Fe-59 is the only viable gamma-emitting isotope that can be used for iron analysis, but it provides a weak signal due to the low natural abundance of

Table 3.1: Comparison of elemental masses calculated from GS with and without corrections for neutron and gamma self-attenuation.

Object	Element	Weighed [g]	GS w/o corr. [g]	Rel. error [%]	GS w/ corr. [g]	Rel. error [%]
Cu foil	Cu	0.22	0.15 ± 0.01	32 ± 2	0.16 ± 0.01	27 ± 2
Cu cube	Cu	8.60	5.02 ± 0.05	42 ± 1	9.78 ± 0.15	15 ± 1
	Ti	3.15	2.14 ± 0.03	32 ± 1	3.40 ± 0.04	8 ± 1
Ti6V4Al	V	0.14	$0.12 \pm < 0.01$	$14 \pm < 1$	$0.17 \pm < 0.01$	$21 \pm < 1$
	Al	0.21	$0.17 \pm < 0.01$	$19 \pm < 1$	$0.25 \pm < 0.01$	$19 \pm < 1$
Steel 37-2	Fe	7.79	2.00 ± 1.20	74 ± 15	8.00 ± 4.00	3 ± 51
	Mn	0.11	$0.02 \pm < 0.01$	$82 \pm < 1$	$0.04 \pm < 0.01$	$64 \pm < 1$

Note: GS = Gamma Spectroscopy. Values with ± indicate uncertainty. Relative error is calculated against the weighed value Corrections refer to neutron and gamma self-attenuation effects. The uncertainty arises from the peak-fitting procedure. Values like < 0.01 indicate well-fitted peaks.

its parent isotope Fe-58 (0.28%), combined with a short irradiation time (2 hours) relative to its 44-day half-life. These factors result in low signal-to-noise ratios in the gamma peak of Fe-59, reducing its mass calculation accuracy.

In general, the GS method with self-attenuation correction is applicable and effective for quantifying elemental mass in bulk metallic materials from am NT experiment, when the isotopes of interest present in sufficient quantities and can be properly activated. Research of bronzes meet such criteria, as both the main elements Cu and Sn and trace elements such as As, Sb, Mn, In have proper half-lives and can be properly activated, making this GS method well-suited for analysing their mass composition. It is also a common situation that there are precious metals Ag and Au involved in bronzes for ritual purposes, this GS method can also help quantify their mass to some extent or derive their mass percentage that also allow us to understand more about the material that used by the artist and the customs of that social society.

3.4 Applications

This method is applied to three different ancient bronze objects that vary in size, shape, and homogeneity, showcasing its feasibility to different extents.

The dagger fragment (Figure 3.5a) is a typical simple bronze object, which has a flat, rectangular shape and nearly uniform composition. By contrast, the Shiva's "J-shaped" pendant (Figure 3.6a) has less shape regularity. It is a very small inlay in the necklace and appears homogeneous from NT. The Kuvera statuette (Figure 4.1a) with a mysterious deposit hidden within its pedestal is an exampleof an object with highly complex shape and composition.

3.4.1 Dagger Fragment

The dagger fragment shown in Figure 3.5 was found by Dutch metal detectorists in a valley in the Netherlands. Its uniqueness promptly drew the attention of the Cultural Heritage Agency of the Netherlands, which initiated a multidisciplinary investigation, including non-destructive neutron analysis conducted at TU Delft. NT was first performed to visualise the interior structure of the fragment (Figure 3.5b), followed by GS for elemental composition analysis. The fragment was irradiated for a total of 4 hours during NT, and

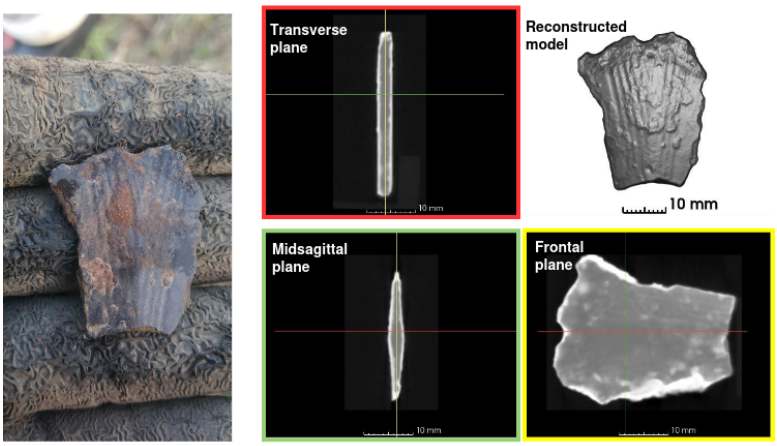

Figure 3.5: Dagger fragment [49] discovered by enthusiastic private finder Wim and Nico van Schaijk in the Aa valley in 2021. (a) Two bands of parallel-line decoration and remains of two rivet holes suggest it may have been part of a grooved ogival dagger, similar to the one found in Annertol (Figure A.1). (b) Three cross-sections of its NT model reveal a homogeneous interior core (grey) completely covered by a corrosion layer (white).

the GS measurements continued for approximately 5 days.

By measuring the reconstructed 3D computer model, the total volume of the fragment was calculated to be 2.13 cm^3, comprising a 0.87 cm^3 corrosion layer and a 1.26 cm^3 uncorroded bronze core. A "matchbox" model (3.6 cm high, 2 cm wide, 0.175 cm thick) with a corrosion-layer thickness of 0.06 cm was used for self-attenuation corrections in the GS analysis. The corrosion layer was assumed to contain hydrogen, as suggested by its strong neutron attenuation in the NT model. XRF measurements of the fragment's surface indicated a composition rich in tin (50 wt%), iron (30 wt%), and copper (20 wt%). The corrosion layer was therefore modeled with these components plus an assumed 0.1 wt% hydrogen. The core was initially assumed to be 90 wt% copper and 10 wt% tin, later refined based on the GS results.

Table 3.2: Elemental mass composition of the dagger fragment calculated from the GS data.

Element	**Mass [g]**	**wt [%]**
Cu	8.4± < 0.1	82.5
Sn	1.2± < 0.1	11.8
Fe	0.5 ± 0.1	4.9
As	0.06± < 0.01	0.59
Cl	0.02± < 0.01	0.20
Sb	0.01± < 0.01	0.10
Mn	0.001± < 0.01	0.01
Na	0.0005± < 0.0001	0.005
In	0.0001± < 0.0001	0.001
Au	0.00003± < 0.00001	0.0003
Total	**10.19**[a]	**100**

[a] Weighed mass is 10.2 g

Table 3.2 shows the bulk elemental composition averaged over the entire dagger fragment. The dagger consists predominantly of 83 wt% Cu and 12 wt% Sn. Given the XRF surface measurement of 20 wt% Cu in the corrosion layer, the pristine bronze core likely contains a higher Cu content than the bulk average. Notably, around 5 wt% Fe was detected by GS, likely originating from groundwater rather than the original bronze alloy, consistent with the stream landscape where the fragment was found. Iron in the water can oxidise

to form iron(III) oxide, Fe_2O_3, which can further hydrate into $Fe_2O_3 \cdot xH_2O$ [50]. This hydrated compound is one of the primary components of rust and is responsible for the brown corrosion products visible in Figure 3.5a.

Chlorine may be introduced as NaCl from handling (salt on people's hands is commonly found on museum objects). However, in our measurements the Cl concentration is much higher than Na, arguing against simple surface NaCl contamination and instead suggesting that Cl is bound to Cu in corrosion phases—most plausibly cuprous chloride (CuCl) and possibly copper hydroxychlorides—known to accelerate bronze corrosion [51, 52]. Given its low overall concentration, it is unlikely to be of significant concern.

In addition to the major elements, trace amounts of arsenic, antimony, and manganese were found, all commonly associated with bronze alloys [53]. We also detected a very small quantity of gold, which may have originated from groundwater, may have been a trace inclusion in the original alloy, or may have been intentionally added to produce black bronze [54]. The calculated total mass of 10.19 g agrees with the weighed mass of 10.2 g, indicating an error below 1%.

3.4.2 Shiva's Pendant

The Shiva statuette (Figure 3.6a) is a solid-cast Indian statuette with stylistic features of the Chola Dynasty [55], housed at the Rijksmuseum in Amsterdam. To investigate its internal structure and the relevant ancient casting skills, the object has been non-invasively studied by researchers across institutions [4], using neutron techniques including NT in Berlin and Delft [8, 56], neutron diffraction (ND) in Oxford [57], GS in Delft [58].

Unexpectedly, NT revealed that the small pendant on the necklace attenuates neutrons much more strongly than the surrounding bronze (Figure 3.6b). ND further showed that

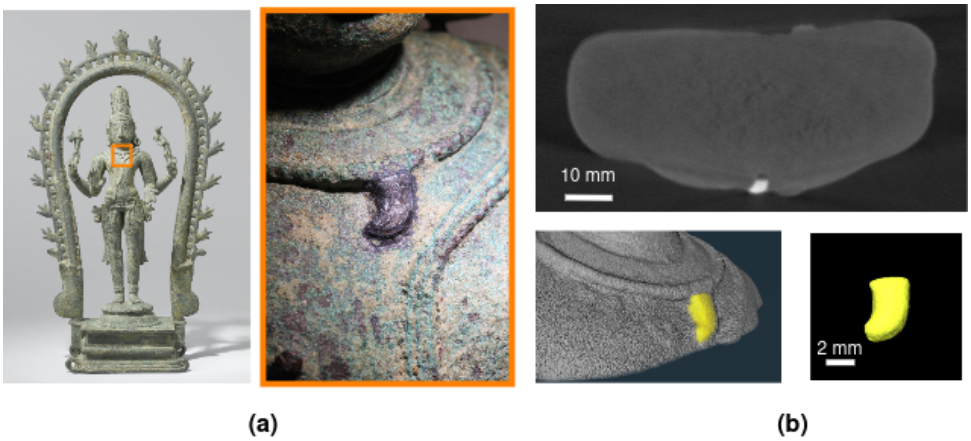

Figure 3.6: Bronze statuette representing the Indian deity Shiva (no.AK-MAK-1291, c. 1000-1200 AD, the Rijksmuseum Amsterdam). (a) The Shiva bronze statuette showing the necklace with pendant; the pendant appears much darker than the main bronze material. (b) NT model of this statuette. A top-view cross section slice shows the pendant is of highly neutron-penetrating (top). By segmenting the pendant, it has a volume of approximately 50 mm^3 (bottom).

the pendant is composed principally of Ag, Au, or a combination of the two. However, ND alone cannot distinguish Ag and Au because of their almost identical face-centred-cubic lattice constants (4.086 Å for silver and 4.078 Å for gold). By contrary, this is not a problem for GS, as the principal gamma emissions of gold and silver are discernible (658 keV for silver and 412 keV for gold). This provided the motivation for a dedicated GS experiment on the pendant.

The statuette's chest was irradiated for 22.5 h with the object facing upstream (towards the neutron beam). GS spectra were collected for approximately 6 days with the pendant facing the detector at a distance of 3 cm. This front-facing orientation limited the analysis to the pendant, allowing us to neglect self-attenuation by the surrounding bronze. The GS measurements (Figure 3.7) confirmed the presence of both Au and Ag.

Although the pendant is irregular in shape, its size is appropriately approximated using a "matchbox" of 3.1×5×3.2 mm^3 (equivalent pendant volume derived from NT). Using this volume for self-attenuation corrections, we obtain masses of (0.010 ± 0.003)g Au and (0.59 ± 0.01), g Ag (Table A.1), corresponding to an Au:Ag mass ratio of roughly 1:59. From a manufacturing point of view, the pendant can be considered as silver. A cross-check shows that the elemental masses imply a total metal volume of 56mm^3, only 12% higher than the 50mm^3 derived from NT and well within the 22% benchmark uncertainty.

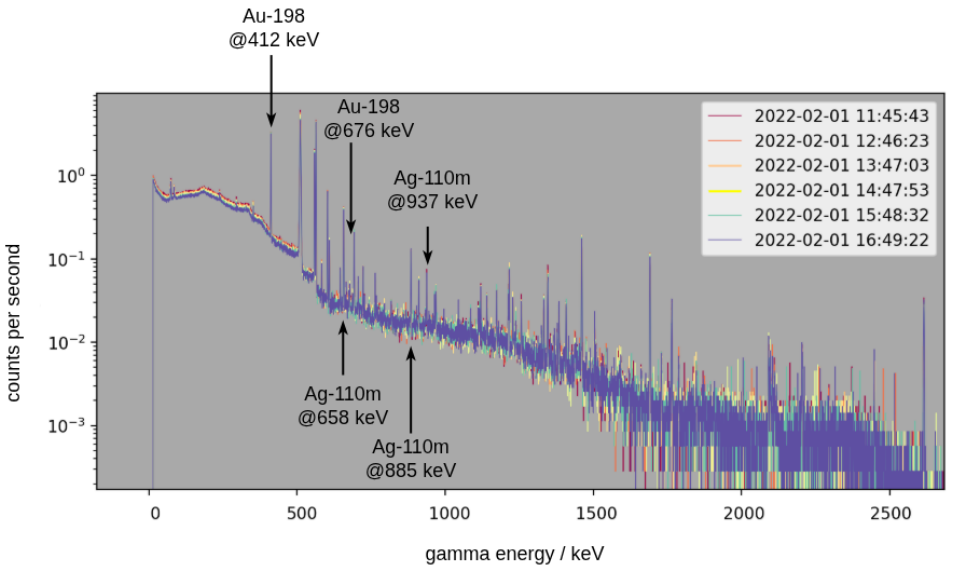

Figure 3.7: Last six gamma spectra acquired for the GS experiment on the Shiva's pendant. Characteristic gamma peaks of both gold and silver are present.

3.4.3 Kuvera Statuette

The Kuvera statuette (Figure 4.1a) is a solid-cast bronze housed at the Rijksmuseum in Amsterdam and originating from Java, Indonesia. Although only 11 cm tall, it shows a very high level of fine surface detail that appears to be as-cast (i.e., not chiselled after casting). Neutron tomography (NT; Figure 4.1c) revealed a heterogeneous internal structure due to bronze phase segregation and corrosion, as well as a folded foil sealed within the pedestal. A short tail of this foil is visible externally and appears yellowish, suggesting it may be gold. Preliminary XRF analysis confirmed the presence of gold, although the possibility of silver could not be ruled out (Table A.2). In this section, we present the determination of the statuette's bulk elemental composition via the GS-based mass quantification. A more comprehensive simulation-based analysis, which considers the multiple bronze materials and the internal foil, is presented in the following chapter.

Table 3.3: Bulk elemental masses of the Kuvera statuette derived from GS data.

Element	Mass [g]	wt[%]
Cu	486 ± 3	82.4
Sn	100 ± 2	16.9
Ag	1.5 ± 0.31	0.25
Cl	0.93 ± 0.19	0.16
Co	0.53 ± 0.11	0.090
As	0.58 ± 0.12	0.098
Au	0.38 ± 0.01	0.064
Sb	0.12 ± 0.01	0.020
Na	0.028 ± 0.001	0.0048
Mn	0.0046 ± 0.0003	0.00078
Total	**590**[a]	**100.0 %**

[a] Weighed mass is 488 g.

The experimental scheme comprised a 30 min irradiation followed by GS for short-lived isotopes such as Sn, then a 23.5 h NT scan and subsequent GS over three days (see the gamma spectra collected from the GS experiment of the Kuvera statuette in Figure 2.3). Despite the statuette's complex shape and internal material structure, a $2 \times 3 \times 11 \text{cm}^3$ "matchbox" volume adequately approximates the self-attenuation path lengths. The outer ≈ 0.05 cm corrosion shell was modelled with 77 wt% Cu, 21 wt% Sn and 0.025 wt% H (from surface XRF), while the bronze core was assumed to be 90 wt% Cu and 10 wt% Sn, whose composition was refined to match the GS results.

Tabel 3.3 lists the resulting bulk composition which is an average over the entire object volume. As expected, gold is present, while a more noticeable amount of silver is detected. They are most likely from the foil, according to the XRF results. However, these Ag and Au masses cannot explain the foil composition. The summed calculated masses exceed the weighed mass by 21 %, still within the 22 % benchmark uncertainty, but more precise determination of the foil composition and different bronze materials requires modelling their actual shape and position inside the object, which will be addressed in the simulation-based analysis in the next chapter.

3.5 Conclusion

This GS-based mass quantification method provides deeper insights into the overall composition of large, bulk bronze artefacts, far beyond the capabilities of XRF, which is also non-destructive but only probes the metal surface. Compared to conventional INAA methods for large objects, this method allows for more flexible irradiation scenarios, including cases with or without object rotation. In addition, a "matchbox" model is used to approximate objects, regardless of their size, shape, and composition, simplifying the

self-attenuation corrections from a 3D problem to a 1D estimate.

The ability of this method to identify elements and quantify elemental composition based on GS data has been validated using benchmark objects, with an average uncertainty of 23%. This method was then applied to three bronze artefacts:a dagger fragment, where both shape and composition match the matchbox model closely; Shiva's pendant, which has an irregular shape but simple composition; and the Kuvera statuette, which features both complex shape and composition. The corresponding accuracy of the GS-based results ranged from below 1%, to 5%, and up to 21%, respectively, clearly showing that the method performs better when applied to objects with more regular shapes and more homogeneous composition.

Overall, this method is effective, providing a good overview of an object's composition in terms of the elements present and their estimated masses from the overall volume, allowing one to determine both the internal structure (from NT) and the bulk, pristine composition (from GS) within a single experimental time slot. It is especially well-suited for non-destructive estimation of elemental composition in relatively simple artefacts, such as swords or daggers. Moreover, the results can be used as initial composition assumptions in simulation-based methods for more accurate element assignment and quantification, which is discussed in the next chapter. Taken together, this approach allows one to rapidly determine both the internal structure (from NT) and the bulk, pristine composition (from GS) within a single experimental time slot.

4

Geant4-based Iterative Simulation Method for Element-to-Source Material Assignment and Compositional Quantification

By performing gamma spectroscopy after neutron tomography, the interior elemental composition of artefacts can be obtained "for free". While direct analysis of gamma data allows estimation of bulk composition averaged over the artefact volume, it lacks spatial resolution and cannot distinguish between different internal materials. This limitation is especially critical for artefacts with complex composition, such as the ancient Indonesian solid-cast bronze statuette, the Kuvera, which contains a concealed deposit. Neutron tomography provides the needed spatial information, and ray-tracing simulations can account for the object's shape and material heterogeneity. Inspired by this, a Geant4-based iterative simulation approach is proposed in this chapter, fusing neutron tomography and gamma spectroscopy datasets, thus allowing the assignment of identified elements to their specific source materials and the quantification of their respective compositions. This chapter outlines the core principle of this method and demonstrates the extent of its quantification capability on bulk objects of known composition. It further showcases its practical application to the Kuvera statuette, through which we gain insights into how the pristine inner bronze segregated to a composition different from that of the surrounding shell. Similarly, the method allows us to quantify the composition of the hidden offering in the statuette that consecrates the bronze for worship purposes.

This chapter is based on the publication: **Li, Y.**, Creange, S., Zhou, Z., Southworth, W., Pappot, A., & van Eijck, L. (2024). Exploiting

4.1 Introduction

The Kuvera (Figure 4.1a) is a solid bronze statuette from Indonesia, crafted to honour the god of prosperity, known as Kuvera in Hinduism or Jambhala in Buddhism. This statuette, only 11 cm in height, impresses with its intricate details, such as jewellery and a mongoose in its left-hand spewing pearls or coins, vividly depicting an image of wealth and demonstrating the casting craftsmanship of the artist(s) of its time. Notably, the statuette's hollow pedestal, cast as one with the solid figure, is filled with greenish and brownish materials, with a yellowish metal foil sticking out, indicating a consecration deposit sealed by the filler (Figure 4.1b). Consecrating statues with the addition of such small objects is common in several regions, including the Himalayas and Indonesia [59, 60]. To gain deeper insights into the craftsmanship and cultural customs of the ancient society, as well as to assess the current state of corrosion in the artefact without causing damage, neutron tomography (NT) was performed to visualise the internal structure, followed by gamma spectroscopy (GS) to obtain elemental information for the entire object. The main aim of the iterative method presented in this chapter is to obtain quantitative information on the respective materials within the heritage object, through data fusion of the NT and GS experimental data.

Compared to X-rays, neutrons offer visibility of both light and heavy elements, even when the bronze is obscured by thick corrosion layers. Figure 4.1c and d show a NT slice of the Kuvera statuette and a segmentation highlighting different regions based on their grey tones. Despite a thin layer of superficial bronze corrosion (yellow segment), the statuette appears to be in good condition overall. The outer bronze "shell" (lavender purple) appears more solid than the inner bronze "core" (rose pink), which displays higher porosity, probably due to the casting process where the shell solidified first, forcing gases to move to the core (and outside). As anticipated, a folded foil (cyan) showing a high grey tone was discovered within the pedestal, mostly covered by filler material (white). Since the foil shows a notably higher grey tone compared to the main bronze, considering the associated ritual customs [61], it is reasonable to hypothesise that the foil is made of gold or silver (based on the neutron attenuation coefficients (cm^{-1}) of Au (6.23) > Ag (4.04) > Cu (1.07) > Sn (0.21) [62]). Even though it is possible to distinguish distinct bronze compositions (corrosion, shell, core) and the hidden foil, it is not possible to directly draw conclusions solely from NT to answer questions, such as which bronze composition was used for this statue, which corrosion products are associated with it, as well as which material was used for the foil offering in the pedestal. In heritage science, such information is usually obtained from XRF analysis, which has limited capability to quantify the elemental composition and probes only the outer micrometres of the object that may have undergone changes due to segregation during casting, degradation, alterations, or conservations during its lifetime. In this context, neutron-based elemental composition characterisation methods, such as instrumental neutron activation analysis (INAA), are ideally used to obtain the missing elemental information of the (pristine) inner materials.

Our method, similar to INAA, measures delayed radioactive decay through gamma spectroscopy, but the neutron activation is performed in an NT experiment. As discussed in the last chapter, corrections for self-attenuation effects of neutrons and gamma photons

activation radiation from neutron tomography reveals the hidden elemental composition of 3D art objects for free. *Scientific reports*, 14(1), 28982.

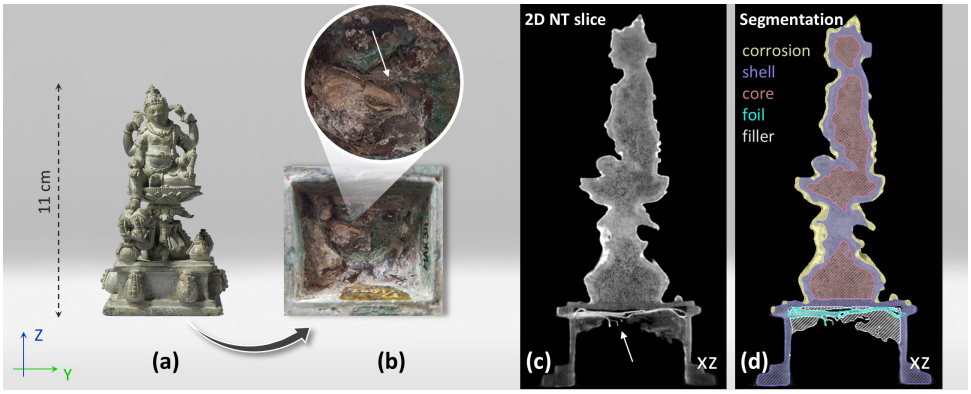

Figure 4.1: Neutron tomography of the Kuvera statuette. (a) Bronze representation of Kuvera or Jambhala, the god of prosperity in Hinduism and Buddhism. This statuette is in the Asian collection of the Rijksmuseum, Amsterdam (object number: AK-MAK-311, c. 850-930) [65]. (b) A bottom view of its pedestal where a small part of the foil sticks out (white arrow) of the filler material meant to seal this consecration deposit. (c) A vertical slice of the reconstructed NT model: the bulk bronze appears rather porous. Underneath the baseplate of the pedestal, a folded foil is visible with high brightness. Underneath the foil, an irregular filling material is visible that mostly covers the foil. (d) Segmentation of different regions according to the grey tones. The regions can be tentatively assigned to different material compositions.

are essential for accurate quantification. The mainstream approach of applying INAA to bulk objects involves determining factors for correcting these effects, either by theoretical modelling based on the Beer-Lambert law (e.g. 1D self-attenuation correction illustrated in Chapter 3), by Monte Carlo modelling assuming objects with simple geometry or homogeneity [26, 47], or by using a priori available composition information of a test portion sampled from the object [63, 64]. In the case of ancient cast bronzes, these calculations become tedious due to irregular shapes as well as internal inhomogeneities. Our method allows the incorporation of such complexities into the analysis through ray-tracing simulations. Moreover, NT provides an essential spatial resolution that is a lack in the traditional GS analysis, enabling the assignment of the identified elements to their specific source materials. A method, which quantitatively and non-invasively determines both structure and composition of the interior respective materials of an object, is of great value in heritage science.

While NT and GS solely provide spatial and elemental resolution, respectively, their datasets are quantitative, which in turn presents a unique opportunity to fuse structure and elemental information. For instance, if the foil (Figure 4.1b) is made of pure gold, its mass can be determined from the volumetric data of NT. Similarly, the mass can be obtained from the intensity of radioactive decay from gold through GS (if the attenuation effects are considered properly). If these two calculations yield the same mass of gold, it is a likely justification for the hypothesis; if not, the hypothesis can be revised until the two results align. Inspired by this concept, we designed an iterative approach (Figure 4.2) based on ray-tracing simulations to fuse NT and GS datasets, thereby localising the interior materials and quantifying their elemental compositions.

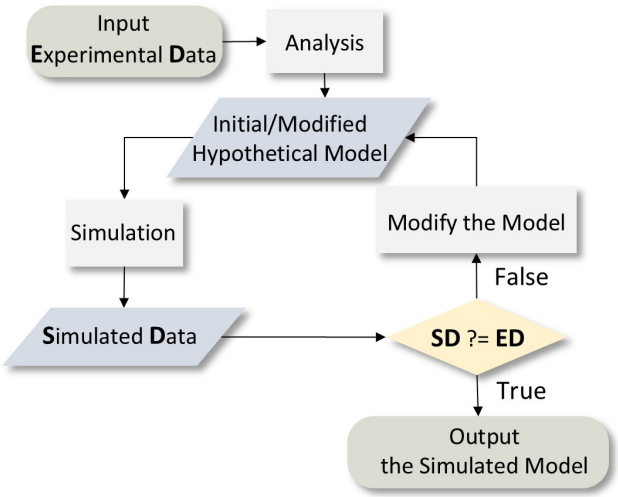

Figure 4.2: The iterative method. The process is divided into four steps: (1) analysing the experimental NT and GS data; (2) making a hypothetical model of material structure and composition for a simulation; (3) reproducing NT and GS data using Monte Carlo simulations; (4) comparing the simulated data with the experimental data. If the simulations match the experimental data, end the process; otherwise, repeat steps (2)-(4).

Our aim is to reproduce both NT and GS datasets using Monte Carlo ray-tracing simulations, where the attenuation correction effects of neutrons and gamma rays can be properly accounted for, regardless of the shape complexity. The core principle involves: (1) running multiple simulations with varied elemental composition assumptions, and (2) comparing the simulated data with experimental data to determine the composition that best matches the experimental data. Moreover, once the elemental composition is determined, our method can further predict how long an object remains radioactive, which is a common concern in cultural heritage research involving NT. In this chapter, we outline the method and demonstrate its precision by benchmarking the simulations using two objects with known compositions. Additionally, we showcase the potential of the method by applying it to the precious Kuvera statuette (Figure 4.1a).

4.2 Methods

To implement the data fusion algorithm described above, we first perform NT and (subsequent) GS on the object. These experimental datasets are then simulated through ray-tracing calculations of both experiments, using 3D models extracted from the NT reconstruction. The initial elemental composition assigned to the 3D model is based on the GS data. Subsequently, the composition is adjusted in an iterative process to reproduce both the gamma spectra as well as the neutron tomography projections.

4.2.1 Object Geometry from Neutron Tomography

The three-dimensional model (Figure 4.1c), reconstructed using Octopus software [30], represents both the atomic density as well as the neutron absorption and scattering cross-sections of local compositions. Utilising this data, materials with different grey tones can be segmented using Avizo software, as shown in Figure 4.1d. These segmented volumes are subsequently converted into surface models that define the geometries in the simulations.

4.2.2 The First Composition from Gamma Spectroscopy

The bulk composition, calculated based on the GS data using Equations 3.19 and 3.20, is an average over the entire object volume. According to this composition, along with the prior knowledge from techniques such as XRF and information about ritual customs, we are capable to make an initial composition assumption of each distinct material that segmented from the NT model.

4.2.3 Simulation of Experiments Using Monte Carlo Method

After assigning each segment of the object an initial elemental composition in the ray-tracing models, the particle beam as well as the interactions between particles and matter are simulated using Monte Carlo stochastics [66]. In practice, we utilised TOPAS MC [67] to perform Geant4-based Monte Carlo simulations [27]. The default "Shielding" physical model of particle-matter interactions was applied in the simulations. Due to the incomplete atomic de-excitation database within Geant4, a modification of the Geant4 databases was needed to produce gamma rays from metastable isotopes. For instance, gamma rays from Sn-125m were introduced by replacing the half-life and decay scheme of Sn-125 in the database (G4ENSDFSTATE and RadioactiveDecay, respectively) with those of Sn-125m. In fact, because the corresponding cross section affects both the gamma yield as well as the neutron attenuation in the simulation, this value was not modified, and we implemented the correct gamma yield in the simulations output, only.

In the simulations, the neutron beam was modelled as a parallel beam with Gaussian position distributions in both horizontal and vertical directions as illustrated in Figure 2.2. To simulate the accumulation effects of nuclei activation, the intensity of the neutron beam was modelled as multiple pulses, spread over the irradiation time. The neutron camera and gamma detector were modelled as surface scorers with dimensions matching those of the experimental neutron scintillator and the germanium crystal inside the gamma detector. These surface scorers record information about incident particles, including type, energy, arrival time, and arrival position, which could be converted into neutron projections or gamma spectra. Typically, one simulation of both datasets requires several hours on an 8-CPU workstation, depending strongly on the model complexity. By simulating approximately 100 million neutron trajectories through the object, the resulting neutron projections and gamma spectra can be compared with experimental data. Based on the differences between the simulated and experimental data, the composition of the segments in the model is adjusted to improve the match.

4.2.4 Comparing Simulations with Experiments

Comparison of Neutron Projections

Firstly, flat-field correction[68] needs to be applied to both the experimental and simulated projection pictures, and then the residual of their normalised pictures P is calculated pixel by pixel through:

$$\Delta P = \left| \frac{P_{\text{simu}} - P_{\text{expt}}}{P_{\text{expt}}} \right| \tag{4.1}$$

To individually assess the residual of each material segment l, the differences are further analysed by using its binary mask image M_l, the median of its residual is determined via:

$$\Delta P_l = \mathrm{MED}(\Delta P \cdot M_l) \tag{4.2}$$

Comparison of Radioactive Decays

The simulated gamma photon intensity I_{simu,E_k} needs to be corrected by considering the differences between the experiment and the simulation in terms of the number of impinging neutrons as well as the detector efficiency:

$$I'_{\mathrm{simu},E_k} = I_{\mathrm{simu},E_k} \cdot \frac{\Phi_{\mathrm{expt}}}{\Phi_{\mathrm{simu}}} \cdot \frac{\epsilon_{\mathrm{expt},E_k}}{\epsilon_{\mathrm{simu}}} \tag{4.3}$$

where Φ_{expt} and Φ_{simu} are the neutron fluxes in the experiment and simulations, respectively. ϵ_{simu} is the geometric efficiency of the simulated detector without gamma-energy resolution, while $\epsilon_{\mathrm{expt},E_k}$ represents the full-energy photopeak efficiency of the experimental detector for gamma energy E_k (refer to Section 2.3.3).

Then, the simulated gamma intensity can be compared to the experimental gamma intensity, without additional scaling factors, and their residual is defined as:

$$\Delta I_{E_k} = \left| \frac{I'_{\mathrm{simu},E_k}}{I_{\mathrm{expt},E_k}} - 1 \right| \tag{4.4}$$

where the quotient $\frac{I'_{\mathrm{simu},E_k}}{I_{\mathrm{expt},E_k}}$ is determined using Orthogonal Distance Regression (ODR) calculations implemented in the SciPy Python package[69].

Residuals-Based Iterative Procedure

The total residual Δ_{total}, combining residuals from neutron projections of L segmented materials as well as residuals from K gamma spectrum energy peaks, is determined by:

$$\Delta_{\mathrm{total}} = \sum_{l=1}^{L} \Delta P_l + \sum_{k=1}^{K} \Delta I_{E_k} \tag{4.5}$$

An ideal simulation would yield a residual of 0, implying that the closer the residual is to 0, the more likely the assumed composition in the simulation matches the actual composition. Following this principle, the elemental composition can be updated iteratively according to Δ_{total} calculated in the current (and previous) simulations, aiming to reduce Δ_{total} in the next comparison.

4.3 Materials and experiments

First, the validation of Geant4-based simulations is demonstrated by a set of six known objects contained within an aluminium cylinder (CYL) (Figure 4.3a), for which both the NT and GS experimental data are reproduced. Then, our method is demonstrated using a simple composition of a copper cube with three thin gold foils (CUBE) (Figure 4.3b). The iteration routine can determine the mass of the CUBE, solely from the gamma spectrum. Lastly, the method is applied to "data-fuse" the NT and GS experiments on the Kuvera bronze statuette, as shown in Figure 4.3c, where both the NT and GS components are shown simultaneously.

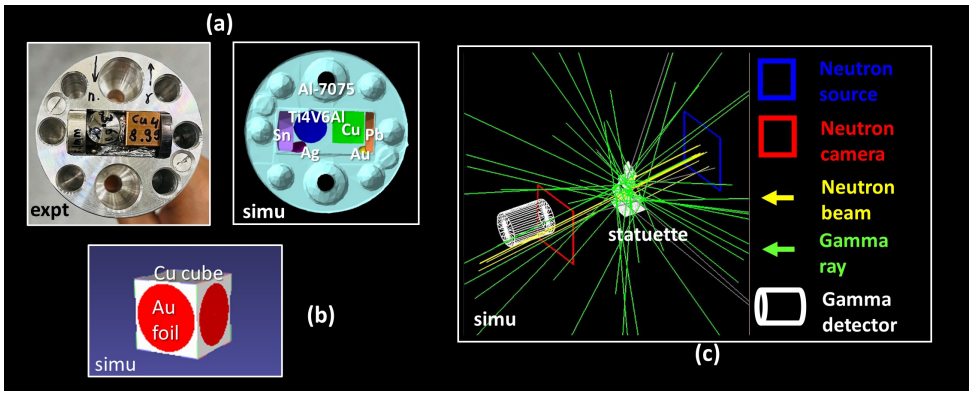

Figure 4.3: Objects used in the experiments: (a) Cylindrical object (CYL): top views of the CYL in the experiment (left) and simulation (right); (b) Cubic object (CUBE): CUBE model in the simulation; (c) Screenshot of the simulation of the NT and GS experiments on the Kuvera statuette (Figure 4.1)

4.3.1 CYL

The CYL is comprised of a large aluminium (Al-7075) cylinder, along with six small objects: a copper cube, a tin cylinder, a lead cylinder, a titanium alloy (Ti6Al4V) cylinder, a gold bead, and a silver nugget. To measure short half-life isotopes the object was first irradiated for 20 min in the neutron beam, thereby enabling a better signal-to-noise ratio in the GS detection. Then, NT on the CYL was done for 2.5 h, during which 501 projections from different orientations were collected. Subsequently, GS was performed to detect the long half-life isotopes. The model (the 3D geometries from the NT reconstruction, and their known composition) was then used in the simulations to reproduce NT and GS data. These simulated data were then compared with the experimental data to assess the accuracy and precision of the simulations in reproducing the experimental results.

4.3.2 CUBE

The demonstration of the iterative approach is done with a CUBE consists of a 1 cm^3 copper cube and three gold foils, each with a thickness of 0.05 mm. The foils were positioned individually against the side of the copper cube and wrapped together using aluminium foil. The CUBE was irradiated by neutrons for 2.5 h without rotation. Then, the radioactive decay was measured by GS, from which the masses of gold and copper were approximately determined. These initial mass estimates served as the starting point for subsequent iterative simulations aimed at optimising the masses to better match the actual masses. This optimisation process was implemented through TopasOpt [70].

4.3.3 Kuvera Statuette

The experiment procedure of the Kuvera, similar to the CYL experiment, involved an irradiation of 30 min followed GS measurements for short half-life isotopes. Then, NT was performed using 1500 orientations of the Kuvera in the beam, resulting in an irradiation of 23.5 h. Following this, GS was performed starting approximately 30 min after the NT and

lasting for 3 days.

The NT model was segmented into the bronze (consisting of corrosion, shell, and core), the foil, and the filler (Figure 4.1d) based on their grey tones. To assign an initial composition to each of these 5 segments, the masses per element were estimated from the GS data, using (initial, coarse) self-attenuation corrections (see analysis details in Section 3.4.3). These masses were then assigned to the segments (core and shell: {Cu, Sn, As, Sb, Co, Mn}, corrosion: {H, Na, Cl, Cu, Sn, As, Sb, Co, Mn}, foil: {Au, Ag}, filler: {Sn, Cu}).

The first approximation is that elements As, Sb, Co and Mn (with concentrations less than 1 wt%) hardly contribute to the neutron attenuation, while H (present only in corrosion layer) has a very strong contribution. Moreover, H, Na, and Cl are assumed to be associated with the corrosion layer only, while the other trace elements are assumed to be evenly distributed over the bronze. According to the ancient Indonesian tradition [60] and our NT analysis (as illustrated in Figure A.2), tin and bronze were used in the filler segment, which we confirmed with XRF measurements (Table A.2). XRF also provides an approximate Sn/Cu ratio of the corrosion layer. These segments, with their corresponding composition, were used as an initial hypothetical model for use in an iterative optimisation procedure of composition determination. For practical reasons, we demonstrate this procedure for a range of compositions that were 'manually' set, rather than determined by an iteration routine.

The segments "wrap" each other: the core is enveloped by the shell, which is covered by the corrosion layer. Matching the simulation projections to the experimental data will imply that any composition changes in one segment will affect the analysis of the other two. To circumvent this effect, the optimisation workflow was designed in a specific analysis order from outer segment to inner segment, progressing from the corrosion layer to the shell and finally to the core. Once the composition of the outer segment is determined, it is fixed to determine the composition of neighbouring inner segment(s).

Since the grey value of the corrosion layer is dominated by H, firstly, the ratio of H to (Sn/Cu) of the simulation is matched using the experimental projections. With this corrosion composition fixed, the Sn/Cu ratio of the shell is matched likewise. Lastly, this procedure is repeated for the core, filler and the foil. When comparing the simulated GS using these compositions to the experimental spectra, it turns out that the Sn and Cu GS signals are slightly less than the experimental data (with a mismatch of 31% and 10%, respectively). The most obvious modification to then make is the Sn/Cu ratio of the corrosion layer (which was inferred from XRF). This order, comparing NT projections from outside to inside and then comparing GS, allows to determine a self-consistent set of compositions after a few iterations. With the bronze compositions fixed, finally, the Sn/Cu composition of filler and the Au/Ag composition of the foil are determined.

4.4 Results and discussion

4.4.1 Method validation

Simulation

Figure 4.4 shows the agreement in the gamma spectroscopy between the simulation and the experiment for the known objects (CYL), achieved without the need for scaling or calibration. For all the studied isotopes, the gamma intensity was simulated to be of

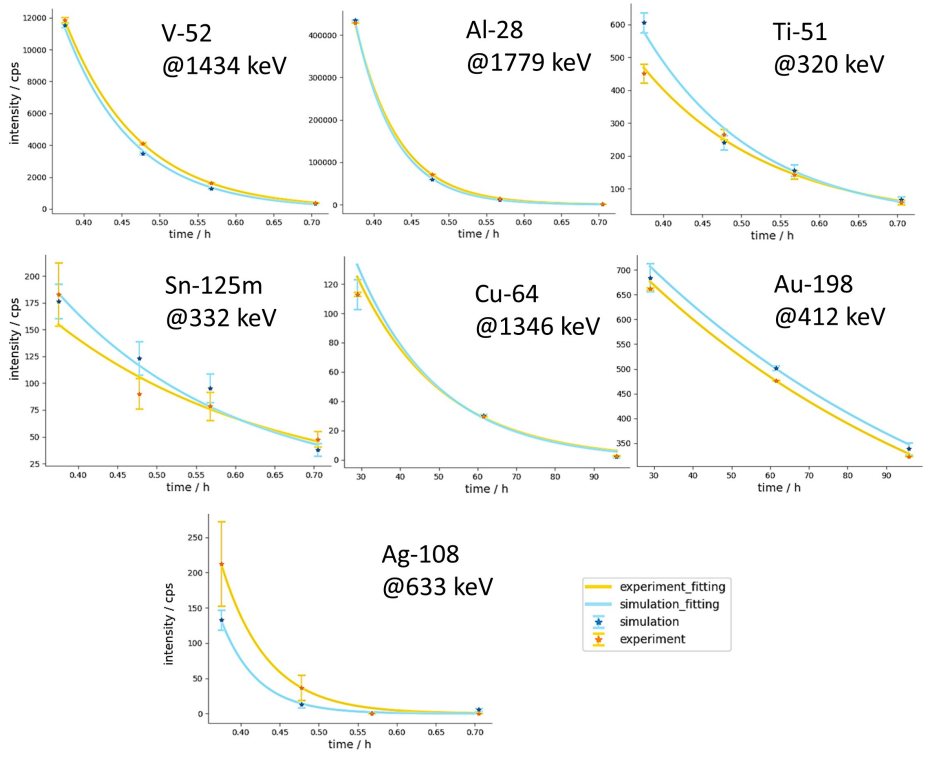

Figure 4.4: Correspondence of the time-dependent simulated and experimental gamma intensity for the different isotopes of the CYL. Notably, all these simulated gamma intensities contain no scaling factor.

the same order of magnitude as that observed in the experiment, and it decayed with a similar rate as that in the experiment. The most noticeable deviations are that of the Ti-51 and Ag-108, two short half-life components. Their intensities were affected by the much stronger Al-28 decay and the spectral background generated by this (230 g) cylinder. In Figure A.3, we demonstrated the improved correspondence when the aluminium cylinder is absent during the irradiation. Although the agreement is not perfect, the comparison indicates that the gamma spectroscopy data can be quantitative predicted by simulation of the experiments (NT irradiation and GS). Additionally, the simulations based on the Geant4 databases are capable to predict the gamma intensities effectively.

Since the GS method lacks spatial resolution, the GS result reports the per-isotope intensity integrated over the entire cylinder. As a result, the measured copper signal includes contributions from both the Cu cube and the Al-7075 cylinder, making the Cu mass quantification as a whole, rather than independently. However, by applying material masks in the analysis of the NT projections, the neutron attenuation effect of each material can be observed and quantified independently (Figure 4.5). We exploit this for Pb, which is not detected by GS but exhibits a clear signature in the NT projections, as shown in Figure 4.5a and b. The residuals of NT projections were quantified per pixel, as shown

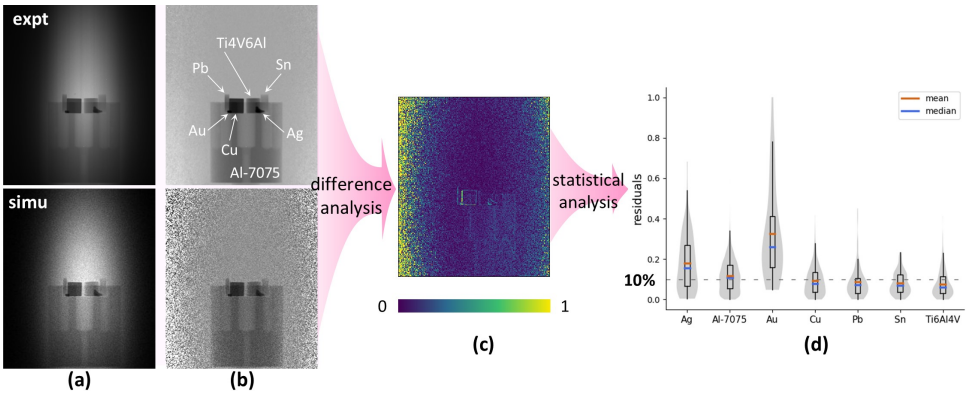

Figure 4.5: Comparison of simulated and experimental NT data for the CYL experiment. (a) Experimental and simulated NT projections at the same orientation of the CYL in the beam. (b) Normalised experimental and simulated projections for comparison. (c) Residual of the comparison, determined through Eq. (2). A perfect agreement would result in all pixels being dark blue. (d) Statistics results of NT pixel residuals for each material segment. The distribution of data points is shown in grey.

in Figure 4.5c, with most disagreements observed at the rim of the figure and the rim of objects. Further statistical analysis of the NT residuals per material segment is presented in Figure 4.5d. Notable data outliers, mainly caused by simulated particles with 30 times lower intensity than those in the experiment, increased the residual uncertainty. Nonetheless, the median values remained representative of the pixel residuals across the entire material area. Especially small or transparent objects can pose challenges in obtaining accurate segmentation, thereby limiting the accuracy of our method. For instance, the segmented dimensions of the tiny Au bead, Ag nugget, and the (transparent) Al cylinder were respectively +26%, +15%, and -10% off from their physical dimensions, resulting in their relatively larger residuals of 33%, 18%, and 12%, respectively. Despite these discrepancies, good correspondence between the simulated model and the actual object was achieved, with the median of the residuals for other elements is below 10%.

Combining the results from GS and NT provides a more comprehensive understanding of the discrepancies arising from each element within each material of the CYL (see details in Table A.3). Ag and Au, with the smallest weight and volume, exhibited the largest total residual of 60% and 38%, respectively. This indicates relatively high simulation uncertainty associated with the analysis of elements present in smaller quantities. For the remaining elements, the simulated data closely matched the experimental data, suggesting that the complexities of the interactions between objects and particles were effectively accounted for in the simulations. While certain factors, such as neutron beam divergence and detector efficiency, were not fully incorporated into the simulations, leading to slightly less accurate simulated results, a good overall agreement with the experimental data (overall difference $\leq$ 20%, except Ti, which is 23%) was achieved. Future work will involve modelling more realistic neutron beam and detector systems to enhance the accuracy of the simulations.

Table 4.1: Comparison of measured and calculated masses before and after 50 iterations in the CUBE analysis.

Material	Weighed [g]	Initial calc. [g]	Rel. error [%]	Final calc. [g]	Rel. error [%]
Cu cube	9.06	10.59	17	8.33	8
Au foils	0.19	0.24	27	0.19	0

Note: "Initial calc." and "Final calc." refer to masses calculated before and after 50 iterative corrections. Relative error is calculated against the weighed value.

Iteration

The experiment with the cube (CUBE) aimed to validate the iterative approach. Table 4.1 demonstrates a significant improvement in mass calculation accuracy after performing 50 iterations, compared to the mass initially calculated by GS. This outcome confirms the feasibility of achieving accurate mass composition quantification using iterations with Monte Carlo simulations. Although this experiment is based only on GS data, coupled with the findings from the CYL experiment, we believe that the addition of the "simu-expt" comparison of the NT projections will further improve the composition quantification through imposing an extra constraint. For heritage science, where the composition is not known, this methods allows to determine the composition, based on minimization of the differences between simulation and experiment.

4.4.2 Analysis of the Kuvera Statuette

As shown in Figure 4.1, the solid bronze consists of three regions, of which the corrosion layer was absent when the statue was cast. The analysis of the 3D NT model suggests that this solid bronze statuette was made via the lost-wax casting technique, as shown in Figure 4.6a. During casting, the clay mould was positioned upside down, and the molten bronze was poured into the mould through a system of pouring channels and vents, of which we can see remnants at the bottom of the pedestal walls. This process, combined with the slow cooling of the liquid bronze, led to the segregation of the bronze into the distinct (solid) shell and (porous) core region. It is apparent that the core is particularly porous, and our new data fusion algorithm allows to quantify that the composition of this region is different from that of the shell region, as shown in Figure 4.6b (see detailed simulation procedure and results in Figure A.4). The shell bronze (5 wt% Sn) solidified first, expelling some of the tin towards the core (15 wt% Sn) and possibly the outer surface. Based on the assumption of homogeneity of molten bronze, we infer that the original bronze material prepared by the artist contained 85-95 wt% Cu and 5-15 wt% Sn, characteristic of low-tin bronze statuettes.

The corrosion analysis revealed a significant association with hydrogen, chlorine, and sodium. Despite hydrogen being undetected by GS, its notable neutron attenuating effects were measured by neutron projection, suggesting a certain amount of hydrogen presence within the corrosion layer (see Figure A.4). Additionally, chlorine and sodium were identified in the corrosion layer, indicating the presence of potential corrosion products such as copper chlorides and chalconatronite [71]. These three corrosion-associated elements were present in moderate amounts, implying that only a small amount of material was corroded. This observation aligns well with the analytical results from NT slices and visual

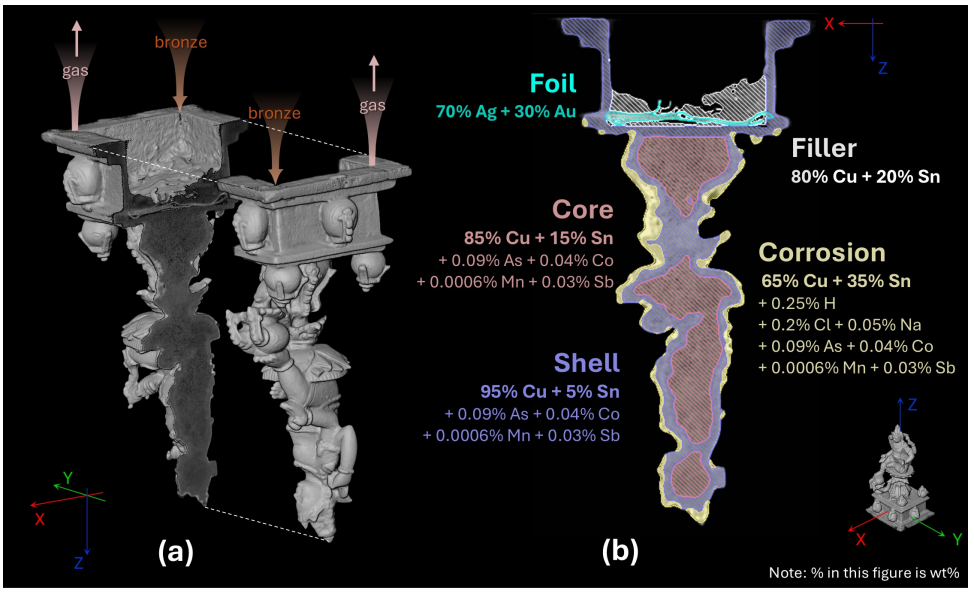

Figure 4.6: (a) Possible casting process of the Kuvera statuette. (b) The quantified elemental composition of each material segment of this statuette. See Table A.4 for the summary of the analytical elemental masses.

inspections. By comparing the composition of the corrosion bronze (65 wt% Cu) with that of the pristine bronze in the core and the shell (approximately 90 wt% Cu), we tentatively conclude that the corrosion layer has undergone decuprification, which may have occurred during burial.

Contrary to our initial hypothesis that the foil was pure gold, based on its yellowish appearance, our results surprisingly indicate that the foil comprises primarily silver (70 wt%) with a small amount of gold (30 wt%). This finding could reflect an intentional choice of alloy, perhaps to economize on gold for making a silver-gilt foil, or it might have been an unintended result of recycling precious metals. For the filler material, although its composition was initially identified as an alloy of Cu and Sn, further structural analysis (Figure A.2) suggests that it is more likely a mixture of low-tin bronze foil(s) and pure tin. The bronze foil(s) could have been used as a support to fix the deposit during tin casting and/or as a spacer to prevent the deposit from getting contamination of the solder material (Sn), or they might have served other unknown ritual purposes.

4.5 Conclusion

We established a non-destructive method to quantify both the internal elemental composition and structure of bulk objects using only a single neutron tomography experiment. Specifically, this method involves performing delayed-gamma spectroscopy after neutron tomography to gain composition information "for free" and utilizing ray-tracing simulations to quantitatively fuse these NT and GS datasets in an iterative procedure. Even if the object consists of distinct materials rather than one homogeneous alloy, our method

allows to assign a plausible composition of each part.

This method has been validated in two ways, utilizing objects of known composition. The simulation procedure can reproduce both the neutron projections as well as the gamma intensity with a total residual of less than 20%. Since it is based on segmentation of the NT-reconstructed 3D model, the method is limited by the spatial resolution of the NT experiment. Likewise, the analysis of the GS data is limited by the beam flux and the signal-to-noise ratio can be diminished by the Compton background of the different elements in the object, as we demonstrate in determining silver from the Ag-108 signal, hindered by the Al-28 background. By assigning specific elements to sub-volumes, an iterative process can determine the masses of these sub-volumes with an uncertainty of less than 10%. This method was then successfully applied to a bronze Kuvera statuette—a complex analytical case with corrosion, phase segregation, and a consecration deposit. Our method allowed to quantify the interior elemental composition of this statuette from a single NT experiment, providing potential insights into the (technical) skills, technological and material choices of local craftsmen, as well as the ritual customs of ancient societies.

Despite not achieving perfect correspondence to the experimental datasets and being constrained by limited computational power, this work represents a pioneering step forward in multimodal neutron techniques, expanding the applications of both neutron tomography and gamma spectroscopy, through data fusion of these two modalities. In addition, our approach only requires a single HPGe detector and an 8-core CPU to add the extra "element-dimension" to the 3D model of the neutron tomography and is therefore widely applicable. Materials science of heritage objects is notoriously challenging because of the heterogeneity of the pristine object as well as its centuries-long (un-) intentional modifications. The ability to non-destructively obtain quantitative structural and compositional information on the hidden (pristine) bulk material of these objects is a great asset for heritage science. We believe that our method offers such value and can be further applied in other cultural heritage research involving objects such as Chinese bi-metallic bronze swords [72], Van Leeuwenhoek's microscope[73], and glasses with multiple colours [74]. We demonstrate that this data fusion method provides new capabilities for beamlines with a neutron flux of $\sim 7 \times 10^6$ n/cm^2/s, with sufficient sensitivity. Furthermore, we expect it can be combined with other characterisation techniques, such as X-ray CT [75], epithermal neutron radiography [76], and cold neutron radiography/tomography [77], to broaden its application and to gain more comprehensive insights into the studied object. Finally, for context within this thesis, we compare the accuracy and efficiency of the present iterative Geant4 method with the "matchbox" approach (Chapter 3)—as well as with the GPU-based framework introduced next—in Chapter 5.

5

New GPU-based Simulation Framework to Accelerate Data Fusion

Iteratively testing composition models in simulation has proven effective for quantitatively fusing neutron tomography and subsequent delayed gamma spectroscopy datasets, offering valuable insights into the interior elemental composition of bulk artefacts. This is an aspect of unique importance in cultural heritage research, but its practical application is significantly limited by the computational demands of CPU-based simulations. Since GPU-based graphics rendering shares underlying physical similarities with the tracing of photons, neutrons, and gammas, we were inspired to develop a novel GPU-accelerated simulation framework used as the computational core of the data-fusion method. The framework integrates neutron transport and time-resolved neutron activation into a single, unified ray-tracing pipeline, enabling large-scale NT-GS simulations to be performed with high efficiency and physical realism. Compared to the Geant4-based simulation on an 8-core CPU, the runtime on a consumer-grade NVIDIA GeForce RTX 3070 was reduced from 50 days to just 5 minutes for a simulation involving ten billion neutrons. This substantial speed-up reduced the overall analysis time from weeks to hours in the application to the Ommerschans sword, demonstrating how GPU acceleration makes simulation-based NT-GS data fusion both practical and scalable for real-world archaeological investigations.

This chapter is based on an ongoing collaborative project with Jordan Ingram and Ilia Meijer, to be published in the near future.

5.1 Introduction

In cultural heritage research, it is increasingly common to employ a variety of non-invasive techniques for probing materials and obtaining complementary insights. Despite the extensive information these techniques provide, it remains difficult to draw definitive conclusions from individual datasets. Consequently, data fusion stands out as an essential procedure for integrating disparate datasets into one, more informative model that offers a more comprehensive view. However, this process is often complicated by differences in data formats and representations. In this respect, neutron tomography (NT) and gamma spectroscopy (GS) are particularly well suited for data fusion. Both non-invasive techniques can provide quantitative bulk information and, crucially, probe the same entire volume of the object, thereby avoiding the mismatch that arises when combining, for example, XRF (surface-sensitive) with CT (bulk-sensitive). NT and GS provide fundamentally different but complementary information: NT yields 3D geometry and internal structural features, while GS reveals elemental composition. In our previous work, presented in Chapter 4, we proposed a feasible simulation-based approach to fuse NT and GS datasets, assigning elemental compositions back to the source materials and thus providing new insight into quantitative interior mass composition that is difficult to achieve with any single technique.

While this data-fusion approach has proven effective and has been successfully applied to bronze research, its core operation—searching for the optimal composition assignment by iteratively running simulations and comparing them with experimental datasets—can be extremely time-consuming. In our previous work, individual simulations involved tracing at least millions of rays and often required several hours to complete using Geant4 [27] on an 8-core CPU. Geant4 is one of the most widely used ray-tracing tools in the neutron community, but its speed is strongly constrained by CPU-based processing, with rays handled sequentially. Although CPUs can achieve some parallelism through multithreading, the efficiency remains limited compared to GPUs. As a result, the number of composition assumptions that could realistically be tested was limited, restricting the scope of the search for the best match. This limitation becomes especially critical in complex experiments involving multiple irradiations and radioactivity measurements, such as the neutron investigation with the Ommerschans sword (see Figure 5.1). Modern GPUs provide a practical solution to this computational bottleneck. Unlike CPUs, which trace particles one at a time, GPUs can execute millions or even billions of independent particles in parallel. By shifting the ray-tracing simulations from Geant4 to a GPU-based implementation, we retain the iterative workflow for data fusion but significantly increase its efficiency, making it possible to explore a far broader range of composition assumptions within the available analysis time and thereby strengthen the robustness of the results.

GPUs have already been widely used in ray-tracing applications such as optical rendering [78–80] and in particle transport simulations for neutrons or photons [81–86]. However, no existing GPU-based simulation framework is capable of treating neutron transport and subsequent neutron activation with gamma transport within a single pipeline, which is essential for combining NT and GS in a quantitative manner. This motivated our development of a GPU-accelerated program for NT-GS simulations, but developing such a tool entirely from scratch would require considerable expertise in both programming and particle physics. Therefore, rather than starting from zero, it is more practical to adapt and extend an existing open-source GPU framework, enabling efficient, flexible NT-GS

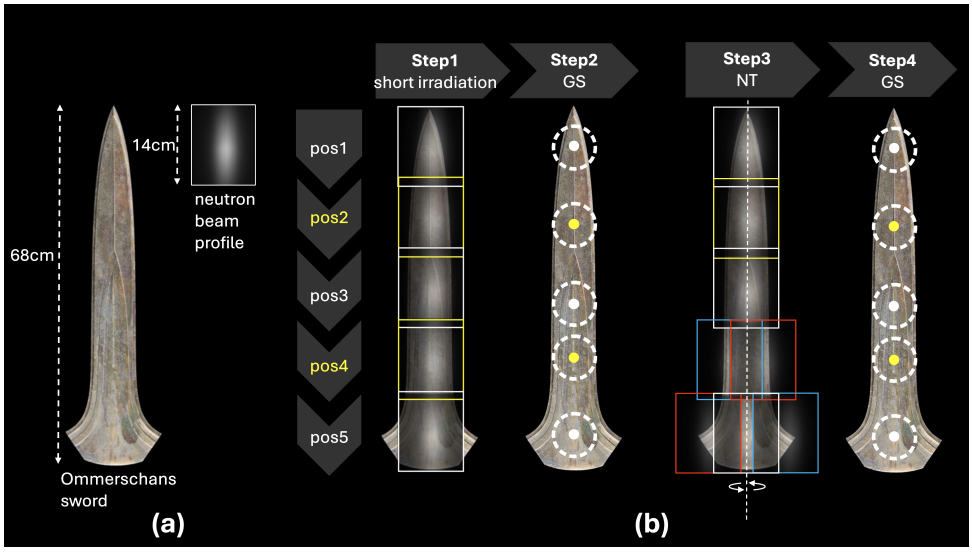

Figure 5.1: Neutron experiments on the Ommerschans sword to investigate its interior structure and composition. (a) The sword is currently housed in the *Rijksmuseum van Oudheden* (object number: ROM *inv.* no. d 2017/7.1). Compared to the neutron beam cross-section, the sword is much larger, requiring multiple neutron irradiations and scans to fully cover the sword. (b) The experiment has two stages, comprising four steps in total. Stage 1: five short irradiations along the sword's height to detect short half-life isotopes; gamma spectroscopy was performed after each irradiation. Stage 2: neutron tomography (long irradiation) was performed at the five height positions for reconstructing 3D structure and detecting long half-life isotopes; sideways scans were also performed on the wide regions; gamma spectroscopy was conducted after each height-position scan.

simulations with substantially reduced development effort.

In this work, we leverage Vulkan Ray Tracing [79] as the framework for simulating NT and subsequent GS experiments. Originally developed for real-time photorealistic rendering in applications such as video games [87] and movies [88], Vulkan Ray Tracing provides a highly parallel and extensible pipeline for GPU-based ray-tracing. Its design makes it particularly well suited for particle transport simulations for two main reasons: first, tracing visible light shares fundamental physical similarities with tracing neutrons or gamma photons, as both involve modelling particle trajectories and their interactions with matter; and second, two of the most computationally intensive tasks, namely particle-geometry intersection calculations and CPU–GPU data transfer, are already optimised through built-in acceleration structures and advanced memory management. This preserves both computational efficiency and precision in simulating neutron and gamma transport. In addition, the default image-rendering function can be conveniently repurposed to produce simulated neutron projections (NT data), while its frame-based rendering can be exploited to represent time evolution, thereby allowing simulation of the accumulation and decay of gamma emissions (GS data) over time by using successive frames, analogous to neutron pulses in a neutron irradiation experiment. Building on these features, we construct a GPU-accelerated framework for simulating NT and GS experiments, which ultimately supports efficient and reliable NT-GS data fusion. In the context of cultural heritage

research, such a tool is particularly valuable, as NT and GS are increasingly combined for non-invasive investigations of objects' interior structures and compositions, and this new GPU-accelerated framework provides an efficient and accessible way to easily perform the complex particle simulations required to quantitatively fuse the two datasets.

This work is an advancement of the data-fusion method proposed in Chapter 4, following the same principle but with a focus on accelerating the simulation and overall analysis processes using GPUs. The primary objective is to transform a reference example of Vulkan Ray Tracing into a specialized GPU-based framework for simulating NT and subsequent GS experiments. This includes incorporating neutron- and gamma-specific physical processes into the ray-tracing pipeline and adapting the default rendering pipeline to encode NT and GS outputs. In this chapter, we detail the construction of this adapted framework and validate its ability to reproduce neutron projections and gamma spectra through a benchmark experiment with a known composition object. We also showcase its application to the Ommerschans sword to quantify the composition of its tip region and compare the results with those obtained from the GS-based method (Method 1 in Chapter 3) and from the Geant4-based NT-GS data-fusion method (Method 2 in Chapter 4), thereby assessing the consistency and demonstrating the practical advantage of the GPU-accelerated simulation framework.

5.2 Implementing NT-GS Simulations via Vulkan Ray Tracing

5.2.1 Ray-tracing Pipeline and Shader-Based GPU Execution

The NT-GS simulation is implemented using a predefined example of Vulkan Ray Tracing [89]. Figure 5.2 shows the virtual simulation world, replicating the experimental setup and the particle behaviours relevant to NT and GS experiments. In the implementation, particle behaviours are modelled using small programs called *shaders*, which are chained together in the ray-tracing *pipeline* that guides the GPU to execute the simulation.

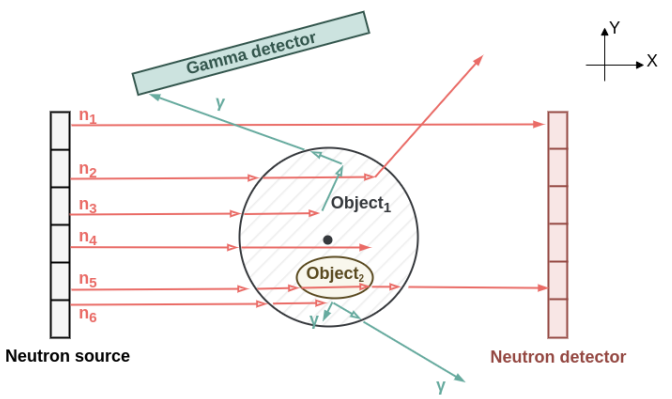

Figure 5.2: Schematic of the simulation scene for NT and GS experiments (top view). The object is placed at the centre. The neutron source and detector rotate around the object to mimic neutron scans, while the gamma detector remains fixed to represent delayed gamma measurements. Neutrons may transmit, scatter, or be absorbed with or without gamma emission, whereas gamma photons either transmit or are absorbed (with all photon interactions treated as absorption in this simulation).

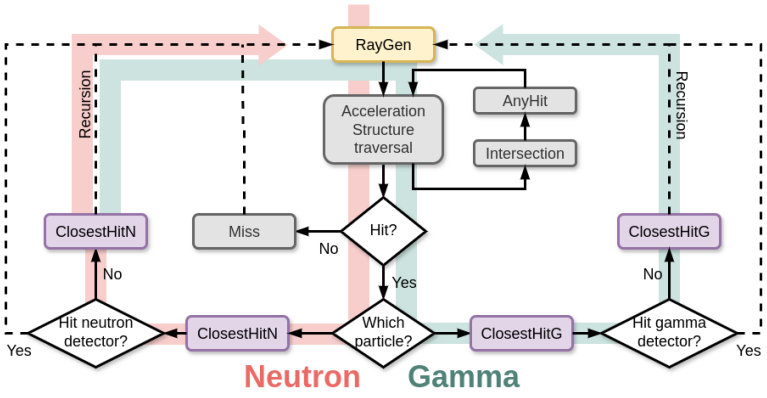

Figure 5.3: Ray-tracing pipeline for neutron transport and neutron activation with gamma transport. The process branches into two recursive paths: (1) the neutron path (rose), where neutrons are emitted (RayGen), traced to the closest hit (Intersection and AnyHit), or exit the scene (Miss); at the closest hit, they may transmit, scatter, be absorbed, or be detected (ClosestHitN); and (2) the gamma path (mint green), triggered when neutron absorption induces gamma emission. Gamma rays are generated (RayGen) and then traced through the same intersection tests (Intersection and AnyHit) until they exit the scene (Miss); if a closest hit is found, they may transmit, be absorbed, or reach the detector (ClosestHitG). Custom shaders (ClosestHitN and ClosestHitG) implement neutron and gamma physics, while built-in shaders (Intersection and AnyHit) handle geometry traversal. The transition from the neutron path to the gamma path is determined in the ClosestHitN shader.

The simulated setup includes a neutron source, the object(s) under investigation, a neutron detector, and a gamma detector. The pipeline, shown in Figure 5.3, begins with the RayGen shader, where neutrons are emitted as parallel beams from the source. This emission is represented by rays launched from a virtual camera plane of pixels (an abstraction inherited from graphics rendering[1]). Each pixel generates one neutron with a fixed parallel direction, while its position and energy are sampled from reference distributions.

Each neutron is then traced through the scene to its nearest intersection with the object's surface (the *closest hit*). At this stage, the ClosestHitN shader evaluates whether the neutron actually reaches the intersection without interaction, or whether it interacts beforehand, leading to scattering or absorption. Transmission and scattering events both generate a new neutron, while absorption may trigger the emission of one or more gamma photons. Secondary particles are launched from the RayGen shader with updated position, direction, energy, and particle-type information. If multiple gamma photons are produced, they are emitted and traced sequentially. Similar to neutrons, gamma photons are traced to their closest hit, but their interactions are processed by the ClosestHitG shader, where all non-transmission interactions are treated as absorption events.

Tracing terminates under different conditions depending on the particle type. For neutrons, it ends if the particle exits the scene, reaches the detector, or is absorbed without gamma emission. For gamma photons, tracing continues until all photons in the cascade have been absorbed, exited, or reached the detector. Detector signals are then collected in

[1]In Vulkan and similar GPU ray-tracing frameworks, rays are typically generated from a virtual camera plane for optical rendering efficiency. Here, this mechanism is repurposed both to initialise neutron beams and to record NT and GS outputs.

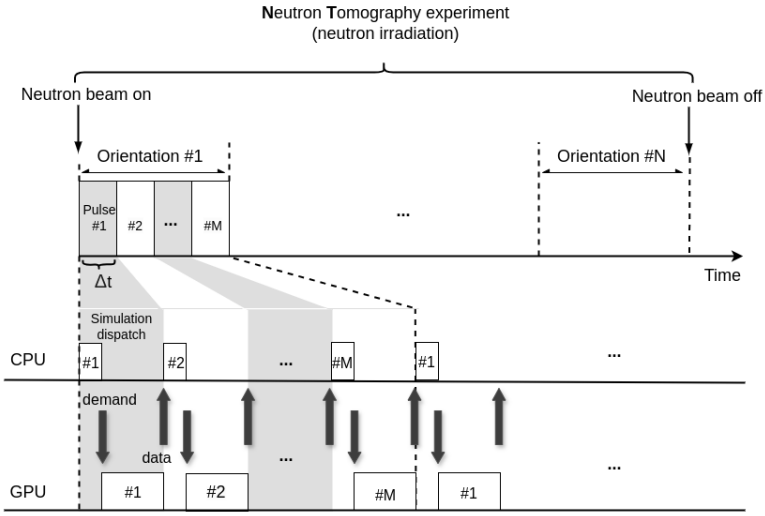

Figure 5.4: CPU and GPU collaboration in NT-GS simulations. Neutron scans are modelled as multiple irradiations at different angles. For each orientation, the CPU submits multiple neutron-pulse dispatches (at different time) sequentially to the GPU, simulating radioactivity build-up from neutron activation. The GPU handles each dispatch by emitting and tracing neutrons in parallel. The simulated neutron and gamma data are returned to the CPU for data aggregation. Gamma data from each dispatch update the spectra using the same acquisition times as in the experiment, while neutron data from the same orientation are merged to generate the corresponding projection.

RayGen and stored as either neutron hit positions or gamma energies with delayed times. Shaders exchange information via the *ray payload*, which carries particle-specific data and ensures consistency across the different shaders of the pipeline.

The entire simulation operates through close collaboration between CPU and GPU, as shown in Figure 5.4. Conceptually, the CPU acts as the "manager", scheduling simulation dispatches (neutron pulses) and aggregating the simulated results, while the GPU functions as the "worker", running each dispatch through the ray-tracing pipeline and transferring back the simulated data to the CPU. Once all dispatches are complete, the data is aggregated to form the simulated NT and GS datasets, which are ready for comparison with experimental data in the data-fusion workflow.

5.2.2 Integrating Stochastic Physical Processes into Ray-Tracing Shaders

To realistically and quantitatively simulate neutron and gamma transport, as well as neutron-to-gamma transition, the model must account for the probabilistic nature of particle behaviour in NT and GS experiments. This is achieved by integrating stochastic physical processes into the ray-tracing pipeline, specifically within the RayGen, ClosestHitN, and ClosestHitG shaders (Figure 5.5). A Monte Carlo approach is used to sample both the initial properties of particles and their subsequent interactions with matter.

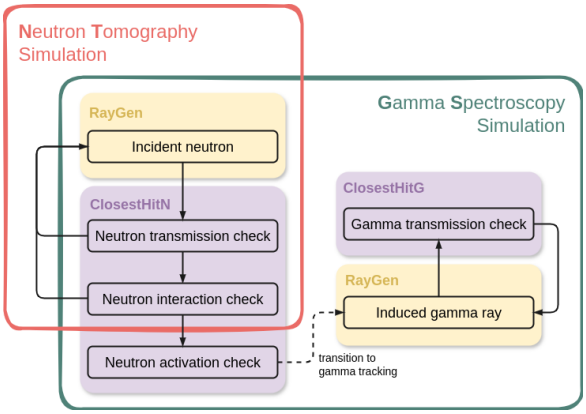

Figure 5.5: Overview of the essential shader logic and the associated physical processes in the ray-tracing pipeline of the NT-GS simulation.

For neutrons, the process begins at initialisation, where energy and position are sampled from the reference spectrum and spatial distribution. After emission, each neutron is tested for transmission through the medium to its closest-hit intersection (neutron transmission check). If transmission fails, an interaction is assumed and classified as either scattering or absorption (neutron interaction check). In the case of absorption, the simulation also evaluates whether activation occurs; if so, one or more gamma photons are generated, with their emission energies and times explicitly determined at this stage (neutron activation check).

For gamma photons, the procedure is similar but simplified. Once emitted, each photon is tested for transmission through the medium (gamma transmission check). If transmission fails, the photon is classified as absorbed, with no further distinction between photoelectric absorption, Compton scattering, or pair production. This simplification is based on an assumption that only full-energy gamma photons contribute to the corresponding peaks in the experimental GS data.

Monte Carlo Method

The stochastic modelling in this simulation is based on the Monte Carlo method [66], which enables sampling of physical quantities according to their known probability distributions, thereby representing the inherent randomness of the physical processes of NT and GS experiments. The procedure involves two essential steps.

Step 1: constructing a cumulative distribution function (CDF) from the underlying normalised probability distribution.

For discrete quantities with probability mass function (PMF) p_i, the cumulative distribution is:

$$P_i = \sum_{j=1}^{i} p_j \tag{5.1}$$

For continuous quantities with probability density function (PDF) $p(x)$, the cumulative distribution is:

$$P(x) = \int_{-\infty}^{x} p(t)dt \tag{5.2}$$

Step 2: generating a uniform random number r in the interval $[0,1)$ and using it to sample from the CDF.

For the discrete case:

$$\text{Find } i \text{ such that } P_{i-1} \leq r < P_i \tag{5.3}$$

For the continuous case:

$$x = P^{-1}(r) \tag{5.4}$$

Random numbers are generated from seed values that vary with each dispatch, emission pixel, and particle type, ensuring statistical independence across samples.

Approximation of Large Tabulated Cross-Section Data

The key datasets used in this simulation are neutron and gamma cross-sections, which are frequently queried for sampling in the particle transmission and interaction checks. Their values are tabulated over a wide energy range: neutron data by isotope and gamma data by element. These datasets are therefore large and highly detailed, which makes them impractical for direct use in shaders because of the limited GPU memory and the computational overhead of repeated lookups. To address this, the tabulated data are approximated with parametric models. This approach allows each isotope- or element-specific cross-section dataset to be represented by a small set of parameters, which significantly reduces storage requirements while still preserving the precision of the original data.

Neutron Cross Section The attenuation of thermal neutrons is dominated by scattering and absorption. Within the thermal range of 0.01-0.13 eV relevant to the experiments, the total scattering cross section remains nearly constant (e.g. for Cu-63, the variation is of only about 2% across the thermal range), whereas the absorption cross section is strongly energy dependent. Accordingly, the scattering cross section is treated as a constant for each isotope, while the absorption cross section is approximated using its inverse relationship with neutron velocity, following the 1/v law:

$$\sigma_{\text{abs}}(E) \propto \frac{1}{v} \tag{5.5}$$

Given the relationship between energy and velocity:

$$v = \sqrt{\frac{2E}{m}} \tag{5.6}$$

the absorption cross section becomes:

$$\sigma_{\text{abs}}(E) = \frac{k}{\sqrt{E}} \tag{5.7}$$

where k is a fitted scaling parameter based on the data from the ENDF database [90]. The total cross section is then given by

$$\sigma_{\text{tot}} = \sigma_{\text{abs}} + \sigma_{\text{scatt}} \tag{5.8}$$

Gamma Cross Section For gamma photons, the energy range of 100-4000 keV is considered, aligning with the GS experimental setup. The cross sections in this range are approximated by fitting elemental cross-section data from the ENDF database [90] with a second-degree polynomial in log-log space:

$$\ln(\sigma_{\text{tot}}(E)) = a + b\ln(E) + c[\ln(E)]^2 \tag{5.9}$$

where a, b, and c are fitting parameters stored for each element.

Neutron Initialisation

The initialisation of neutrons is performed in the RayGen shader, where each emitted neutron is assigned an energy, a position, and a fixed parallel emission direction. Both the energy and spatial distributions are sampled from experimentally measured reference data to reproduce a realistic neutron beam.

For neutron energy, the experimentally measured energy spectrum is first converted into a CDF via Equation 5.1. Sampling then proceeds using the inverse transform method (Equation 5.3), ensuring that the simulated neutron energies statistically follow the reference spectrum [35].

For spatial distribution, the reference open-beam image provides a two-dimensional flux profile across the source plane (Figure 2.2). Both the horizontal and vertical intensity profiles are approximated with Gaussian functions, whose parameters are used for sampling the neutron emission position in 2D and reproducing the experimental beam profile.

Particle Transmission Check: Flight Length vs Penetration Depth

When neutrons or gamma photons encounter an object along their trajectory (the closest hit), the simulation must verify whether the detected geometric intersection is physically valid. Intersection detection alone does not account for possible interactions with the medium that may occur before the particle reaches the hit point. To evaluate whether the neutron actually reaches the intersection without interaction, the simulation compares two quantities: (1) the geometric flight length L, i.e., the distance from the particle's origin to the closest hit, determined by the AnyHit and Intersection shaders; (2) the penetration depth d i.e., the distance a particle is expected to travel in the medium before interacting.

Both neutron and gamma attenuation are modelled using the Beer-Lambert law. The probability density of an interaction occurring at depth d is

$$p(d) = \mu e^{-\mu d} \tag{5.10}$$

where μ is the total attenuation coefficient of the medium, derived from isotopic cross sections via Equations 2.1, 2.2 and 2.3. The corresponding cumulative distribution is

$$P(d) = 1 - e^{-\mu d} \tag{5.11}$$

This yields a sampled penetration depth:

$$d = -\frac{1}{\mu}\ln(1-r) \tag{5.12}$$

Since r and $1-r$ are both uniformly distributed in $[0,1)$, Equation 5.12 can be simplified to:

$$d = -\frac{1}{\mu} \ln r \tag{5.13}$$

The outcome depends on comparing d and L:

- If $d \geq L$, the particle has transmitted through the medium without interacting. The pipeline returns to RayGen, which emits a new particle of the same type at the intersection point with unchanged direction and energy.
- If $d < L$, the particle has interacted before reaching the geometric intersection. The hit position is reset to the sampled depth d, which is then used as the starting point for scattered neutrons or for secondary gamma photons.

Neutron Interaction Check

If the neutron is determined to interact, the next step is to determine whether the interaction is scattering or absorption. This process involves two stages: identifying the interacting isotope and then sampling the interaction type.

Isotope Selection The probability that a neutron interacts with isotope i in the medium is proportional to its contribution to the total attenuation coefficient:

$$p_i = \frac{\mu_{\text{tot},i}}{\sum_j \mu_{\text{tot},j}} \tag{5.14}$$

where $\mu_{\text{tot},i}$ is the total attenuation coefficient of isotope i. Then the interacting isotope is selected via the discrete sampling method (Equations 5.1 and 5.3).

Interaction Type Selection After the interacting isotope is selected, the type of interaction is sampled based on the isotope's cross sections:

$$p_{\text{scatt}} = \frac{\sigma_{\text{scatt}}}{\sigma_{\text{tot}}}, \quad p_{\text{abs}} = \frac{\sigma_{\text{abs}}}{\sigma_{\text{tot}}} \tag{5.15}$$

where σ_{scatt}, σ_{abs}, and σ_{tot} are the scattering, absorption, and total cross section of the chosen isotope.

If the neutron is scattered, the simulation returns to RayGen to emit a new neutron from the interaction position. The scattered neutron inherits the same energy as the incident one. Its emission direction is sampled uniformly over 4π steradians, assuming isotropic scattering. In this way, all scattering events are approximated as elastic incoherent scattering, but a more detailed treatment could be incorporated in future work. If the neutron is absorbed, the pipeline remains in the ClosestHitN shader to determine whether the absorption induces gamma emission.

Neutron Activation Check: Gamma Generation

If the daughter isotope formed after neutron absorption is radioactive, it decays according to its characteristic decay scheme, which may include gamma emission. In the simulation,

once the absorbing isotope is identified, its delayed decay time, which is also the gamma emission time, is sampled using the probability density for a nucleus to decay at time t:

$$p(t) = \lambda e^{-\lambda t} \tag{5.16}$$

where λ is the decay constant determined by the isotope's half-life.

For each candidate gamma photon listed in the ENSDF database [91], its emission probability per decay (defined as absolute intensity) is compared with a random number to decide whether a photon is emitted. If emission occurs, the photon is assigned the corresponding energy, an isotropic emission direction, and the position of the neutron interaction. It is then passed to the RayGen shader for tracing. For computational efficiency, only the two most intense gamma lines per activation event are included. This is sufficient for validating the simulation framework while still reproducing the key peaks in the spectra. The inclusion of full decay schemes could be incorporated in future developments. Once generated, gamma photons undergo the transmission check (as described earlier). If not transmitted, they are absorbed (all gamma interactions, including photoelectric absorption, Compton scattering, and pair production, are lumped into absorption).

5.2.3 GPU Output and Data Processing

Once a neutron or gamma photon is detected, the RayGen shader encodes the event in a four-channel RGBA image, which is the default rendering output of Vulkan Ray Tracing. Repurposing this rendering feature allows the simulation to efficiently record and process large volumes of event data in matrix form. Neutron projections and gamma spectra are then reconstructed from these encoded images.

The output image has the same size as the neutron source plane of pixels. Each pixel corresponds to a neutron index, and the four colour channels store the outcome of its tracing. The encoding scheme is summarised in Table 5.1. The R and G channels are binary flags identifying whether the detected particle was a neutron or a gamma photon. The B and A channels store the corresponding particle information: hit position for neutrons, or photon energy and delayed time for gammas.

Each dispatch produces one such RGBA image, which is then transferred back to the CPU for decoding and accumulation. For neutrons, the hit position decides in which pixel on the corresponding projection at that orientation the intensity should be accumulated. For gammas, the delayed time, combined with the frame time (i.e., neutron pulse emission time), determines whether the photon is included in the acquired spectrum. Once all dispatches are complete, the projections from different orientations and the gamma spectra at each acquisition time are ready to be compared with experimental data for data fusion via the procedure described in Chapter 4 (Equations 4.1-4.5).

Table 5.1: Tracing outcome encoding scheme of the output RGBA image (32 bits).

Channel Group #1	**Meaning**	**Channel Group #2**	**Meaning**
Binary Flags (**R**, **G**)	Particle Type	Data Values (**B**, **A**)	Particle-carried information
(1, 0)	Neutron	(x, y)	The neutron hit coordinates on the detector.
(0, 1)	Gamma	$((E_{\gamma 1}, E_{\gamma 2}), t_d)$	The characteristic gamma energy and delayed decay time of the radioactive isotope. Each gamma energy value occupies 16 bits of the A channel.
(0, 0)	Any particle that has not been detected.	–	No further data stored; particle excluded from decoding.

5.3 Simulation Validation

5.3.1 Neutron Beam

The neutron beam generated by the simulation shows close agreement with the experimental beam, as illustrated in Figure A.5. The spatial flux variation is reproduced in both horizontal and vertical directions through sampling a 2D Gaussian distribution. The main discrepancy occurs at the centre of the vertical profile, where the maximum relative error remains below 5%, due to approximating a non-Gaussian distribution with a Gaussian function in the simulation. In addition to reproducing the spatial flux distribution, the simulation also captures the energy characteristics of the beam. The agreement in both spatial and energy distributions indicates that the incident neutron beam is well represented in the simulation, providing a solid basis for subsequent NT and GS analyses.

5.3.2 Neutron Radiography

Since copper has comparable absorption and scattering cross sections, its absorption and scattering effects are both significant, allowing to validate the simulation's neutron interaction features using it. Accordingly, we performed a neutron radiography experiment with a 1 cm^3 Cu cube placed on an Al bar against the scintillator (Figure 5.6a) and simulated this experiment (Figure 5.6b). The pixel-wise comparison on the projections (Figure 5.6d) shows good overall agreement between the simulated and experimental projections. Minor discrepancies occur at the beam rim (due to low counting statistics), at the cube edges (caused by a slight model mismatch), and at the Al bar (omitted in the simulation). However, most of the comparison image, particularly the Cu cube itself, shows negligible differences between the experiment and simulation. Compared to the Geant4 simulated NT projections (Chapter 4), the simulation precision is greatly improved by increasing emitted neutron

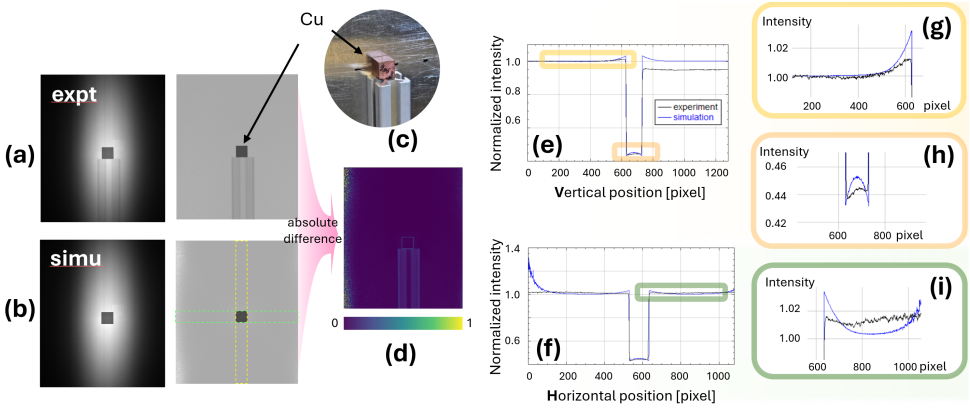

Figure 5.6: (a) Experimental and (b) simulated neutron projections of a Cu cube placed against the scintillator, shown with the original projections on the left and the normalised projections on the right. (c) Photograph of the Cu cube in the experiment. (d) Absolute difference between the normalised experimental and simulated projections. Vertical (yellow dashed) and horizontal (green dashed) strip regions are selected from the normalised images to extract one-dimensional profiles, obtained by averaging grey values across the short axis of each strip. The resulting profiles are shown along the vertical (e) and horizontal (f) directions. (g-i) Zoomed views of the intensity profiles

counts (approximately ten billion neutrons), while the running time is only approximately 5 minutes.

The experimental and simulated data are further compared using intensity profiles extracted from the normalised images. Vertical (yellow dashed) and horizontal (green dashed) strip regions across the cube are selected to assess the scattering and absorption effects. Figure 5.6e and 5.6f show the comparison of vertical and horizontal intensity profiles, respectively. In both cases, the normalised neutron intensities show good agreement between simulation and experiment, with values closely matching inside and outside the cube regions. A sharp decrease is observed within the cube, as neutrons are strongly absorbed by the Cu. Outside the cube, intensities remain close to unity, reflecting the negligible flux variation in uncovered regions.

Notably, slightly elevated intensities appear near the cube edges, caused by scattered neutrons, with higher values closer to the cube and a consistent decreasing trend in both experiment and simulation (Figure 5.6g). Interestingly, neutron scattering also contributes within the cube (Figure 5.6h), where a small bump is observed in both experiment and simulation data. This effect occurs because the cube centre has a relatively higher probability than other regions of the cube of receiving scattered neutrons. The mean transmission of the cube region is reproduced as 44.5% in the simulation, closely matching the experimental value of 44.2%. In the horizontal direction, both experimental and simulation profiles are strongly influenced by the rapid decrease in neutron flux, particularly near the beam rim (Figure 5.6f and 5.6i). Despite these fluctuations, the intensities remain close to unity, and the beam rim regions are typically away from the objects of interest in experiments. Overall, the simulation successfully captures the main transmission and scattering features of Cu, providing reliable reproduction of the experimental projection. Similar good performance

is expected for other materials, since the underlying isotope selection and interaction modelling in the simulation are the same as for copper.

5.3.3 Gamma Spectroscopy

Natural copper consists of two stable isotopes, Cu-63 (69%) and Cu-65 (31%). After neutron capture, they form the radioactive isotopes Cu-64 (12.7 h) and Cu-66 (5.12 min). Cu-64 emits two main gamma lines at 511 keV and 1346 keV with emission probabilities of 35% and 0.47%, while Cu-66 emits lines at 1039 keV and 833 keV with probabilities of 9.23% and 0.22%. Because copper has only two stable isotopes and simple, well-characterised activation channels, it is an ideal reference material for evaluating GS simulations.

Following the neutron radiography experiment with the Cu cube in Section 5.3.2, we measured gamma spectra from the cube and simulated the corresponding GS measurements under identical irradiation conditions. The irradiation lasted for 22 minutes, followed by seven consecutive gamma measurements. Peak intensities were extracted from each spectrum and compared directly with the absolute simulated gamma intensities.

Figure 5.7 shows the comparison between simulation and experiment. For each isotope, simulated gamma intensities are of the same order of magnitude as the experimental values. Both simulated and experimental intensities were fitted with decay curves, and the resulting decay constants agree well. However, across all peaks, the absolute simulated intensities are systematically about 15% lower than the experimental values, a discrepancy larger than the mismatch observed in the Geant4 benchmark (Chapter 4). Since the relative intensities between gamma lines are consistent, this uniform offset most likely arises from a factor that scales all signals equally, independent of isotope or gamma energy.

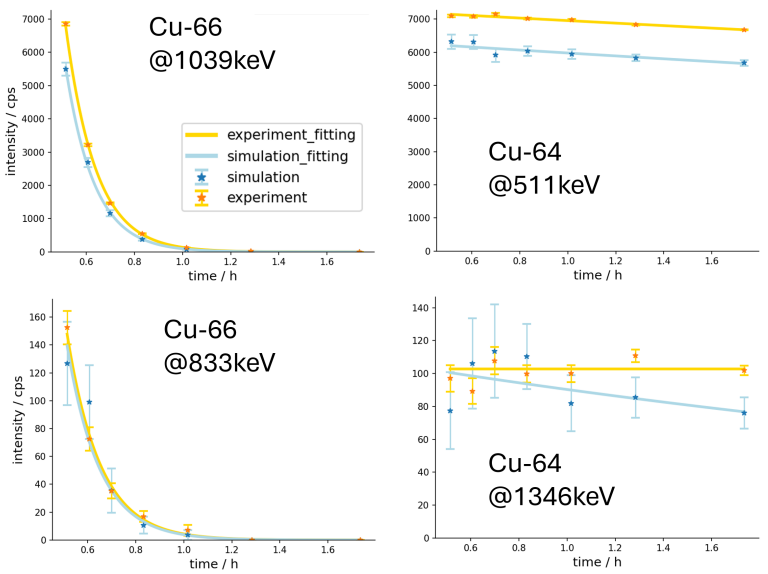

Figure 5.7: Correspondence of the time-dependent simulated and experimental gamma intensity for the different isotopes and peaks of the Cu cube.

We exclude object-related errors, including geometry, mass, and density, based on the previous validated neutron transmission and interaction modelling, and we excluded flux and detector efficiency corrections as possible sources of error. Theoretically, the approximation in gamma generation, where the full de-excitation cascade is replaced by absolute emission probabilities for the main gamma lines, should not affect the absolute scale of intensities but only the fine structure of the spectrum. The remaining likely cause lies in the gamma transport modelling, where all non-transmission interactions (Compton scattering, photoelectric absorption, pair production) are treated as absorption. This approximation underestimates the contribution of scattered photons. However, since most Compton scattering occurs at angles with substantial energy loss [92], these photons rarely contribute to the full-energy peaks. In addition, Compton scattering is strongly energy dependent, whereas the observed scaling factor appears independent of gamma energy. Therefore, Compton effects alone cannot account for the uniform underestimation.

Although the investigation is ongoing, we treated the underestimation as an effective scaling factor in the GS analysis. This does not hinder the data-fusion process, as the simulated isotope composition remains valid as long as all gamma intensities are affected by a similar factor. Therefore, instead of requiring absolute agreement in gamma intensities (the strategy used in Chapter 4), we compare scaling factors across gamma peaks: if they are consistent, the corresponding composition is considered the most accurate.

5.4 Application to the Ommerschans Sword

As shown in Figure 5.1, the experiment on the Ommerschans sword was more complex than the copper reference case, involving multiple short irradiations and long NT measurements for different regions along its height. The radioactivity of each region was measured after irradiation. In this study, the short irradiation experiment on the tip region (Figure 5.8) was selected as a representative case for detailed analysis. The irradiation lasted 31 minutes with the sword kept fixed in orientation and position. Subsequently, three gamma measurements were performed with an object-to-detector distance of 31.5 cm, for a total acquisition time of 15 minutes.

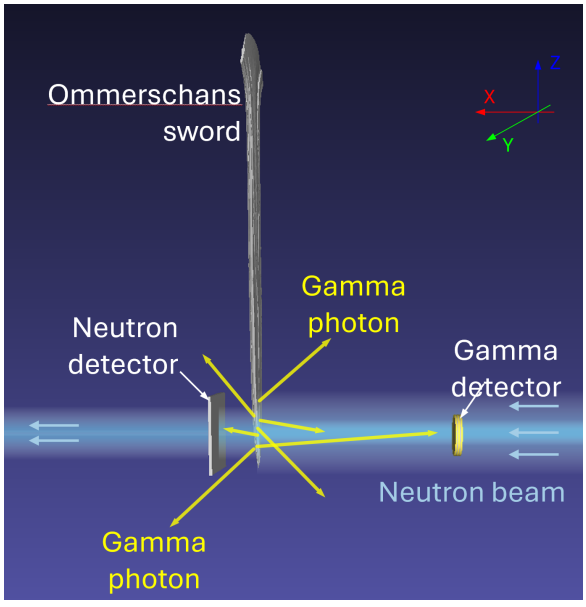

Figure 5.8: Simulation setup for the radiography and subsequent GS measurements on the Ommerschans sword tip region.

To simulate this experiment, the sword's 3D geometry model, derived from NT reconstruction, was assigned a bronze composition. As a first step, the bronze was modelled as a binary Cu-Sn alloy, consistent with XRF measurements indicating copper and tin as the dominant elements. Figure 5.9a compares the residuals between experimental and simulated NT projections with the Cu concentration varying from 80-100 wt%. Increasing the Cu fraction reduces the residuals, with the minimum obtained for a pure Cu assumption (see details in Figure A.6). However, this contradicts the XRF results, which detected 14.5 wt% Sn on the surface. This discrepancy suggests the influence of hydrogen, commonly introduced by bronze corrosion, which significantly affects neutron attenuation.

To evaluate this effect, we simulated a ternary Cu-Sn-H composition with 85 wt% Cu and 15 wt% Sn while varying the hydrogen content (Figure 5.9b). The residuals decrease as the hydrogen fraction increases, reaching a minimum around 0.05 wt% H. Given the sampling step and possible Cu-Sn composition variation, a hydrogen range of 0.025-0.075 wt% was considered realistic. If the hydrogen originates from cupric hydroxide ($Cu(OH)_2$), a typical bronze corrosion product, the amount corresponds to a uniform corrosion layer of approximately 110-330 μm, which falls within the typical archaeological bronze corrosion range of 100-500 μm [71]. On this basis, three representative cases with 0.025, 0.05, and 0.075 wt% H were carried forward for GS analysis.

The GS analysis was then performed under the Cu-Sn-H composition assumptions, with H assumed to be homogeneously distributed in the object. Tin, like copper, has two activation products relevant within the experimental time: Sn-123m (half-life 40.6 min, emitting a 160 keV peak) and Sn-125m (half-life 9.52 min, emitting a 332 keV peak). These peaks, together with the copper peaks described earlier, form the basis of the GS comparison. For each element, a scaling factor was calculated as the ratio of experimental to simulated gamma intensities, averaged across isotopes (Figure 5.10).

Across all hydrogen contents, the Cu scaling factor decreases slightly with increasing Cu concentration, while the Sn scaling factor increases progressively. The intersection point of the Cu and Sn scaling factors consistently lies between 85 and 87.5 wt% Cu, suggesting

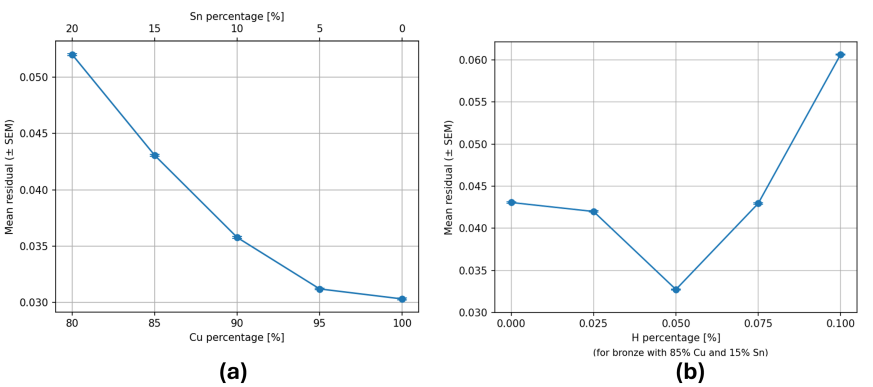

Figure 5.9: Comparison of residuals between simulated and experimental neutron projections under different composition assumptions for the Ommerschans sword. (a) Binary Cu-Sn bronze with Cu concentration varied from 80-100 wt%. (b) Ternary Cu-Sn-H bronze with 85 wt% Cu and 15 wt% Sn while hydrogen content is varied.

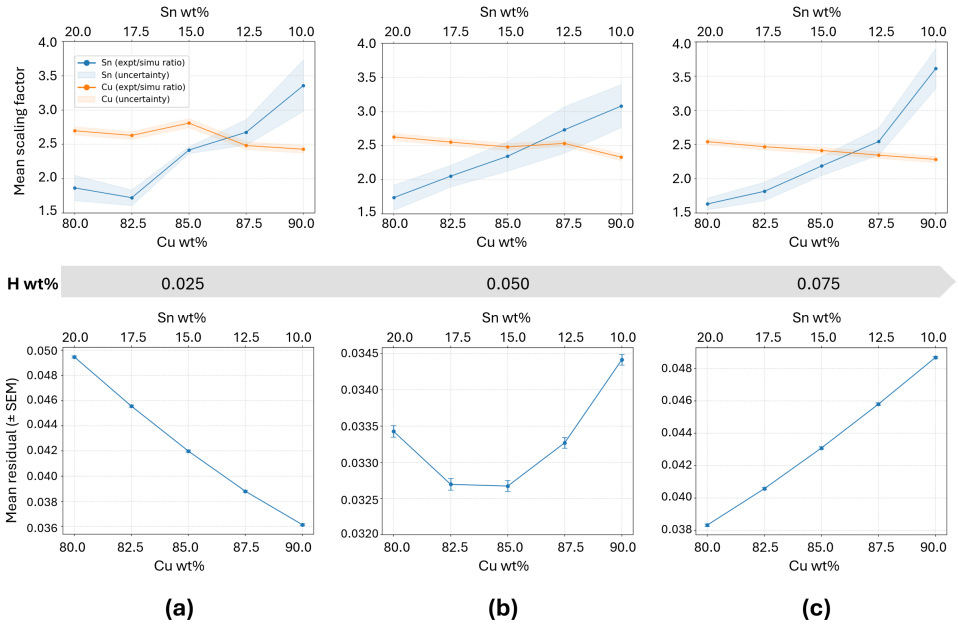

Figure 5.10: Analysis results of NT-GS simulations under Cu-Sn-H composition assumptions with varied Cu and Sn fractions and H fixed at (a) 0.025 wt%, (b) 0.05 wt%, and (c) 0.075 wt%.

this range as the most plausible alloy composition.

For the NT projections, the behaviour differs with hydrogen content. For 0.025 wt% H, the residuals continue decreasing across the investigated range, with the minimum expected above 90 wt% Cu. For 0.075 wt% H, the minimum falls below 80 wt% Cu. Only the 0.05 wt% H case yields a residual minimum within the investigated range, located between 82.5-85 wt% Cu. Although slightly offset from the GS intersection range, this case provides the best overall consistency. Combining the NT and GS comparisons, we infer that the true composition of the sword tip corresponds to 85-87.5 wt% Cu and 12.5-15 wt% Sn, with a small hydrogen contribution between 0.025 and 0.05 wt%, most plausibly close to 0.05 wt%.

5.5 Comparison of the Three Mass Quantification Methods Applied to the Ommerschans Sword

Having applied the three mass quantification methods introduced in this thesis to the Ommerschans sword, we now compare their results in terms of the elemental composition and computational efficiency. The approaches yield broadly consistent outcomes, as summarised in Table 5.2. All three methods converge on an alloy composition of approximately 85-89 wt% Cu and 11-15 wt% Sn, consistent with the XRF measurement, which detected 14.5 wt% Sn on the surface. Only the two simulation-based methods are sensitive to hydrogen, identifying a small contribution, attributable to corrosion products. In addition, both simulation-based methods yield a total sword mass of approximately 3 kg, in good

Table 5.2: Comparison of mass quantification results for the Ommerschans sword (tip region) obtained by the three methods.

Method	Cu	Sn	H	Total Mass
1	388 ± 2 g (86.6 wt%)	60 ± 8 g (13.4 wt%)	–	~448 g (tip)
2	86–89 wt%	11–14 wt%	~ 0.1 wt%	~2978 g (sword)
3	85–87.5 wt%	12.5–15 wt%	~ 0.05 wt%	~2977 g (sword)

Note: Method 1: GS-based method with 1D self-attenuation correction, Method 2: NT-GS data-fusion method using Geant4 (CPU-based), Method 3: NT-GS data-fusion method using GPU-accelerated simulation.

Table 5.3: Comparison of computational efficiency of the three mass quantification methods for analysing the Ommerschans sword.

Method	Simulation per composition		Hardware	Total analysis time
	Neutrons emitted	Runtime		
1	–	–	8-core CPU	< 1 hour
2	1.53×10^{10}	~53 days	8-core CPU	–
2*	1.53×10^{10}	~1 day	Supercomputer	~1 month
3	4.15×10^{10}	~15 min	NVIDIA RTX 3070	~1 day

Note: Method numbers correspond to those in Table 5.2. Method 2* refers to running on a supercomputer with an optimised execution plan.

agreement with the measured weight of the sword [7], providing additional validation.

The three approaches differ sharply in computational demands. The GS-based method mainly involves algebraic calculations with a simple "matchbox" approximation for self-attenuation, making it a rapid and effective option, typically requiring less than an hour. However, its accuracy is limited when applied to complex object shapes and compositions (Chapter 3). The Geant4-based data-fusion method addresses this limitation by iteratively simulating particle physics interactions in detail, but this unavoidably involves a massive workload. Even with a supercomputer and an optimised execution plan, runtime per tested composition is on the order of a day, implying about a month for a full iterative analysis. By contrast, the GPU-accelerated data-fusion method retains the iterative approach but achieves a step change in performance. On a consumer-grade NVIDIA GeForce RTX 3070, a composition test (traces 41.5 billions neutrons) completes in about 15 minutes, reducing the total analysis to roughly a day. This represents a speed-up of two to three orders of magnitude over the CPU baseline, while maintaining the same accuracy.

5.6 Conclusion

A novel GPU-based simulation framework was developed to accelerate neutron tomography and subsequent delayed gamma spectroscopy simulations, forming the computational core of the iterative data-fusion method introduced in Chapter 4. This framework replaces the previously used Geant4-based simulation, overcoming the computational bottleneck associated with CPU-bound ray-tracing. By leveraging Vulkan Ray Tracing and GPU parallelism, the new framework achieves a significant reduction in runtime–from approximately

50 days on an 8-core CPU to just 5 minutes on a consumer-grade NVIDIA GeForce RTX 3070, for a simulation involving ten billion neutrons.

This framework successfully integrates neutron transport, time-resolved neutron activation, and gamma transport processes into a single, unified GPU-accelerated ray-tracing pipeline. Validation against experimental data, including neutron beam characteristics as well as neutron absorption and scattering features and gamma spectral intensities from a Cu reference object, demonstrated both physical accuracy and simulation reliability. Although a uniform offset in absolute gamma intensities was observed across all peaks, the relative intensities remained consistent. This robustness allows the framework to incorporate an effective scaling factor in the GS data analysis, ensuring accurate comparison with experimental results. Combined with pixel-wise comparison of neutron projections, this provides a reliable benchmark for assessing discrepancies between simulated and experimental datasets in data-fusion workflows.

Despite the simplified modelling of certain physical processes, including assuming isotropic neutron scattering, treating gamma interactions as absorptions, and approximating de-excitation cascades using absolute emission intensities, the framework achieves a practical balance between computational efficiency and physical fidelity. This enables rapid exploration of composition models and marks a step change in the feasibility of applying NT-GS data fusion in real-world cultural heritage applications. Application to the Ommerschans sword further demonstrated the framework's accuracy and practical value. The composition inferred from the GPU-based simulation showed strong consistency with results obtained from both the GS-based analytical method and the Geant4-based data-fusion method, while dramatically reducing analysis time from weeks to hours.

By creatively repurposing a real-time graphics rendering pipeline to simulate NT and subsequent GS experiments, the framework delivers GPU-accelerated performance without the need to build a full-scale particle simulation engine from scratch. This is not only a practical solution, but also a pioneering effort to transform high-resolution rendering tools into high-precision neutron transport and nuclear transmutation simulations. Looking ahead, further structural improvements, such as emitting multiple neutrons per frame and performing data accumulation directly on the GPU, could enhance performance even further. Additionally, integrating crystal-structure-aware modelling libraries such as NCrystal [93] would allow for more realistic material representations and enable extensions to simulate other neutron scattering experiments, such as neutron diffraction. We also believe that the framework's ability to rapidly reproduce high-quality neutron projections can open new opportunities for advancing workflows in radiography-based applications. For example, in studies of water uptake in plant roots [94, 95], where fast radiography is more practical than full tomography, simulation-assisted analysis could help compensate for the lack of 3D information.

6

Conclusion and Outlook

This thesis proposes an insightful experimental strategy for performing gamma spectroscopy (GS) following neutron tomography (NT), making full use of the otherwise wasted radioactivity induced during neutron irradiation to non-destructively extract valuable information on the interior elemental composition of bulk cultural heritage artefacts. To realise this strategy in practice, the thesis implements the fusion of NT and delayed GS data, addressing the challenge of accurately and efficiently quantifying interior compositions. The main objectives were to overcome the analytical difficulties of accurately correcting for the self-attenuation effects of both neutrons and gamma rays as well as to break through the computational barriers posed by iterative methods that rely on large-scale simulations. Through the progressive development of three complementary methods, this work establishes a comprehensive and scalable foundation for the quantitative fusion of NT and GS datasets, advancing the practical use of this NT-GS data-fusion method in cultural heritage investigations.

6.1 Summary of Contributions

Method 1 – Mass Quantification with 1D Self-Attenuation Correction (Chapter 3)

The first method provides a fast and most accessible means to estimate elemental masses from GS data acquired after NT experiments, through an analytical calculation with a simplified "matchbox" model. This approach is largely inspired by Menno Blaauw's work of developing holistic analysis method for INAA [23]. This matchbox model efficiently corrects for neutron and gamma self-attenuation by reducing the correction complexity from three dimensions to one, while preserving the key physical effects governing attenuation. Its accuracy and effectiveness have been demonstrated for objects with homogeneous composition and regular geometry. While its applicability may be limited for artefacts with complex shapes or internal inhomogeneities, it can play a valuable role as a rapid first-step estimation tool which is valuable during experiments or as a foundation for guiding more advanced, simulation-based analyses.

Method 2 – Geant4-Based Iterative Data Fusion (Chapter 4)

The second method advances the fusion of NT and GS by implementing an iterative simulation approach based on the Geant4 Monte Carlo framework. It addresses the analytical challenges of quantifying elemental compositions in complex artefacts composed of multiple materials with irregular geometries and compositional inhomogeneities. By iteratively comparing simulated and experimental neutron projections and gamma spectra, the method enables accurate assignment of elemental information extracted from GS to the corresponding source materials reconstructed from NT. Its application to the Kuvera statuette, which is a typical challenging case involving corrosion, phase segregation, and a concealed consecration deposit, highlights the method's strong capability in handling structurally and compositionally complex objects. While the approach delivers high analytical accuracy, its computational demands, particularly due to the reliance on CPU-based simulations, currently limit its efficiency for large-scale or time-sensitive applications. Nonetheless, the method is quantitative in reproducing the experimental results, and therefore can quantitatively determine the amount of each element, expressed in grams, of the object, setting a robust benchmark for simulation-based NT-GS data fusion in heritage science.

Method 3 – GPU-accelerated Data Fusion (Chapter 5)

The third method addresses the practical bottlenecks of simulation-based data fusion by fundamentally rethinking the computational approach. Rather than relying on traditional CPU-based Monte Carlo simulations, it repurposes a real-time GPU graphics rendering pipeline to simulate neutron transport, time-resolved neutron activation, and gamma transport. This enables NT-GS simulations involving ten billion neutrons to be completed within minutes on a consumer-grade GPU, reducing overall data-fusion analysis time from weeks to hours. Its accuracy and efficiency have been validated experimentally. While it introduces certain physical simplifications, the new GPU-based simulation framework strikes a robust balance between computational speed and physical fidelity, transforming the simulation-based NT-GS data fusion from a technically demanding and time-consuming task into a practical, scalable, and accessible tool, making it especially valuable for large-scale experiments with complex and heterogeneous cultural heritage artefacts.

6.2 General Discussion and Comparative Analysis

This thesis presents a systematic investigation into the fusion of NT and GS datasets, with a goal of non-destructive, quantitative analysis for the interior elemental composition of bulk cultural heritage artefacts. Three complementary methods were developed, forming a coherent strategy adaptable to different levels of object complexity and analytical needs.

- The GS-based analytical approach (Method 1) offers a fast and simple solution for objects with regular geometry and homogeneous composition. While limited in handling complex cases, it serves well for rapid preliminary estimates or as a useful first step in more refined, simulation-based workflows.

- The Geant4-based data-fusion method (Method 2) provides high physical simulation accuracy and supports offers high simulation fidelity and handles complex geome-

tries and inhomogeneities without requiring programming expertise. Although its heavy computational demands and reliance on a CPU-based core limit practical use—especially for large-scale simulations—it enables non-invasive quantification of hidden bulk compositions in objects thousands of years old, and (within this thesis) serves as the reference method for NT-GS data fusion.

- The GPU-based data-fusion method (Method 3) offers a flexible, efficient simulation tool that reproduces the accuracy of Method 2 while dramatically improving computational performance, making it the most suitable option for detailed studies of complex archaeological objects in complex NT and GS experiments.

Each method has clear advantages, serving a distinct but complementary role. Together, they form a practical "toolkit" for adapting NT-GS data fusion to diverse artefact types, analytical goals, and experimental constraints in cultural heritage research.

6.3 Outlook and Future Work

This work contributes a comprehensive, scalable, and accessible solution for NT-GS data fusion in cultural heritage science, advancing the state of the art in non-destructive elemental analysis and setting the foundation for broader interdisciplinary applications.

Future directions may include:

- GPU efficiency improvements: incorporating multiple neutrons per frame and enabling GPU-side data accumulation to further reduce runtime.
- Physical modelling upgrades: integrating libraries such as NCrystal [93] into the GPU-based framework to simulate more realistic crystalline structures and scattering behaviours.
- Gamma intensity calibration: investigating the underlying cause of the unified scaling factor to improve the GPU-based framework's accuracy of absolute gamma yield predictions.
- Extended application to the Ommerschans sword: Applying the data-fusion method to additional regions of the Ommerschans sword to explore compositional variation along its height.
- Cross-domain applications: extending the methods to other fields where rapid, non-invasive compositional analysis is valuable.

A

Supplementary Information

Table A.1: Elemental mass composition of the Shiva's pendant calculated from GS-based mass quantification.

Element	**Isotope**	**@ E_γ [keV]**	**Elemental mass [g]**	**Average mass [g]**
Au	Au-198	411	0.01	0.01
		676	0.01	
Ag	Ag-110m	885	0.60	0.59
		658	0.59	
		937	0.59	

Table A.2: XRF results of two different positions of the Kuvera statuette.

Detection position	**Elemental composition [wt%]**													
	Cu	Sn	Au	Ag	Fe	Pb	Sr	Zn	Bi	Ni	Mo	As	Ti	Co
Filler & foil	14	61	15	7	1.23	0.66	0.36	0.09	0.03	0.03	0.01	\	\	\
Bronze corrosion	77	21	\	0.11	0.51	0.67	\	\	\	0.04	0.004	0.33	0.23	0.03

Table A.3: Summary of the residual between the simulated and the experimental data for the CYL experiment.

Material	Main elements	Actual mass [gr]	Residual (GS) [%] Value	Residual (GS) [%] Std	Residual (NT) [%] Value	Residual (NT) [%] Std	Total residual [%] Value	Total residual [%] Std
Cu cube	Cu	8.99	1	1	9	7	10	7
Al-7075	Cu	4			12	8	13	8
	Al	207	2	3			14	9
Ti6Al4V	Al	0.21			8	6	10	7
	Ti	3.15	15	11			23	13
	V	0.14	8	5			16	8
Au bead	Au	0.14	5	1	33	24	38	24
Ag nugget	Ag	0.33	42	13	18	14	60	19
Sn plate	Sn	5.02	8	4	8	5	16	6
Pb plate	Pb	4.30	\	\	9	8	≥ 9	≥ 8

Note: Residual (GS) = residual between simulated and experimental decay radiation. Residual (NT) = residual between simulated and experimental neutron projections.

Table A.4: Summary of quantified elemental masses for the *Kuvera* statuette.

Element	**Cu**	**Sn**	**Ag**	**Au**	**As**	**Co**	**Mn**	**Sb**	**Cl**	**Na**	**Total**
Elemental mass [g]	444	74	5.36	2.30	0.40	0.18	0.003	0.13	0.08	0.20	526[a]

[a] Weighed total is 488 g.

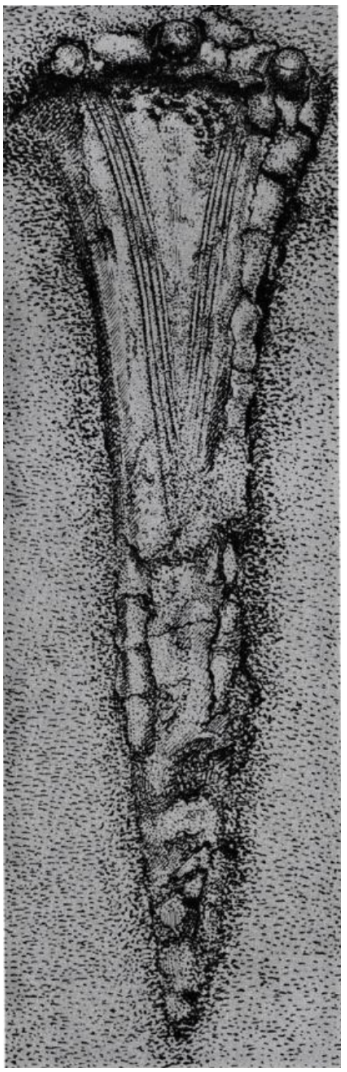

Figure A.1: The grooved ogival dagger from Annertol-Schuilingsoord, Drenthe, the Netherlands is featured by the line decoration. Drawing from Butler, Lanting and Van der Waals [96].

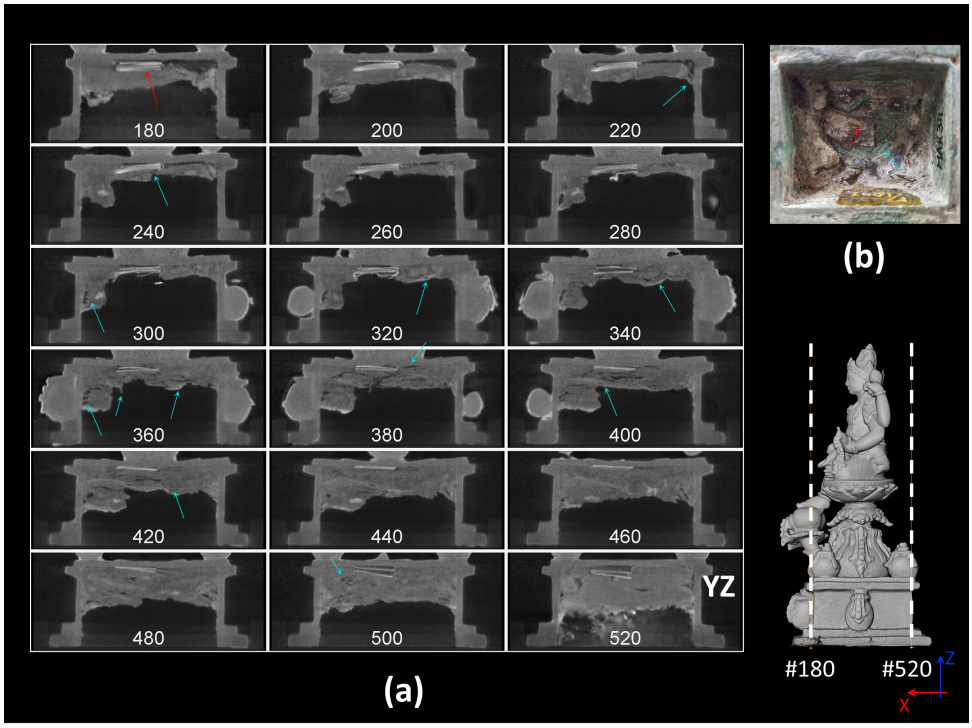

Figure A.2: (a) Reconstructed slices of the pedestal of the Kuvera statuette, with a consecration foil (red arrow) hidden inside and part of it sticking out from the filler. The filler is probably a mixture of pure tin (solder material) and bronze foil(s) (cyan arrow). From slice #520, we can see a layered structure of the tin material, which may caused by multiple tin castings. (b) Bottom view of the pedestal, showing the consecration foil (red arrow) and the bronze foil(s) (cyan arrow).

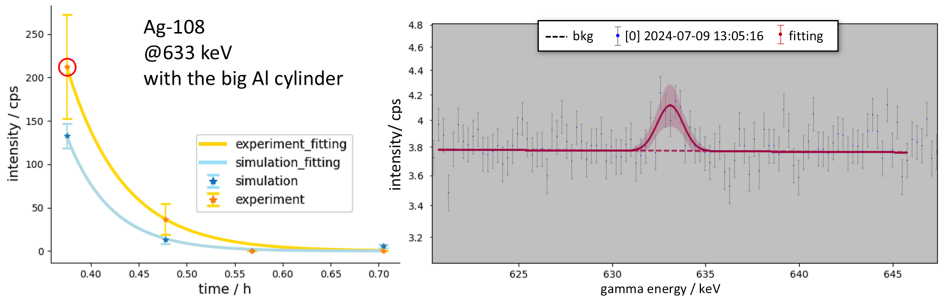

(a)

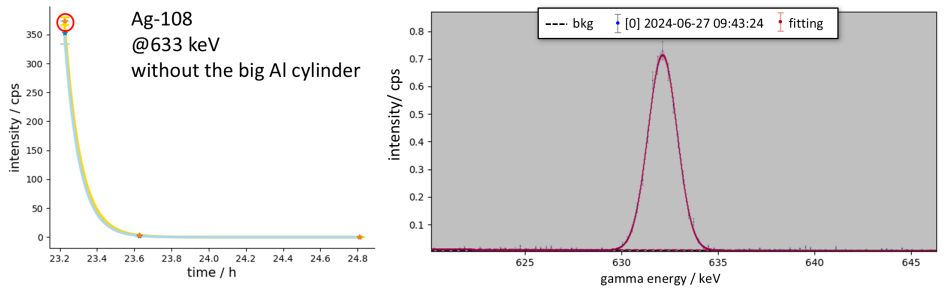

(b)

Figure A.3: Comparison of the accuracy of the GS simulation for small objects with and without a strong background. Here, we use a silver nugget (from the CYL) as an example to illustrate the effect of a strong spectral background in GS analyses. (a) (left) In the CYL experiment, there is a mismatch of 42% between the simulated and experimental gamma intensity from the silver nugget (0.33 g), primarily due to the strong spectral background generated by the (230 g) aluminium cylinder. (right) The gamma spectrum (blue dots) of the first measurement and the fitted peak (red line) at 633 keV showing a significant uncertainty (shaded area). (b) (left) When the silver nugget was irradiated and measured alone in another experiment, the mismatch reduced to 6%, as the fitted peak more accurately represented the gamma data thanks to the improved signal-to-noise ratio. (right) The corresponding gamma spectrum and fitted peak are shown for this scenario.

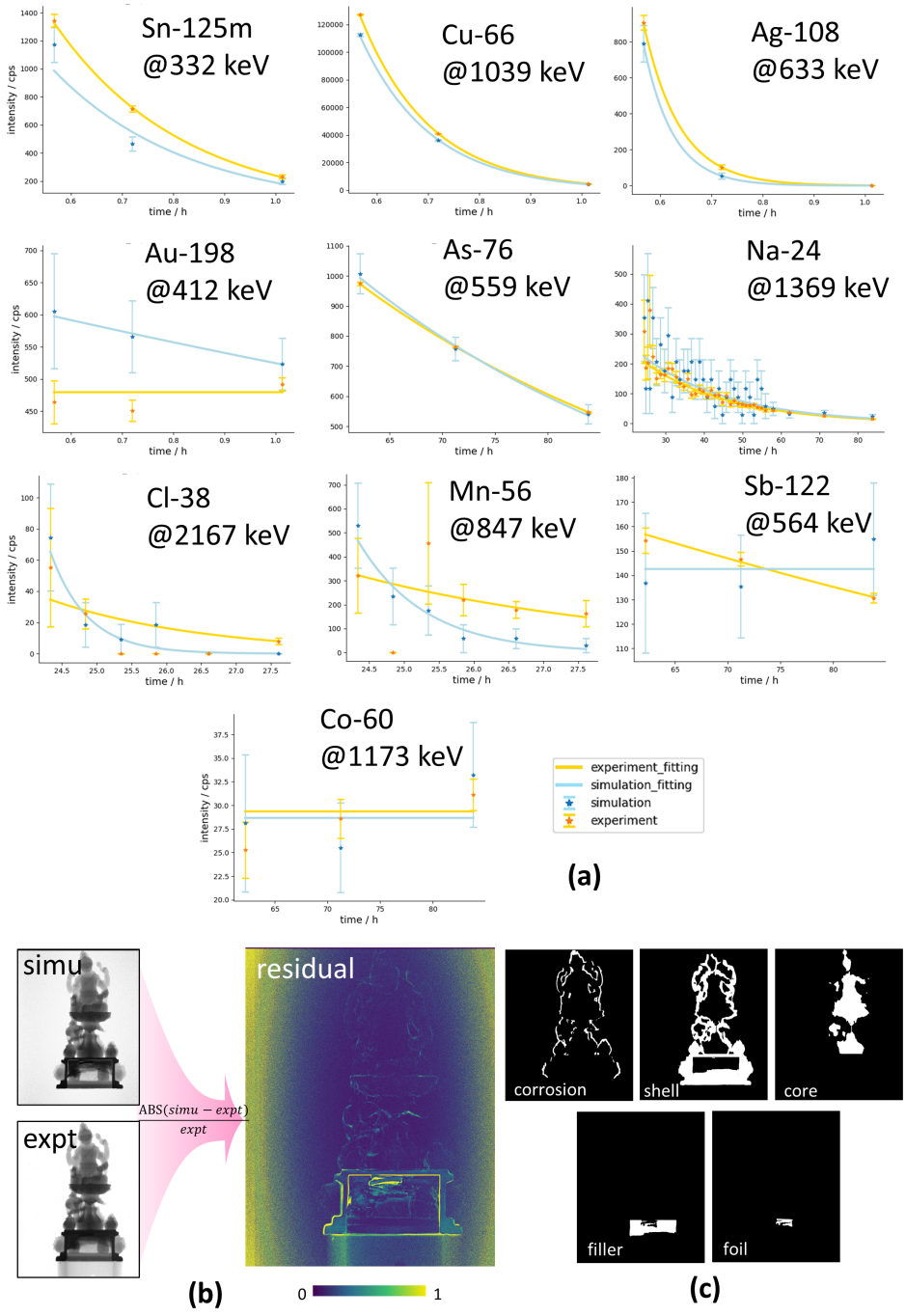

Figure A.4: For the Kuvera statuette, the composition was determined after several iterations of NT and GS simulations. Here we show the results of simulations using this composition. (a) Correspondence between experimental and the simulated gamma intensity for each studied isotope. (b) Agreement between the experimental and the simulated NT projections. (c) Binary masks of each material segment used in Equation 4.2 to evaluate the NT residual, individually.

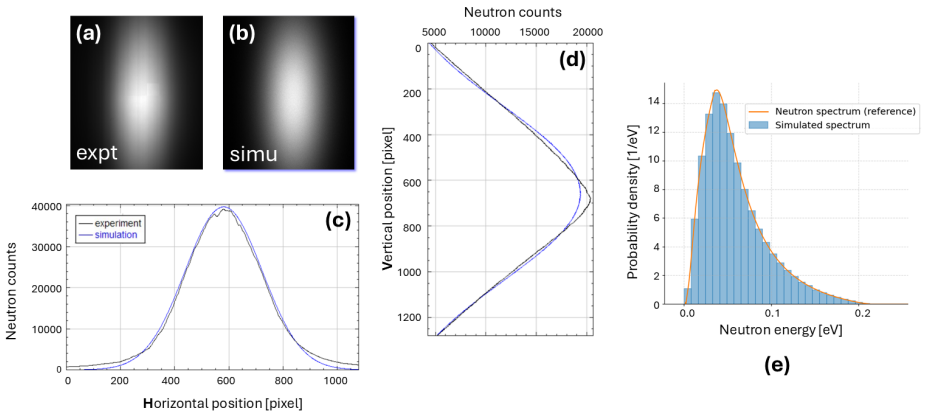

Figure A.5: (a) and (b) Experimental and simulated projections of the open neutron beam. (c) and (d) Comparison of experimental and simulated beam profiles based on pixel grey values (neutron counts) projected along the horizontal and vertical directions. The simulated projection is scaled to match the total neutron counts of the experimental projection. (e) Comparison of experimental and simulated neutron energy spectra.

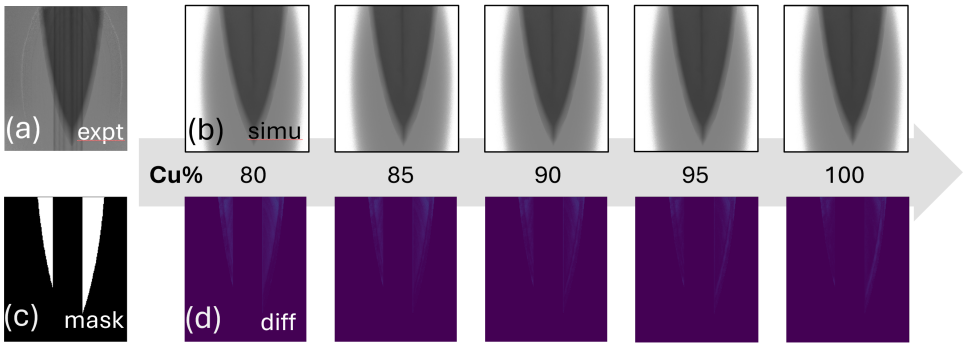

Figure A.6: (a) Normalised experimental neutron projection of the Ommerschans sword's tip region. The strips correspond to the Al bar used as a holder in the experiment. (b) Corresponding simulated projections with assumed Cu concentrations varying from 80 wt% to 100 wt% in Cu–Sn bronze (the Al bar is not included in the simulation).With increasing Cu fraction, the sword appears progressively darker, as Cu interacts more strongly with neutrons than Sn. (c) Mask image used to restrict the comparison region to the sword only. (d) Comparison between simulated and experimental projections, with residual values visualised by blue shading. Smaller residuals (darker blue) indicate closer agreement between simulation and experiment. The residual decreases as the Cu concentrations increases, reaching a minimum when the material is assumed to be pure copper.

Bibliography

References

[1] Daniel O'Flynn, Anna Fedrigo, Laura Perucchetti, and Aurélia Masson-Berghoff. Neutron tomography of sealed copper alloy animal coffins from ancient egypt. *Scientific Reports*, 13(1):4582, 2023.

[2] Marcos Martinón-Torres, Xiuzhen Li, Yin Xia, Agnese Benzonelli, Andrew Bevan, Shengtao Ma, Jianhua Huang, Liang Wang, Desheng Lan, Jiangwei Liu, et al. Surface chromium on terracotta army bronze weapons is neither an ancient anti-rust treatment nor the reason for their good preservation. *Scientific Reports*, 9(1):5289, 2019.

[3] Mirta Sibilia, Chiaramaria Stani, Lara Gigli, Simone Pollastri, Alessandro Migliori, Francesco D'Amico, Chiara Schmid, Sabina Licen, Matteo Crosera, Gianpiero Adami, et al. A multidisciplinary study unveils the nature of a roman ink of the i century ad. *Scientific Reports*, 11(1):7231, 2021.

[4] Francesco Cantini, Sara Creange, Yueer Li, Lambert van Eijck, Nikolay Kardjilov, Saurabh Kabra, and Francesco Grazzi. Morphological and microstructural characterization of an ancient chola bronze statuette by neutron-based non-invasive techniques. *Archaeological and Anthropological Sciences*, 16(3):45, 2024.

[5] Francesco Cantini, Antonella Scherillo, Anna Fedrigo, Monica Galeotti, Andrea Cagnini, Simone Porcinai, Anna Patera, Francesca Morandini, and Francesco Grazzi. The vittoria alata from brescia: a combined neutron techniques and sem-eds approach to the study of the alloy of a bronze roman statue. *Journal of Archaeological Science: Reports*, 51:104112, 2023.

[6] Rijksmuseum van Oudheden. Zwaard van ommerschans.

[7] *Larger than life: The Ommerschans Hoard and the role of giant swords in the European Bronze Age (1500-1100 BC)*. Sidestone Press, 2024.

[8] Zhou Zhou, Jeroen Plomp, Lambert van Eijck, Peter Vontobel, Ralph P Harti, Eberhard Lehmann, and Catherine Pappas. Fish: A thermal neutron imaging station at hor delft. *Journal of Archaeological Science: Reports*, 20:369–373, 2018.

[9] Youngju Kim, M Cyrus Daugherty, Daniel S Hussey, Jacob M LaManna, David L Jacobson, Jongyul Kim, Caitlyn M Wolf, Paul A Kienzle, Daeseung Kim, Minsu Han, et al. Application of neutron grating interferometry and tomography to the nineteenth century korean copper coins. *Scientific Reports*, 15(1):14848, 2025.

[10] Eberhard H Lehmann, David Mannes, and Markus Speidel. Neutron tomography studies of buddhist bronze sculptures. *Applied Physics A*, 130(12):884, 2024.

[11] Francesco Cantini, Oriol Sans Planell, Anders Kaestner, Manuel Morgano, Filomena Salvemini, Marta Porcaro, Antonio Brunetti, Anna Depalmas, Lorenzo Giuntini, and Francesco Grazzi. Non-invasive characterization of the manufacturing process of a nuragic bronze statuette: a neutron imaging study. *Journal of Archaeological Science: Reports*, 60:104801, 2024.

[12] Fengyan Zhao, Manli Sun, Peixun Li, Antonella Scherillo, Francesco Grazzi, Winfried Kockelmann, Fei Guo, Chen Wu, and Yanpeng Wang. Revealing the manufacturing and corrosion characteristics of chinese archaeological metal arrows by non-destructive neutron techniques. *Archaeological and Anthropological Sciences*, 16(4):50, 2024.

[13] II Bashter. Calculation of radiation attenuation coefficients for shielding concretes. *Annals of nuclear Energy*, 24(17):1389–1401, 1997.

[14] Michael D Glascock. Instrumental neutron activation analysis and its application to cultural heritage materials. In *Handbook of cultural heritage analysis*, pages 69–94. Springer, 2022.

[15] Ronald MW Overwater, Peter Bode, Jeroen JM de Goeij, and J Eduard Hoogenboom. Feasibility of elemental analysis of kilogram-size samples by instrumental neutron activation analysis. *Analytical Chemistry*, 68(2):341–348, 1996.

[16] Zsolt Kasztovszky, Christian Stieghorst, H Heather Chen-Mayer, Richard A Livingston, and Richard M Lindstrom. Prompt-gamma activation analysis and its application to cultural heritage. In *Handbook of cultural heritage analysis*, pages 95–143. Springer, 2022.

[17] RL Paul and RM Lindstrom. Prompt gamma-ray activation analysis: fundamentals and applications. *Journal of Radioanalytical and Nuclear Chemistry*, 243:181–189, 2000.

[18] Hans Postma, Luc Amkreutz, David Fontijn, Hans Kamermans, Winfried A Kockelmann, Peter Schillebeeckx, and Dirk Visser. Neutron-based analyses of three bronze age metal objects: a closer look at the buggenum, jutphaas and escharen artefacts. 2017.

[19] Menno Blaauw, H Postma, and P Mutti. An attempt to date an antique benin bronze using neutron resonance capture analysis. *Applied radiation and isotopes*, 62(3):429–433, 2005.

[20] László Szentmiklósi, Boglárka Maróti, and Zoltán Kis. Quantitative, non-destructive elemental composition analysis of 3d-structured samples. *Journal of Analytical Atomic Spectrometry*, 38(2):333–341, 2023.

[21] Zs Révay, P Kudějová, Krzysztof Kleszcz, Stefan Söllradl, and Christoph Genreith. In-beam activation analysis facility at mlz, garching. *Nuclear Instruments and Methods in Physics Research Section A: Accelerators, Spectrometers, Detectors and Associated Equipment*, 799:114–123, 2015.

[22] G Festa, L Arcidiacono, A Pappalardo, T Minniti, C Cazzaniga, A Scherillo, C Andreani, and R Senesi. Isotope identification capabilities using time resolved prompt gamma emission from epithermal neutrons. *Journal of Instrumentation*, 11(03):C03060, 2016.

[23] Menno Blaauw. The holistic analysis of gamma-ray spectra in instrumental neutron activation analysis. *Nuclear Instruments and Methods in Physics Research Section A: Accelerators, Spectrometers, Detectors and Associated Equipment*, 353(1-3):269–271, 1994.

[24] *Advances in Neutron Activation Analysis of Large Objects with Emphasis on Archaeological Examples*. Number 1838 in TECDOC Series. INTERNATIONAL ATOMIC ENERGY AGENCY, Vienna, 2018.

[25] P Bode and RMW Overwater. Trace-element determinations in very large samples: a new challenge for neutron activation analysis. *Journal of radioanalytical and nuclear chemistry*, 167:169–176, 1993.

[26] HW Baas, M Blaauw, P Bode, and JJM De Goeij. Collimated scanning towards 3d-inaa of inhomogeneous large samples. *Fresenius' journal of analytical chemistry*, 363(8):753–759, 1999.

[27] Sea Agostinelli, John Allison, K al Amako, John Apostolakis, Henrique Araujo, Pedro Arce, Makoto Asai, D Axen, Swagato Banerjee, GJNI Barrand, et al. Geant4—a simulation toolkit. *Nuclear instruments and methods in physics research section A: Accelerators, Spectrometers, Detectors and Associated Equipment*, 506(3):250–303, 2003.

[28] Eberhard H Lehmann, Eckhard DESCHLER-ERB, and A Ford. Neutron tomography as a valuable tool for the non-destructive analysis of historical bronze sculptures. *Archaeometry*, 52(2):272–285, 2010.

[29] Ian Rittersdorf. Gamma ray spectroscopy. *Nuclear Engineering & Radiological Sciences*, pages 18–20, 2007.

[30] Manuel Dierick, Bert Masschaele, and Luc Van Hoorebeke. Octopus, a fast and user-friendly tomographic reconstruction package developed in labview®. *Measurement Science and Technology*, 15(7):1366, 2004.

[31] Anders P Kaestner. Muhrec—a new tomography reconstructor. *Nuclear Instruments and Methods in Physics Research Section A: Accelerators, Spectrometers, Detectors and Associated Equipment*, 651(1):156–160, 2011.

[32] Davide Micieli, Triestino Minniti, and Giuseppe Gorini. Neutompy toolbox, a python package for tomographic data processing and reconstruction. *SoftwareX*, 9:260–264, 2019.

[33] Henry Gwyn Jeffreys Moseley. Xciii. the high-frequency spectra of the elements. *The London, Edinburgh, and Dublin Philosophical Magazine and Journal of Science*, 26(156):1024–1034, 1913.

[34] DoITPoMS. Powder diffraction (x-ray diffraction 2).

[35] A.A. van Well, V.O. de Haan, and Th. Rekveldt M. Stacked neutron guides at iri delft. *Neutron News*, 2(3):28–31, 1991.

[36] NIST. Xcom: Photon cross sections database.

[37] Menno Blaauw. The use of sources emitting coincident γ-rays for determination of absolute efficiency curves of highly efficient ge detectors. *Nuclear Instruments and Methods in Physics Research Section A: Accelerators, Spectrometers, Detectors and Associated Equipment*, 332(3):493–500, 1993.

[38] H.W. Baas, P. Bode, and M. Blaauw. Ge detector efficiency calculations for determination of three-dimensional radioactivity distributions. *Radiation Physics and Chemistry*, 61(3):637–638, 2001. 8th International Symposium on Radiation Physics - ISRP8.

[39] P Bode, RMW Overwater, and JJM De Goeij. Large-sample neutron activation analysis: Present status and prospects. *Journal of radioanalytical and nuclear chemistry*, 216:5–11, 1997.

[40] R.M.W. Overwater. *The physics of big sample instrumental neutron activation analysis*. Phd thesis 4 research not tu/e / graduation not tu/e), Delft University of Technology, Netherlands, 1994.

[41] M Blaauw and P Bode. Introduction of the k_1-concept for the interpretation of artificial peaks in k_0-based naa. *Journal of radioanalytical and nuclear chemistry*, 169(1):201–208, 1993.

[42] M Blaauw, HW Baas, and M Donze. Height-resolved large-sample inaa of a 1 m long, 13 cm diameter ditch-bottom sample. *Nuclear Instruments and Methods in Physics Research Section A: Accelerators, Spectrometers, Detectors and Associated Equipment*, 505(1-2):512–516, 2003.

[43] M. Blaauw. The k_0 calibration of the iri system for inaa of samples in the kg range. *Journal of Radioanalytical and Nuclear Chemistry*, 220(2):233–235, 1997.

[44] O. Lakmaker and M. Blaauw. The use of big sample inaa for inhomogeneous materials: Homogenizations no longer needed? *Journal of Radioanalytical and Nuclear Chemistry*, 216(1):69–74, 1997.

[45] Menno Blaauw, Olof Lakmaker, and Paul van Aller. The accuracy of instrumental neutron activation analysis of kilogram-size inhomogeneous samples. *Analytical chemistry*, 69(13):2247–2250, 1997.

[46] RMW Overwater and JE Hoogenboom. Accounting for the thermal neutron flux depression in voluminous samples for instrumental neutron activation analysis. *Nuclear science and engineering*, 117(3):141–157, 1994.

[47] Ronald MW Overwater, Peter Bode, and Jeroen JM de Goeij. Gamma-ray spectroscopy of voluminous sources corrections for source geometry and self-attenuation. *Nuclear Instruments and Methods in Physics Research Section A: Accelerators, Spectrometers, Detectors and Associated Equipment*, 324(1-2):209–218, 1993.

[48] RMW Overwater and P Bode. Computer simulations of the effects of inhomogeneities on the accuracy of large sample inaa. *Applied radiation and isotopes*, 49(8):967–976, 1998.

[49] Portable Antiquities of the Netherlands. Object pan-98491.

[50] William H Walker, Anna M Cederholm, and Leavitt N Bent. The corrosion of iron and steel. *Journal of the American Chemical Society*, 29(9):1251–1264, 1907.

[51] Zhiqiang Song and Ojiyed Tegus. Microstructure and chlorine ion corrosion performance in bronze earring relics. *Materials*, 17(8):1734, 2024.

[52] Bingbing Li, Qixing Xia, and Wenqiang Dong. Comparative study of the corrosive behaviors of rust layers on bronze ware in different corrosive environments. *Materials*, 18(6):1359, 2025.

[53] Daniel Berger, Quanyu Wang, Gerhard Brügmann, Nicole Lockhoff, Benjamin W Roberts, and Ernst Pernicka. The salcombe metal cargoes: New light on the provenance and circulation of tin and copper in later bronze age europe provided by trace elements and isotopes. *Journal of Archaeological Science*, 138:105543, 2022.

[54] Agnese Benzonelli, Ian C Freestone, and Marcos Martinón-Torres. A better shade of black: effects of manufacturing parameters on the development of ancient black bronzes. *Archaeometry*, 59(6):1034–1049, 2017.

[55] Sharada Srinivasan. The art and science of chola bronzes. *ORIENTATIONS-HONG KONG-*, 37(8):46, 2006.

[56] N Kardjilov, A Hilger, I Manke, and J Banhart. Conrad-2: The neutron imaging instrument at hzb. *Neutron News*, 25(2):23–26, 2014.

[57] JR Santisteban, MR Daymond, JA James, and L Edwards. Engin-x: a third-generation neutron strain scanner. *Applied Crystallography*, 39(6):812–825, 2006.

[58] Yueer Li, Sara Creange, Zhou Zhou, William Southworth, Arie Pappot, and Lambert van Eijck. Exploiting activation radiation from neutron tomography reveals the hidden elemental composition of 3d art objects for free. *Scientific Reports*, 14(1):28982, 2024.

[59] Chandra L Reedy. The opening of consecrated tibetan bronzes with interior contents: Scholarly, conservation, and ethical considerations. *Journal of the American Institute for Conservation*, 30(1):13–34, 1991.

[60] Mathilde Mechling, Brice Vincent, Pierre Baptiste, and David Bourgarit. The indonesian bronze-casting tradition. *Bulletin de l'Ecole française d'Extrême-Orient*, 104:63–140, 2018.

[61] Arlo Griffiths. Written traces of the buddhist past: Mantras and dhāraṇīs in indonesian inscriptions. *Bulletin of the School of Oriental and African Studies*, 77(1):137–194, 2014.

[62] Paul Scherrer Institut (PSI). Thermal neutron data—table of linear attenuation coefficients for thermal neutrons (25 mev).

[63] T Vasilopoulou, IE Stamatelatos, EH Montoya, PS Bedregal, I Tsalafoutas, and P Bode. Large sample neutron activation analysis of irregular-shaped pottery artifacts. *Journal of Radioanalytical and Nuclear Chemistry*, 303:853–858, 2015.

[64] I Stamatelatos, F Tzika, T Vasilopoulou, and M Koster-Ammerlaan. Large sample neutron activation analysis of a ceramic vase. *Journal of radioanalytical and nuclear chemistry*, 283(3):735–740, 2010.

[65] Rijksmuseum. Kuvera statuette.

[66] Peter L Bonate. A brief introduction to monte carlo simulation. *Clinical pharmacokinetics*, 40:15–22, 2001.

[67] Joseph Perl, Jungwook Shin, Jan Schümann, Bruce Faddegon, and Harald Paganetti. Topas: an innovative proton monte carlo platform for research and clinical applications. *Medical physics*, 39(11):6818–6837, 2012.

[68] James Anthony Seibert, John M Boone, and Karen K Lindfors. Flat-field correction technique for digital detectors. In *Medical Imaging 1998: Physics of Medical Imaging*, volume 3336, pages 348–354. SPIE, 1998.

[69] Pauli Virtanen, Ralf Gommers, Travis E Oliphant, Matt Haberland, Tyler Reddy, David Cournapeau, Evgeni Burovski, Pearu Peterson, Warren Weckesser, Jonathan Bright, et al. Scipy 1.0: fundamental algorithms for scientific computing in python. *Nature methods*, 17(3):261–272, 2020.

[70] Brendan Whelan, Billy W Loo Jr, Jinghui Wang, and Paul Keall. Topasopt: An open-source library for optimization with topas monte carlo. *Medical Physics*, 50(2):1121–1131, 2023.

[71] David A Scott. *Copper and bronze in art: corrosion, colorants, conservation*. Getty publications, 2002.

[72] Chi Xie, Chunlin Fu, Sishi Li, Lingmin Liao, Guantao Chen, and Chunxu Pan. A special ancient bronze sword and its possible manufacturing technique from materials science analysis. *Materials*, 15(7):2491, 2022.

[73] Tiemen Cocquyt, Zhou Zhou, Jeroen Plomp, and Lambert Van Eijck. Neutron tomography of van leeuwenhoek's microscopes. *Science Advances*, 7(20):eabf2402, 2021.

[74] G Verhaar, L van Eijck, DJM Ngan-Tillard, Rene van Beek, and Luc Megens. The investigation of archaeological glass using x-ray fluorescence spectroscopy and x-ray micro computed tomography. In *Recent Advances in Glass and Ceramics Conservation 2022: 6th Interim Meeting of the ICOM-CC Glass and Ceramics Working Group*, pages 145–153, 2022.

[75] Janneke van der Stok-Nienhuis, Tonny Beentjes, Dominique Ngan-Tillard, Lambert van Eijck, Ineke Joosten, and Maarten R van Bommel. Unravelling the construction of silver filigree spheres from a seventeenth century shipwreck using non-invasive imaging. *Heritage Science*, 10(1):98, 2022.

[76] Giulia Marcucci, Antonella Scherillo, Maria Pia Riccardi, Costanza Cucini, Quentin Lemasson, and Daniela Di Martino. Mapping the elemental distribution in archaeological findings through advanced neutron resonance transmission imaging. *The European Physical Journal Plus*, 139(6):475, 2024.

[77] EH Lehmann, A Kaestner, L Josic, S Hartmann, and D Mannes. Imaging with cold neutrons. *Nuclear Instruments and Methods in Physics Research Section A: Accelerators, Spectrometers, Detectors and Associated Equipment*, 651(1):161–165, 2011.

[78] Steven G Parker, James Bigler, Andreas Dietrich, Heiko Friedrich, Jared Hoberock, David Luebke, David McAllister, Morgan McGuire, Keith Morley, Austin Robison, et al. Optix: a general purpose ray tracing engine. *Acm transactions on graphics (tog)*, 29(4):1–13, 2010.

[79] Matthew Rusch, Neil Bickford, and Nuno Subtil. Introduction to vulkan ray tracing. In *Ray Tracing Gems II: Next Generation Real-Time Rendering with DXR, Vulkan, and OptiX*, pages 213–255. Apress, 2021.

[80] Chris Wyman and Adam Marrs. Introduction to directx raytracing. In *Ray Tracing Gems: High-Quality and Real-Time Rendering with DXR and Other APIs*, pages 21–47. Apress, 2019.

[81] Simon C Blyth. Opticks: Gpu optical photon simulation for particle physics using nvidia® optix™. In *Journal of Physics: Conference Series*, volume 898. IOP Publishing, 2017.

[82] Shijie Yan and Qianqian Fang. Hybrid mesh and voxel based monte carlo algorithm for accurate and efficient photon transport modeling in complex bio-tissues. *Biomedical Optics Express*, 11(11):6262–6270, 2020.

[83] Julien Bert, Hector Perez-Ponce, Ziad El Bitar, Sébastien Jan, Yannick Boursier, Damien Vintache, Alain Bonissent, Christian Morel, David Brasse, and Dimitris Visvikis. Geant4-based monte carlo simulations on gpu for medical applications. *Physics in Medicine & Biology*, 58(16):5593, 2013.

[84] Steven P Hamilton and Thomas M Evans. Continuous-energy monte carlo neutron transport on gpus in the shift code. *Annals of Nuclear Energy*, 128:236–247, 2019.

[85] M Scott McKinley, R Bliele, PS Brantley, Shawn Dawson, Matt O'Brien, Mike Pozulp, and David Richards. Status of llnl monte carlo transport codes on sierra gpus. Technical report, Lawrence Livermore National Lab.(LLNL), Livermore, CA (United States), 2019.

[86] John Tramm, Paul Romano, Patrick Shriwise, Amanda Lund, Johannes Doerfert, Patrick Steinbrecher, Andrew Siegel, and Gavin Ridley. Performance portable monte

carlo particle transport on intel, nvidia, and amd gpus. In *EPJ Web of Conferences*, volume 302, page 04010. EDP Sciences, 2024.

[87] John Papadopoulos. Dota 2 now supports the vulkan api.

[88] Mike Seymour. The midnight sky's virtual production using stagecraft.

[89] Lefrançois Martin-Karl, Gautron Pascal, Bickford Nia, and Akeley David. NVIDIA Vulkan Ray Tracing Tutorials, 2024.

[90] David A Brown, Mark Benjamin Chadwick, R Capote, AC Kahler, A Trkov, MW Herman, AA Sonzogni, Y Danon, AD Carlson, M Dunn, et al. Endf/b-viii. 0: the 8th major release of the nuclear reaction data library with cielo-project cross sections, new standards and thermal scattering data. *Nuclear Data Sheets*, 148:1–142, 2018.

[91] National Nuclear Data Center. Evaluated nuclear structure data file (ensdf). Accessed: 2025-08-12.

[92] V Babiano, J Balibrea, L Caballero, D Calvo, I Ladarescu, J Lerendegui, S Mira Prats, and C Domingo-Pardo. First i-ted demonstrator: a compton imager with dynamic electronic collimation. *Nuclear Instruments and Methods in Physics Research Section A: Accelerators, Spectrometers, Detectors and Associated Equipment*, 953:163228, 2020.

[93] X-X Cai and Thomas Kittelmann. Ncrystal: A library for thermal neutron transport. *Computer Physics Communications*, 246:106851, 2020.

[94] Christian Tötzke, Nikolay Kardjilov, André Hilger, Nicole Rudolph-Mohr, Ingo Manke, and Sascha E Oswald. Three-dimensional in vivo analysis of water uptake and translocation in maize roots by fast neutron tomography. *Scientific reports*, 11(1):10578, 2021.

[95] Indu Dhiman, Hassina Bilheux, Keito DeCarlo, Scott L Painter, Lou Santodonato, and Jeffrey M Warren. Quantifying root water extraction after drought recovery using sub-mm in situ empirical data. *Plant and soil*, 424(1):73–89, 2018.

[96] JJ Butler, JN Lanting, and JD Van Der Waals. Anner tol iii: A four-period bell beaker and bronze age barrow at schuilingsoord, gem. zuidlaren, drente. *Helinium*, 12(3):225–241, 1972.

Acknowledgments

Writing a doctoral thesis is a journey that no one undertakes alone. While only one name appears on the cover, this work is built upon the support of many. To avoid the risk of unintentional omissions, I will keep my specific mentions brief, but my gratitude extends far beyond the names listed here.

My deepest gratitude goes to my parents, Li WenSheng and Zeng jie. Thank you for your love, your upbringing, and your endless encouragement throughout my life. You raised me to be brave, patient, strong, and to face every challenge with positivity (sometimes a little *too* much positivity!). I am incredibly thankful that you never measured me by financial success, but instead unwaveringly supported me and gave me the freedom to pursue my dreams, whatever they were. Even though I am very different from the people you know and the life I chose is totally different from what you have, you keep trying to understand me more and more. I know that the long distance has not always been easy and has often brought you worry, but I firmly believe the world feels not that big as long as we truly care for one another.

I must also extend my heartfelt thanks to my boyfriend Sulian Lebegue and his family. Thank you for your respect and complete understanding. Whenever I have a problem, you always respond immediately, which gives me a deep sense of security and truly makes me feel at home in Europe. Without your love, help, and support, I would not have been able to enjoy my PhD journey as much as I did, nor would I have grown to love French culture (mostly the food, of course) as much as I do.

In my academic life, I am deeply grateful to my promotor, Prof. Catherine Pappas. Although we did not meet very often, your comments on my work were always precise, insightful, and highly encouraging. We rarely discussed technical details, yet you consistently helped me to manage the overall rhythm of the project and to identify the core issues with impressive clarity. I am especially grateful for your support during my job search and for the encouragement you gave me when I struggled to balance life and work as a female scientist. Your words and your own example have given me greater confidence in facing a future in academia, even though that path is never straightforward. Although my next step is still not completely certain, I look forward to seeing you in Berlin!

My sincere thanks also go to my daily supervisor, Dr. Lambert van Eijck. Thank you for giving me the opportunity to come to the Netherlands. This is a step that truly opened my eyes and enabled me to continue in academia. I greatly appreciate your patience throughout my entire PhD. You taught me how to be critical in research while remaining insightful and relaxed in life. I thoroughly enjoyed our discussions: you always offered incisive and thoughtful perspectives that I had never considered before, whether we were talking about particle physics, ancient craftsmanship, or life in general. I will always remember our conversations about the origin of colour changes, as well as the moment you said “I don’t know” to one of my questions—that was the first time I felt that I might be touching the edge of science. You listened carefully, encouraged me to step into the spotlight, and gently

"forced" me to become independent as soon as possible. All of these aspects have played a significant role in shaping who I am today. I really enjoyed my PhD work and I hope my work has made you satisfied ;-) and I also hope to do justice to your mentorship in my (possible!) future academic career.

To my committee members, Joris Dik, Marlies Goorden, Ineke Joosten, Katrien Keune, Markus Strobl, and Ekkes Brück: thank you for your interest in my research and for taking the time to evaluate my thesis. Your constructive and thoughtful feedback helped me to view my work from new perspectives and to better understand what it means to conduct solid, meaningful research. Jan-Leen Kloosterman, thank you for being my chairperson, which will give me great confidence and ease. Antonia Denkova, thank you for being my mentor and for your willingness to support this work.

I owe a debt of gratitude to Sara Creange, Dominique Ngan-Tillard, Francesco Grazzi, Francesco Cantini, Oriol Sans Planell, Menno Blaauw, Folkert Geurink, Mehmet Sarilar, Raymon Bresse, Guus Verhaar, and Anton Lefering for their invaluable support throughout my doctoral studies and for a helping hand whenever it was needed.

To my grandparents (Li Yongping, Ouyang Li (d. 2022), Zeng Ze (d. 2024), and Zhou Xianfen), my extended family, my co-authors, my colleagues, and my friends: thank you for your support and for being so kind and friendly to me; this made my doctoral journey a wonderful experience. Special thanks also go to my students, from whom I have learned just as much as I have taught.

Last but not least, a huge thanks to my paranymphs, Eline van den Heuvel and Qingru Li, for your efforts in making my defence day a true celebration!

I hope our friendship continues long into the future!

Yueer
Delft, November 2025

Curriculum Vitæ

Yueer Li was born on April 3, 1995, in Dazu, Chongqing, China. After graduating from Chongqing Nankai Secondary School in 2013, she began her undergraduate studies in Biomedical Engineering at the Beijing Institute of Technology.

In 2015, she enrolled in a parallel degree program in Law, specializing in Intellectual Property, initially intending to pursue a career as an IP lawyer. However, her focus shifted back to engineering after completing her bachelor's studies in 2017. She continued with a Master's program in Biomedical Engineering at the same university, where she researched medical imaging under the supervision of Prof. Junhai Wen, guiding her toward an academic path focused on 3D reconstruction.



Driven by the desire to step out of her comfort zone and gain a global perspective, she chose to undertake her PhD research overseas. This motivation brought her to the Netherlands in September 2020, where she became a member of the NPM2 group at TU Delft. Specializing in the fusion of neutron tomography and gamma spectroscopy data within the NICAS-beeldvorming project, she completed the research presented in this thesis under the supervision of Prof. Catherine Pappas and Dr. Lambert van Eijck.

List of Publications

5. Inovative GPU-based simulation framework for accelerating non-invasive quantification of interior composition of bulk artefacts. (in preparation)

4. Book Chapter: Joosten, I., Megens, L., Beentjes, T., Amkreutz, L., **Li, Y.**, & van Eijck, L. (2024). The making of the dirk: What can chemical analysis and imaging techniques tell us. In Larger than Life: The Ommerschans hoard and the role of giant swords in the European Bronze Age (1500-1100 BC) (pp. 107-118). Sidestone Press.

3. Paper: **Li, Y.**, Creange, S., Zhou, Z., Southworth, W., Pappot, A., & van Eijck, L. (2024). Exploiting activation radiation from neutron tomography reveals the hidden elemental composition of 3D art objects for free. *Scientific reports*, 14(1), 28982.

2. Paper: Sans-Planell, O., Cantini, F., Costa, M., Durisi, E., Grazzi, F., Mafucci, E., ... **Li, Y.**, & van Eijck, L. (2023). Improved methodologies to study the performance of the ANET Compact Neutron Collimator. *Nuclear Instruments and Methods in Physics Research A*, 1052, 168260.

1. Paper: Cantini, F., Creange, S., **Li, Y.**, van Eijck, L., Kardjilov, N., Kabra, S., & Grazzi, F. (2024). Morphological and microstructural characterization of an ancient Chola bronze statuette by neutron-based non-invasive techniques. *Archaeological and Anthropological Sciences*, 16(3), 45.

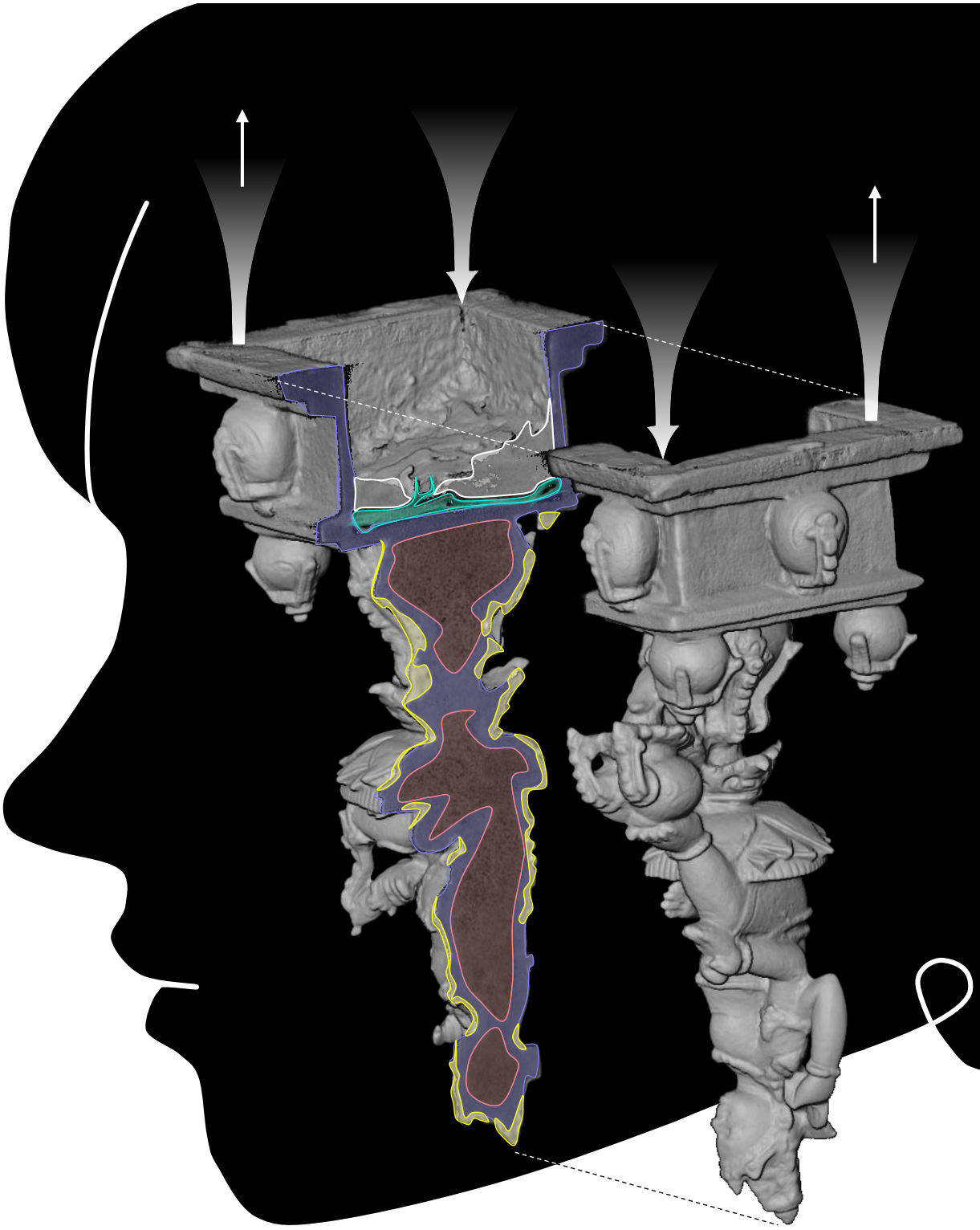

TU Delft